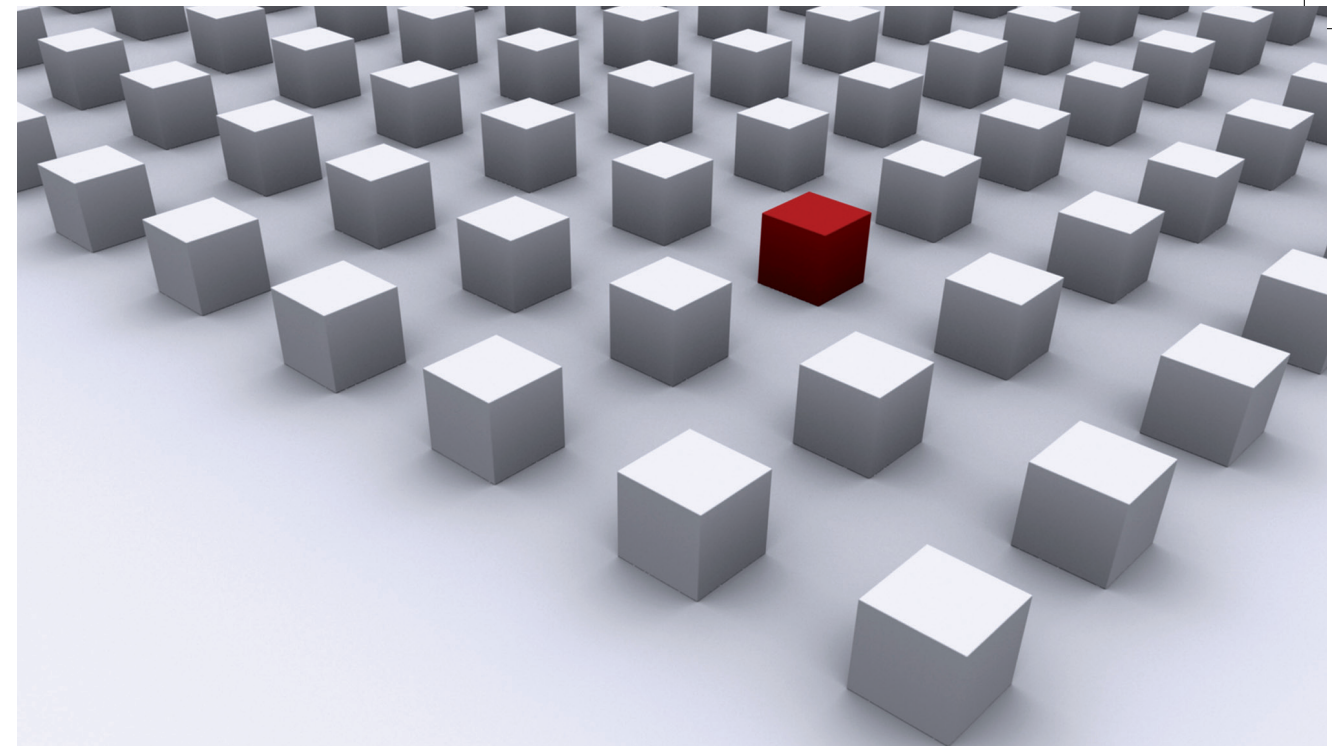


Ultra clean and freely suspended carbon nanotubes provide an ideal model system for electronical transport measurements, and for the investigation of the interplay with their mechanical vibration in the quantum limit. Within the scope of this thesis both excelling electronical and mechanical properties of carbon nanotubes clamped between metal contacts have been investigated. At cryogenic temperatures a quantum dot is formed on the suspended part of the nanotube, where ground and excited state spectroscopy could be performed. Here one has access even to the very first electron on the quantum dot, where the magnetic field dependence of the excited states directly provides the single particle energy spectrum. Curvature induced spin-orbit coupling and KK' valley mixing lift the carbon nanotube specific fourfold degeneracy and induce a level splitting giving rise to unconventional Kondo resonances in the intermediate coupling regime. Tracing those resonances in dependence on an external magnetic field reveals a hitherto unobserved many-body selection rule based on the discrete symmetries of the electronic carbon nanotube system. In addition, the transversal vibration mode of this doubly clamped nano-resonator is actuated and detected, and is used to probe the dependence of the mechanical vibration on the quantum dot charging state and on an external magnetic field. Due to the high mechanical quality the electromechanical coupling in different transport regimes could be analyzed in high precision.

Disertationsreihe Physik - Band 41



Daniel R. Schmid

Suspended Carbon Nanotubes as Electronical and Nano-Electro- Mechanical Hybrid Systems in the Quantum Limit

Universitätsverlag Regensburg

Universitätsverlag Regensburg



ISBN 978-3-86845-111-5

gefördert von:



Alumni der
physikalischen
Fakultät
der Universität
Regensburg e.V.



Universität Regensburg

Daniel R. Schmid

41

Disertationsreihe
Physik



Daniel R. Schmid



Suspended Carbon Nanotubes
as Electronical and Nano-Electro-
Mechanical Hybrid Systems in the
Quantum Limit

Suspended Carbon Nanotubes as Electronical and Nano-Electro-Mechanical Hybrid Systems in the Quantum Limit

Dissertation zur Erlangung des Doktorgrades der Naturwissenschaften (Dr. rer. nat.)

der naturwissenschaftlichen Fakultät II - Physik der Universität Regensburg

vorgelegt von

Daniel R. Schmid

aus Möning

im Jahr 2014

Die Arbeit wurde von Dr. Andreas K. Hüttel angeleitet.

Das Promotionsgesuch wurde am 27.11.2014 eingereicht.

Das Kolloquium fand am 02.06.2014 statt.

Prüfungsausschuss:	Vorsitzender:	Prof. Dr. Tilo Wettig
	1. Gutachter:	Dr. Andreas K. Hüttel
	2. Gutachter:	Prof. Dr. Jascha Repp
	weiterer Prüfer:	Prof. Dr. Rupert Huber



Dissertationsreihe der Fakultät für Physik der Universität Regensburg, Band 41

Herausgegeben vom Präsidium des Alumnivereins der Physikalischen Fakultät:

Klaus Richter, Andreas Schäfer, Werner Wegscheider, Dieter Weiss

Daniel R. Schmid

**Suspended Carbon Nanotubes
as Electronical and Nano-Electro-
Mechanical Hybrid Systems in the
Quantum Limit**

Universitätsverlag Regensburg

Bibliografische Informationen der Deutschen Bibliothek.
Die Deutsche Bibliothek verzeichnet diese Publikation
in der Deutschen Nationalbibliografie. Detaillierte bibliografische Daten
sind im Internet über <http://dnb.ddb.de> abrufbar.

1. Auflage 2014
© 2014 Universitätsverlag, Regensburg
Leibnizstraße 13, 93055 Regensburg
Konzeption: Thomas Geiger
Umschlagentwurf: Franz Stadler, Designcooperative Nittenau eG
Layout: Daniel R. Schmid
Druck: Docupoint, Magdeburg
ISBN: 978-3-86845-111-5

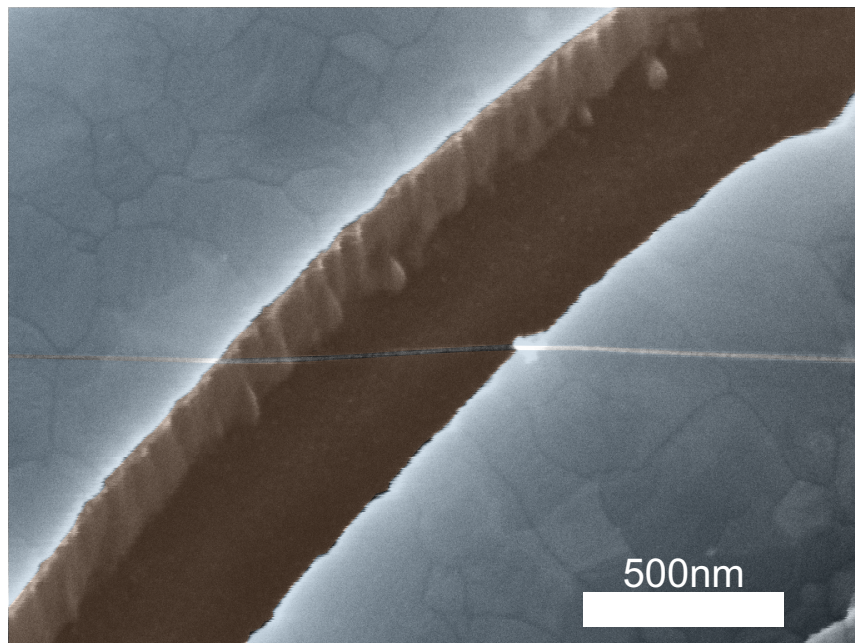
Alle Rechte vorbehalten. Ohne ausdrückliche Genehmigung des Verlags ist es
nicht gestattet, dieses Buch oder Teile daraus auf fototechnischem oder
elektronischem Weg zu vervielfältigen.

Weitere Informationen zum Verlagsprogramm erhalten Sie unter:
www.univerlag-regensburg.de

FÜR MEINE MARINA

FÜR MEINE FAMILIE

There's Plenty of Room at the Bottom.
Richard Feynman



Contents

List of Tables	xi
List of Figures	xvi
List of Symbols	xvii
1 Introduction	1
2 Fabrication of ultra-clean suspended single-wall carbon nanotubes	5
3 Properties of carbon nanotubes	11
3.1 From graphene to carbon nanotubes	12
3.2 Electronical properties of carbon nanotube quantum dots	17
3.2.1 From classical to quantum Coulomb blockade	17
3.2.2 Influence of spin-orbit coupling, KK' -mixing, and magnetic fields on the quantum dot levels	21
3.3 Quantum dot spectroscopy	24
4 The Kondo effect in quantum dots	33
5 Electronic spectroscopy of ultra-clean carbon nanotube quantum dots	37
5.1 Single particle spectrum in the presence of spin-orbit coupling and KK' -mixing	38
5.1.1 Angle calibration	38
5.1.2 Parallel magnetic field	39
5.1.3 Linear low field range	42
5.1.4 High field range	45
5.2 Kondo spectroscopy of CNT quantum dot with finite spin-orbit coupling and KK' -mixing	47
5.2.1 Theory of Kondo transitions and selection rules	48

5.2.2	Characterization of the Kondo effect at zero field	53
5.2.3	Evolution of the Kondo resonances in a perpendicular magnetic field	54
5.2.4	Evolution of the Kondo resonances in a parallel magnetic field	57
5.2.5	Modeling with non-equilibrium many-particle theory	61
5.3	Additionally recorded data	64
5.3.1	Two electron spectrum	64
5.3.2	Magnetic field effect on the conductance in the Kondo regime	67
5.3.3	Hole conduction	69
6	Nanoelectromechanics with CNTs	71
6.1	Theoretical background of CNT nano-electro-mechanical systems . . .	72
6.1.1	Actuation of mechanical vibration in suspended CNTs	72
6.1.2	Continuum mechanics of the transversal bending mode in carbon nanotubes	75
6.1.3	Detection mechanism via dc-current measurement through an embedded quantum dot	76
6.1.4	Dependence of resonance frequency on quantum dot charging .	79
6.2	Magnetic damping of a driven CNT resonator	85
6.3	Charge detection in the Kondo regime	92
6.4	Estimation of the amplitude of the CNT oscillation	97
7	Superconducting microwave resonators	101
7.1	Motivation	101
7.2	Microwave engineering	102
7.3	Micro-fabrication of superconducting coplanar-waveguide resonators .	105
7.4	Measurement setup	107
7.5	Measurements and results	109
7.5.1	Superconducting films	109
7.5.2	RF measurements on sc-cpw resonators	109
8	Conclusion and Outlook	113
A	CNT fabrication	117
A.1	Optical lithography	117
A.2	Electron beam lithography	117
A.3	Metallization and reactive ion etching	118
A.4	Catalyst for the carbon nanotube growth	118
A.5	Chemical vapor deposition growth process	119

B Assignment of the cool-downs to the different measurement setups	121
C Fabrication of sc-cpw resonators	123
C.1 Co-sputtering ReMo-alloys	123
C.2 Reactive ion etching	124
D HF-equipment	125
Bibliography	127
Curriculum Vitae	137

List of Tables

3.1	Transport regimes for a conducting island coupled to leads	18
5.1	Best fit CNT QD parameters for $N_{\text{el}} = 1$	44
5.2	Best fit CNT QD parameters for $N_{\text{el}} = 21$	57
5.3	Best fit CNT QD parameters for $N_{\text{el}} = 17$	59
7.1	Sample parameters of the cpw resonators	106
A.1	Recipe of the SiO_x reactive ion etching process	118
A.2	CNT growth catalyst composition	118
B.1	Specification of the cool-downs	121
C.1	Sputtering parameters for the $\text{Re}_{70}\text{Mo}_{30}$ alloy	123
C.2	Recipe of the reactive ion etching of ReMo	124

List of Figures

2.1	Suspended CNT sample fabrication overview	6
2.2	Optical mask design and optical microscope picture of coarse electrode structures	7
2.3	Electron beam lithography design for the carbon nanotube electrode geometry	8
2.4	Scanning electron microscope picture of the electrode structure	9
2.5	Scanning electron microscope picture of a suspended carbon nanotube	9
3.1	Graphene lattice in real and reciprocal space	12
3.2	Energy dispersion of the π band in graphene with a detail view of one Dirac cone	13
3.3	Unit cell of a (6,4) carbon nanotube	14
3.4	Exemplary calculated dispersion of a (3,3) CNT	16
3.5	Sketches of conductance traces $G(V_g)$ for different CNT types	17
3.6	Replacement circuit of a gate controlled quantum dot coupled to a source and a drain lead	19
3.7	Longitudinal quantization levels on a CNT subband	20
3.8	Single particle level spectrum of a CNT longitudinal mode in perpendicular and parallel magnetic fields	23
3.9	Measurement setup for electronic spectroscopy	24
3.10	Energy diagrams for the case of single electron tunneling and Coulomb blockade	27
3.11	Gate dependence of the current $I(V_g)$ through a carbon nanotube quantum dot at $T=300$ mK	28
3.12	Detail of Fig. 3.11 at few electrons, showing fourfold periodicity . . .	29
3.13	Stability diagram for $0 \leq N_{el} \leq 6$ at $T=30$ mK and of the first holes at $T=300$ mK	30
4.1	Transport processes for spin-1/2-Kondo effect in quantum dots	34
4.2	Temperature dependence of $dI/dV_{sd}(V_g)$ in the Kondo regime	34

4.3	Stability diagram $dI/dV_{sd}(V_g, V_{sd})$ in the intermediate coupling regime ($18 \leq N_{el} \leq 22$) showing sharp zero-bias Kondo ridges	35
4.4	Higher order tunnel processes for spin and orbital Kondo effect in quantum dots	36
5.1	Calibration measurement $I(\theta, V_g)$ of the magnetic field orientation relative to the nanotube axis	39
5.2	Stability diagrams of the first Coulomb oscillation ($0 < N_{el} < 1$) at different magnetic fields parallel to the nanotube axis	40
5.3	Magnetic field dependence of the bias trace $G(V_{sd})$ through the first diamond for $B_{\parallel} < 2$ T	41
5.4	Fitting the first electron excited states with single-electron theory . .	44
5.5	Magnetic field dependence of the bias trace $G(V_{sd})$ through the first diamond in high field $B_{\parallel} < 17$ T	45
5.6	Fit of the high field single electron spectroscopy measurement	46
5.7	Gate dependence of the differential conductance at low bias voltage $V_{sd} = 0.2$ mV and low temperature $T = 30$ mK	47
5.8	Bias traces $G(V_{sd})$ for different fixed N_{el}	49
5.9	Magnetic field dependence and symmetry conjugations of the CNT eigenstates for finite spin-orbit coupling and valley mixing	50
5.10	Elastic and inelastic Kondo transitions	52
5.11	Stability diagram for $N_{el} = 21$ with rescaled bias traces and extracted Kondo temperatures	53
5.12	Magnetic field dependence of the bias trace $G(V_{sd})$ at $N_{el} = 21$ in perpendicular orientation to the CNT axis	54
5.13	Determination of the g'_s -factor by linear fitting of the central peak splitting	55
5.14	Fitting of the peak positions with the single-particle energy spectrum in a perpendicular field	56
5.15	Differential conductance in dependence on a parallel field and on the bias voltage for $N_{el} = 17$	57
5.16	Fitting of the peak positions with the single-particle energy spectrum in a parallel field	60
5.17	Temperature dependence of measured and calculated conductance traces	61
5.18	Magnetic field dependence of measured and calculated conductance traces for both perpendicular and parallel field orientation	63
5.19	Stability diagram of the second Coulomb oscillation and conductance traces $G(V_{sd})$ in parallel field dependence	66

5.20	Gate dependence of the current as function of a parallel magnetic field for $32 < N_{\text{el}} < 48$	68
5.21	Parallel magnetic field dependence of conductance traces $G(V_g)$ for $N_h < 10$	70
6.1	Length dependence of the energy for different CNT vibration modes .	72
6.2	Stability diagram for $1 < N_{\text{el}} < 2$ with hints of longitudinal vibration modes	73
6.3	^3He evaporation cryostat with an installed rf-antenna	75
6.4	Detection mechanism for CNT transversal vibrations	77
6.5	Power dependence of the frequency dependence of the averaged dc-current around a mechanical resonance	78
6.6	Gate voltage dependence of the mechanical resonance frequency on large scale	80
6.7	Gate dependence of the resonance frequency around $N_{\text{el}} = 19$	82
6.8	Sketch of the bias dependence of $f_0(V_g)$ for low and high tunnel rates Γ	83
6.9	Resonance frequency behavior in the few electron regime $0 \leq N_{\text{el}} \leq 3$	83
6.10	Resonance frequency behavior for few hole charging states	84
6.11	Stability diagram for high electron numbers around $N_{\text{el}} = 40$ showing discontinuities in the conductance	85
6.12	Stability diagram around $N_{\text{el}} = 40$ with damped mechanical effects . .	86
6.13	Theoretically calculated current modification in the strong feedback regime	86
6.14	Numerically obtained conductance in the self-excitation area at different magnetic fields	87
6.15	Circuit model explaining magnetic damping	88
6.16	Dependence of the quality factor Q on an external magnetic field . .	90
6.17	Theoretically proved magnetic field dependence of the Q -factor	91
6.18	Gate dependence of the differential conductance in the electron conduction regime	92
6.19	Mean current as function of gate voltage and driving frequency in the strong Kondo regime	93
6.20	Measured and calculated gate dependence of the resonance frequency $f_0(V_g)$ and the current $I(V_g)$	96
6.21	Stability diagram around $N_{\text{el}} = 40$ at $B = 0\text{ T}$ and $B = 2\text{ T}$	97
6.22	Current $ I (V_g)$ in the self-oscillation region for un-damped and damped mechanical vibration	98

7.1	Current density and electric field distribution in cpw-structures . . .	103
7.2	Sketch of half- and quarter-wavelength coplanar waveguide resonators	104
7.3	Cpw resonator fabrication overview	105
7.4	Sketch and SEM images of a quarter-wavelength resonator	107
7.5	Sketch and picture of the HF sample holder	108
7.6	Sketch of the HF measurement setup	108
7.7	Temperature dependence of the Re and ReMo alloy resistance before and after the CVD process	109
7.8	Frequency dependence of the attenuation of quarter-wavelength res- onators	110
7.9	Attenuation of a quarter-wavelength resonator as a function of rf- frequency and input power	112
D.1	Rohde+Schwarz Signal Generator and Analyzer	125
D.2	High frequency dipstick assembly	126

List of Symbols

a	Lattice constant of graphene ($a = 2.46 \cdot 10^{-10}$ m)	12
$\vec{a}_{1,2}$	Unit vectors of the hexagonal graphene lattice	12
α	Gate coupling factor	25
\vec{B}	External magnetic field ($B = \vec{B} $)	21
$B_{\perp,\parallel}$	Perpendicular and parallel component of the external magnetic field	21
$\vec{b}_{1,2}$	Reciprocal unit vectors of the hexagonal graphene lattice	12
c	Speed of light in vacuum ($c = 1/\sqrt{\epsilon_0\mu_0} \simeq 2.998 \cdot 10^8$ m/s)	103
\vec{C}	Chiral vector in carbon nanotubes (CNTs)	12
\hat{C}	Chiral symmetry operator	48
C	Capacitance of a stripline per unit length	103
$C_{g,S,D,\Sigma}$	Gate, source, drain, and total capacitance of a quantum dot	18
Δ	Energy distance between Kramers doublets in one longitudinal mode of a CNT quantum dot (QD)	22
Δ_{\parallel}	Energy distance between different longitudinal modes in a CNT QD	42
$\Delta\epsilon$	Single particle quantum energy	19
ΔE	Addition energy: energy required to charge a quantum dot with an additional electron	19
Δk_{\perp}	Subband spacing of a CNT in the Brillouin zone of graphene	15
Δk_{\parallel}	Longitudinal quantization induced spacing within one CNT subband	43
$\Delta_{KK'}$	KK' splitting	23
Δ_{SO}	Spin-orbit splitting	23
e	Elementary electric charge ($e \simeq 1.602 \cdot 10^{-16}$ A s)	18
E_C	Classical charging energy of a quantum dot	18
E_g	Size of the semiconducting energy gap	16

ϵ	Relative dielectric constant	103
ϵ_0	Vacuum permittivity ($\epsilon_0 \simeq 8.854 \cdot 10^{-12} \text{ A s}/(\text{V m})$)	103
ϵ_{eff}	Effective dielectric constant	103
ε_d	Reference energy of the longitudinal mode of a CNT QD	21
$\varepsilon_{1,2,3,4}$	Eigenenergies of the levels in one CNT QD quadruplet	48
f	Frequency of the rf-signal	80
ϕ	Angle between CNT axis and external magnetic field	21
ϕ_0	Magnetic flux quantum ($\phi_0 \simeq 2.068 \cdot 10^3 \text{ T/nm}^2$)	43
G	Differential conductance, i.e. derivative of the current with respect to the bias voltage ($G \equiv dI/dV_{\text{sd}}$)	25
G_0	Differential conductance at zero bias voltage $V_{\text{sd}} = 0$	35
$\Gamma_{\text{S}}, \Gamma_{\text{D}}$	Tunnel rate to source (S) and drain (D) lead	18
g_{orb}	Orbital g -factor	22
g_{s}	Spin g -factor	22
g'_{s}	Effective spin g -factor	55
\hbar	Reduced Planck constant ($\hbar \equiv h/(2\pi) \simeq 6.582 \cdot 10^{-16} \text{ eV s}$)	38
I	Electric current through the quantum dot	25
k_{B}	Boltzmann constant ($k_{\text{B}} \simeq 8.617 \cdot 10^{-5} \text{ eV/K}$)	17
k_{\parallel}	Longitudinal quantization direction in the k-space of a CNT	15
k_{\perp}	Transversal quantization direction in the k-space of a CNT	15
K, K'	Dirac points in the reciprocal graphene lattice	13
λ	Wavelength of an rf-signal	104
λ_{F}	Fermi wavelength	19
L	Inductance of a stripline per unit length	103
L_{k}	Kinetic inductance of a superconducting stripline per unit length	102
L_{m}	Geometric inductance of a stripline per unit length	102
μ	Electro-chemical potential of the quantum dot	25
μ_0	Vacuum permeability ($\mu_0 = 4\pi \cdot 10^{-7} \text{ V s}/(\text{A m})$)	103
μ_{B}	Bohr magneton ($\mu_{\text{B}} \simeq 5.788 \cdot 10^{-5} \text{ eV/T}$)	22
μ_{orb}	Orbital magnetic moment	42
$\mu_{\text{S,D}}$	Electro-chemical potential of the source, drain electrode	25

n, m	Chiral indices of a carbon nanotube	13
$\langle N \rangle$	Average charge occupation of the quantum dot	79
N_{el}	Number of electrons on the quantum dot	35
N_{h}	Number of holes on the quantum dot	69
ω_0	Mechanical resonance frequency ($\omega_0 = 2\pi f_0$)	71
$\hat{\mathcal{P}}$	Particle-hole symmetry operator	48
P_{rf}	Nominal power of an rf-signal	78
Q	Quality factor of a resonator	71
q_{c}	Control charge ($q_{\text{c}} = C_{\text{g}} V_{\text{g}}$)	77
R_{K}	Von-Klitzing constant ($R_{\text{K}} \simeq 25812.807 \text{ V/A}$)	71
$\hat{\sigma}_{x,y,z}$	Pauli spin matrices	21
T	Sample temperature	18
\vec{T}	Translation vector in the CNT unit cell	18
$\hat{\mathcal{T}}$	Time-reversal symmetry operator	48
T_0	Residual mechanical tension at charge neutrality	76
T_{dc}	Static mechanical tension	76
T_{C}	Superconducting critical temperature	102
T_{K}	Kondo temperature	33
V_{g}	Gate voltage applied to substrate	24
V_{sd}	Bias voltage applied between source and drain contact	24
v_{F}	Fermi velocity in carbon nanotubes	43
x_{ZP}	Zero-point motion amplitude of a resonator	71
Z	Electrical impedance per unit length	103

Chapter 1

Introduction

Nano-electromechanical systems (NEMS) are promising objects both for technological advancement and fundamental physical research [Cleland, 2003]. Regarding the size they represent the next logical step after micro-electromechanical systems (MEMS), which are already widely used as force sensors resulting in very compact, sensitive and cheap devices. MEMS can by now be found in many commercial applications, from acceleration sensors in smartphones or airbag trigger systems to cantilevers in scanning microscopes.

The further miniaturization to the nano-scale reaches a limit where quantum effects become dominating. The confinement of the electronic wavefunction and charge quantization introduce novel effects, and superposition and entanglement may occur.

A basic condition for the observation of such quantum mechanical effects is the decoupling of the system from its environment, which would provide thermal energy that exceeds the energy difference of the quantum states. The lowest energetic excitation in NEMSs is the mechanical oscillation. Such that the corresponding energy scale, which is proportional to the resonance frequency, exceeds the thermal energy, experiments must target an increase of the resonance frequency in combination with low sample temperatures. The manipulation and readout of the state without inducing noise, which causes demolition of the quantum state, is only possible by the coupling of the NEMS to an additional quantum system. This can transfer excitation quanta to the object and vice versa, as recently shown by [O'Connell et al., 2008].

Here, it is shown that ultra-clean single-wall carbon nanotubes (CNTs) can act as nearly ultimate NEMSs with diameters down to 1 nm and very low mass densities combined with a high stiffness. A detailed analysis of both electronical and mechanical aspects of this system is done.

Multi-wall carbon nanotubes, a concentric arrangement of several CNTs, have been

first observed in [Radushkevich and Lukyanovich, 1952]. In 1991 S. Iijima examined the reaction products from an electric discharge on a graphite electrode and identified individual single-wall CNTs [Iijima, 1991], hollow cylinders of one-atom-thick sheets of carbon atoms arranged in a graphene lattice structure.

Following transport measurements on contacted ropes of carbon nanotubes [Bockrath et al., 1997], Tans et al. have addressed single CNTs with metallic leads for transport measurements at low temperatures [Tans et al., 1997]. Due to tunnel barriers between CNT and metal contact the originally one-dimensional electronic system is further restricted to form a quantum dot.

In these first measurements, CNTs have been deposited on a chip substrate either from a suspension or by an on-chip growth. In the first scenario, nanotubes are synthesized separately by laser evaporation or electrical discharge and collected in a solvent, while in the latter method the CNTs are grown directly on the chip, based on a chemical vapor deposition process. The various methods are listed in [Saito R.; Dresselhaus G, 1998]. For both the fabrication of electrically contacted nanotubes starts with single CNTs fixed on the substrate by van-der-Waals forces, where they have to be located for further processing. The subsequent fabrication steps include wet chemistry and lithographic processing. Both contamination by adsorbates and damaging of the nanotubes can take place. By shifting the growth process to the very last step of the fabrication the risk of damaging and contaminating the CNT is minimized, providing so-called "ultra-clean", defect-free CNTs. This improves both electronic and mechanical performance [Cao et al., 2005]. A drawback is the low yield of successfully overgrown CNTs connecting two or more contacts, which can however be resolved by fabricating large arrays of contact structures on one single chip.

On the one hand the low mass density and the high Young's modulus causes very high resonance frequencies in the MHz regime combined with very high Q -factors up to 10^5 [Hüttel et al., 2009b] for defect-free nanotubes. On the other hand clean CNTs show an unperturbed electronic structure in transport spectroscopy, since they are free of defects. This provides a clean and regular level structure where the small lateral dimensions provide an sufficiently large energy spacing, resolvable by electronic spectroscopy at cryogenic temperatures.

The thesis starts with the introduction of the new fabrication method in Regensburg to achieve such ultra-clean CNTs. This results in very clean samples, meaning the absence of contaminations affecting the electronic properties. An overview of the theoretical background of the electronic structure of CNTs and the basic physics of quantum dots (QDs) is given in Chapter 3, and the Kondo effect in such QDs is introduced (see Chapter 4). Chapter 5 presents the measurements of purely elec-

tronical properties, while Chapter 6 focuses on the mechanical characteristics and the corresponding experiments, enabled by the suspended structure of the CNT sample. Both the electronic spectroscopy and the mechanical measurements have been performed on one sample, i.e. on the same suspended CNT. The results are however obtained from different cool-downs in different cryostats. In Chapter 7, the progress on superconducting electronical resonators is presented, namely the fabrication and basic high frequency measurements. Finally the thesis is concluded and an outlook is given for possible future projects which are of high interest in the current research, building on the work presented here.

Chapter 2

Fabrication of ultra-clean suspended single-wall carbon nanotubes

In order to achieve an excellent mechanical and electrical performance of the carbon nanotubes, a modified fabrication process following [Cao et al., 2005] is used, where the CNT growth takes place as very last step in the fabrication. This avoids any contamination by contact with chemicals as e.g. lithography resist or acids and thus keeps the nanotubes as clean as possible. Since the position of the nanotubes on the chip surface is not determined via scanning electron microscope (SEM) imaging, we further avoid amorphous carbon deposition on the CNT, which stems from remaining hydrocarbon gases in the SEM chamber cracked by the highly energetic electrons.

In Fig. 2.1, an overview of the discussed fabrication steps is given, which are described in the following in detail.

Chip fabrication starts with a highly positive (boron) doped silicon substrate with a thermally grown 300 nm thick silicon oxide (SiO_x) layer on top. The degenerately doped semiconducting substrate guarantees electrical conductance even at temperatures in the mK-range. For this reason, it can be used as a global back gate.

After cleaning the surface the coarse structures are defined by optical lithography, using a mask (see Fig. 2.2) including bond pads, leads, and labeling. A photo-sensitive resist is selectively exposed by ultra-violet light changing its chemical structure. The exposed areas can then be removed by a developer solution. A 40 nm thick rhenium (Re) layer is deposited by sputtering in a UHV chamber.

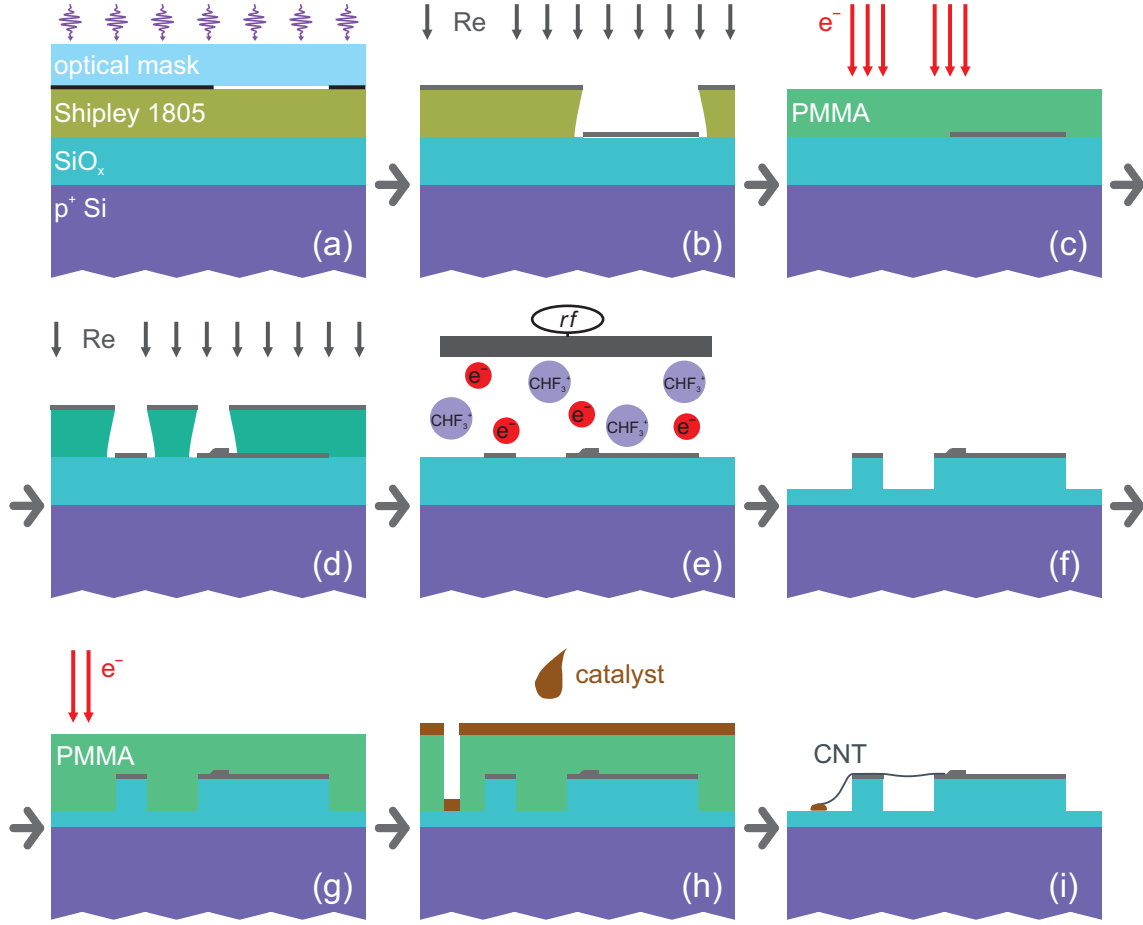


Figure 2.1: (a) The chip substrate is a highly positive doped silicon wafer with a thermally grown silicon oxide layer on top. Coarse structures are defined by optical lithography, where a photo-sensitive resist is selectively exposed by ultraviolet light and developed. (b) In an ultrahigh vacuum (UHV) chamber rhenium metal is deposited by sputtering. (c) Fine structures later used as contact electrodes, aligned to the coarse ones, are defined by electron beam lithography (EBL) in a scanning electron microscope (SEM) and (d) again metallized with rhenium. (e) Reactive ion etching (RIE) etches 160 nm SiO_x selectively and anisotropically. In (f) the final contact structure is shown with trenches of 200 nm depth and widths between 200 and 800 nm. (g,h) Catalyst, required to induce the growth reaction is locally deposited by exposing small areas in an additional EBL step. The catalyst suspension is drop-cast onto the chip. Removing the surplus catalyst in a lift-off process leaves solely small islands thereof on the substrate. (i) In the very last step the growth process takes place in hydrogen/ methane atmosphere heated up to 900°C. Nanotubes grow in arbitrary direction and fall over contact electrodes.

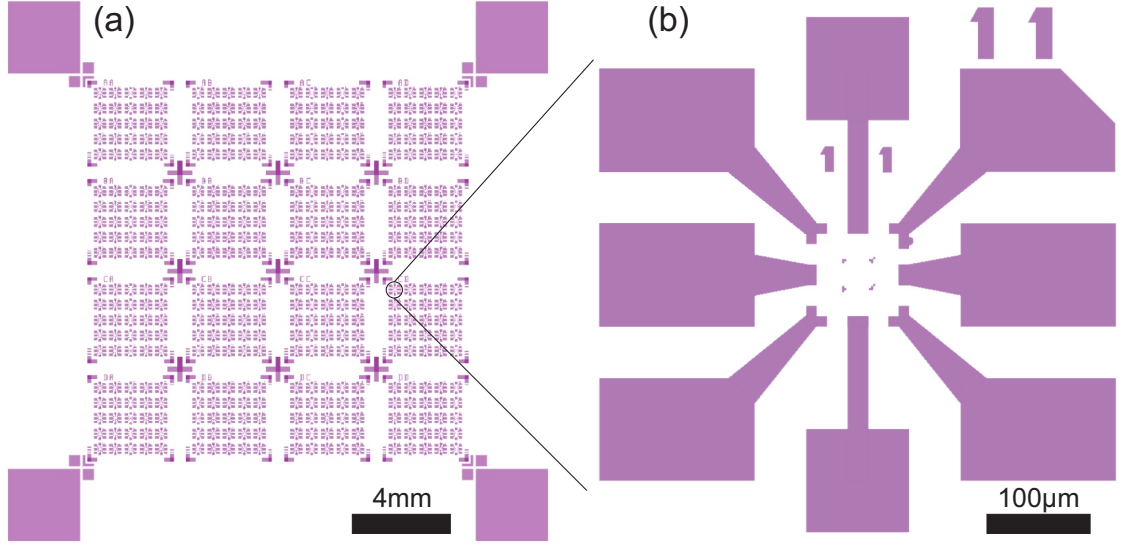


Figure 2.2: (a) Optical mask structure to define bond pads, coarse leads and labeling on a 16×16 mm chip. (b) Zoom on a single electrode structure containing eight bond pads.

Afterwards, the chip is placed in hot acetone in order to remove the surplus metal on top of the undeveloped resist.

Then, the fine structures are aligned in the SEM with respect to the coarse ones. In an electron beam lithography (EBL) step, a PMMA resist is exposed by a focused electron beam scanning the defined structures. In this EBL step all the inner parts including the later contacts to the CNT are exposed with overlap to the optically defined structures. Since the nanotube growth starts at a catalyst particle and the nanotubes grow in a non-controllable, arbitrary direction, a circular electrode structure has been designed to increase the probability for an overgrowth process, which is shown in Fig. 2.3. Several electrodes are arranged with varied distances to obtain different suspended segment lengths. Additionally, due to the circular symmetry the suspended length is better defined since the nanotube tends to grow radially outwards. Again the resist is developed and a 40 nm Re layer is deposited with a subsequent lift-off step.

To guarantee freely suspended CNTs bridging two or more contacts the trenches between the circular metal electrodes have to be deepened. This is done by reactive ion etching (RIE), where plasma enhanced dry etching anisotropically removes 160 nm of the SiO_x while the metal is nearly unaffected and works as etching mask. At this status all chip structures are defined, namely several contacts with 200 nm deep and 200 nm to 800 nm wide trenches in between, on a single 4×4 mm chip. Figure 2.4 shows an SEM micrograph with tilted stage. Catalyst particles and a CNT

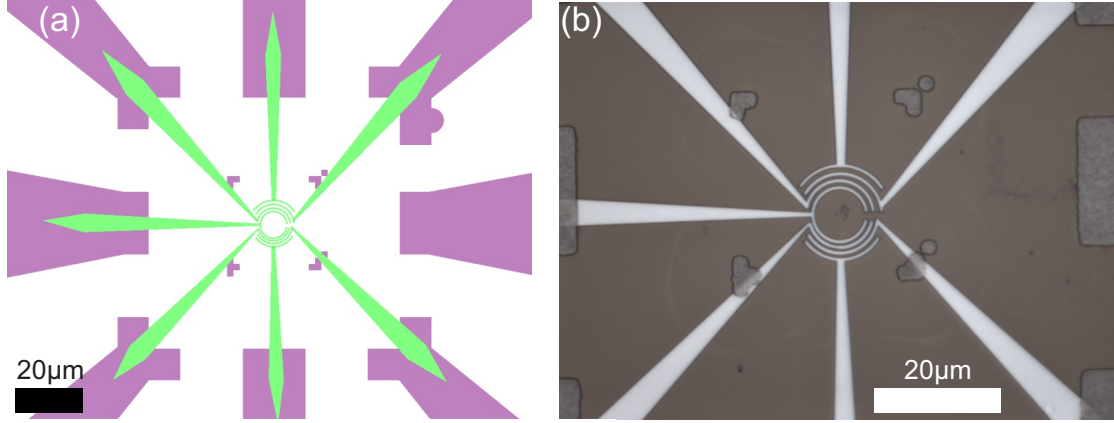


Figure 2.3: (a) EBL design for the CNT electrode geometry. (b) Optical microscope picture of circular contact structure aligned to coarse optical mask structures.

are schematically drawn, depicting an ideal situation of a single CNT contacted by several electrodes.

For the CNT growth process a catalyst, composed of transition metal oxide and metalorganic particles suspended in methanol, is needed. The exact composition is listed in Appendix A.4. We use an additional EBL step to place a small amount of catalyst in the center of the circular structures. A drop of the catalyst suspension is cast onto the developed resist and dried on the hot plate to evaporate the methanol. In the following lift-off process the catalyst is removed except for small clusters placed at the structure centers, as illustrated in Fig. 2.4.

The CNT growth process takes place in a quartz tube in an oven heated up to 900°C while a gas mixture of hydrogen and methane is flowing over the sample. Again, the detailed recipe is listed in Appendix A.5. At the catalyst the methane decomposes and the carbon crystallizes building up the CNT, which grows upwards until it tilts and attaches to the substrate. Van-der-Waals forces fix the CNT at the substrate surface. Despite several attempts in our lab to guide the CNT growth direction using a modified process with a low gas flow rate, in order to obtain laminar flow [Jin et al., 2007], one still observes arbitrary growth directions. Thus the yield of working structures differs in general from sample to sample.

In order to identify the working structures SEM imaging is avoided, since an electron beam focused on a CNT deposits amorphous carbon on the nanotube, as has been shown in Raman spectroscopy. Instead, we solely measure the electric resistance between all electrodes, allowing us to distinguish between contacts connected by a CNT and open- or short-circuited ones. The promising ones are further tested by measuring the back gate dependence of the conductance, and the most auspicious

samples are mounted into the cryostat for low-temperature transport measurements. SEM pictures as shown in Fig. 2.5 are taken only after all low-temperature transport measurements.

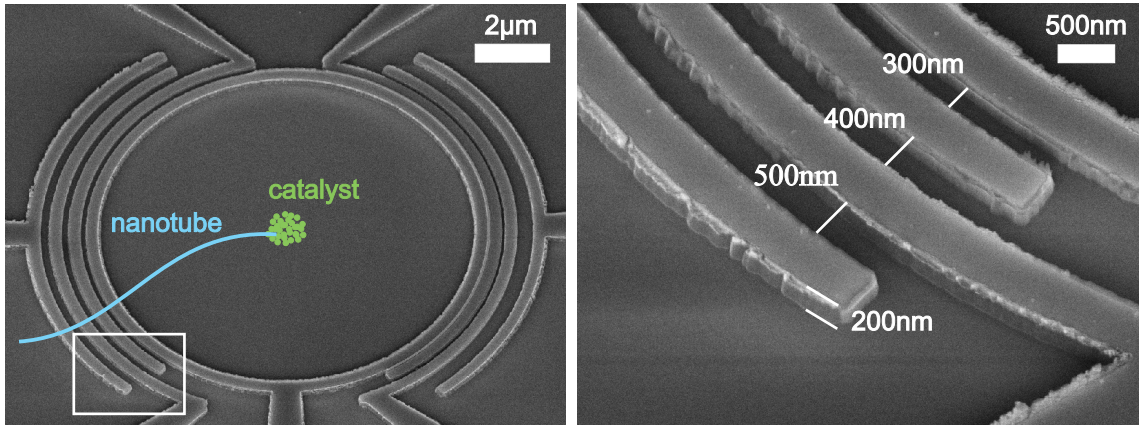


Figure 2.4: Left: Tilted SEM picture of the electrode structure with indicated possible catalyst and CNT position. Right: Zoom on the area marked in the left image with a white rectangle showing the circular electrode geometry in detail.

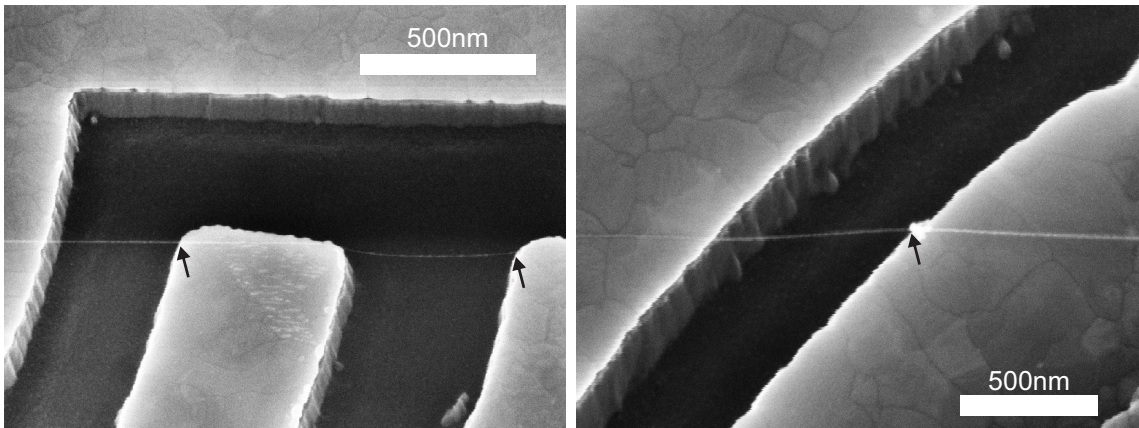


Figure 2.5: Tilted SEM picture of CNTs suspended between rhenium contacts after a successful overgrowth process.

Chapter 3

Structure and electronic properties of carbon nanotubes

Carbon nanotubes are one allotrope of carbon besides graphite (graphene), diamond and fullerenes. This work focuses on single-wall CNTs, which were discovered by Iijima in 1991 [Iijima, 1991] in the products of an arc discharge at graphite electrodes by transmission electron microscope imaging. Other fabrication methods include laser evaporation by a pulsed laser beam focused on a graphite substrate and chemical vapor deposition (CVD) [Saito R.; Dresselhaus G, 1998]. Former experiments have shown that the last mechanism provides the highest quality in terms of lowest defect density and the highest yield of single-wall CNTs. Additionally, it is compatible with pre-defined on-chip structures, as shown in Chapter 2.

CNTs rapidly became interesting for transport measurements due to their quasi one-dimensionality combined with a perfect regular lattice structure in the ideal case of a clean CNT. At cryogenic temperatures the effectively one-dimensional electronic system¹ can be further reduced by tunnel barriers induced by metal contacts, to define quantum dots (QDs), so-called "artificial atoms". QDs based on CNTs provide an interesting internal structure, having some degrees of freedom like spin and valley quantum numbers with a pronounced shell configuration. The CNT macro-molecule with its extremely small diameter (≈ 1 nm) provides a highly regular system with relatively high quantum confinement energies among mesoscopic systems.

¹For realistic nanotube diameters solely the lowest transversal subband is energetically accessible in transport measurements at low temperatures, restricting free propagation only along the nanotube axis.

3.1 From graphene to carbon nanotubes

In a first approximation the physical properties of CNTs can be deduced from those of graphene, a one-atom thick layer of carbon atoms arranged in a honeycomb lattice. This layer, "rolled up" along the so-called chiral vector \vec{C} , forms a hollow cylinder with a typical diameter of few nanometers. Thus, as a first step we will start with the physics of graphene, later deducing the properties of CNTs.

Graphene is formed by a hexagonal arrangement of carbon atoms, connected by σ -bonds of sp^2 -hybridized orbitals at 120° angles in the plane (see Fig. 3.1(a)). These orbitals of neighboring atoms overlap forming molecular σ and σ^* bands, which do not contribute to transport, since they are far away from the Fermi energy. The remaining p_z orbital is aligned perpendicular to the honeycomb plane, forming delocalized bonding π and anti-bonding π^* bands.

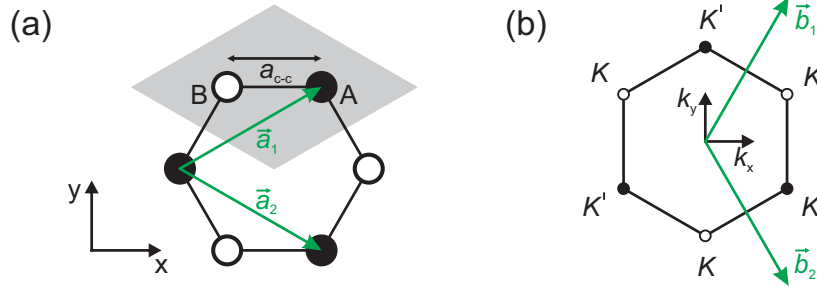


Figure 3.1: (a) Graphene lattice in the real space spanned up by the unit vectors \vec{a}_1, \vec{a}_2 . The bond length between the two carbon atoms A, B in the unit cell (shaded gray) is $a_{C-C} = 1.42 \text{ \AA}$. (b) First Brillouin zone of graphene in the reciprocal space with the unit vectors \vec{b}_1, \vec{b}_2 . The six symmetry points are labeled K and K' .

As depicted in Fig. 3.1, the unit cell of the hexagonal lattice of graphene is spanned by unit vectors

$$\vec{a}_1 = \left(\frac{\sqrt{3}}{2}a, \frac{a}{2} \right) \quad \text{and} \quad \vec{a}_2 = \left(\frac{\sqrt{3}}{2}a, -\frac{a}{2} \right). \quad (3.1)$$

It contains two carbon atoms, labeled A and B in the figure, situated at the positions $(0, 0)$ and $\frac{1}{3}(\vec{a}_1 + \vec{a}_2) = (a/\sqrt{3}, 0)$. The lattice constant is

$$a = |\vec{a}_1| = |\vec{a}_2| = a_{C-C} \cdot \sqrt{3} = 2.46 \text{ \AA}, \quad (3.2)$$

where $a_{C-C} = 1.42 \text{ \AA}$ is the carbon atom distance, i.e. the length of the σ -bond. In the reciprocal lattice the corresponding unit vectors \vec{b}_1, \vec{b}_2 , fulfilling the orthogonality condition $\vec{b}_i \cdot \vec{a}_j = 2\pi\delta_{ij}$, are

$$\vec{b}_1 = \left(\frac{2\pi}{\sqrt{3}a}, \frac{2\pi}{a} \right) \quad \text{and} \quad \vec{b}_2 = \left(\frac{2\pi}{\sqrt{3}a}, -\frac{2\pi}{a} \right). \quad (3.3)$$

In the tight binding approximation for the delocalized p_z orbitals using Bloch waves, the electronic structure of the valence (π) and conduction (π^*) band of the graphene layer can be calculated. After a further approximation that the overlap integral becomes zero (Slater-Koster scheme) one obtains the simplified dispersion relation of a graphene layer, plotted in Fig. 3.2 (for details see [Saito R.; Dresselhaus G, 1998]):

$$E_{\text{graphene}}(k_x, k_y) = \pm \left[1 + 4 \cos\left(\frac{\sqrt{3}k_x a}{2}\right) \cos\left(\frac{k_y a}{2}\right) + 4 \cos^2\left(\frac{k_y a}{2}\right) \right]^{1/2}. \quad (3.4)$$

Due to the two π electrons per unit cell the lower π band is fully occupied, while the π^* band is empty. However, the most remarkable electronic property of graphene is the "zero-energy band gap" at the six corners of the Brillouin, the so-called K -points. Only two are independent, labeled K, K' , while the others are connected by reciprocal lattice vectors. In the low energy limit the dispersion at this K -points is linear, as can be seen in the zoom in Fig. 3.2(b). Due to these features of the dispersion relation graphene exhibits quasi-metallic behavior.

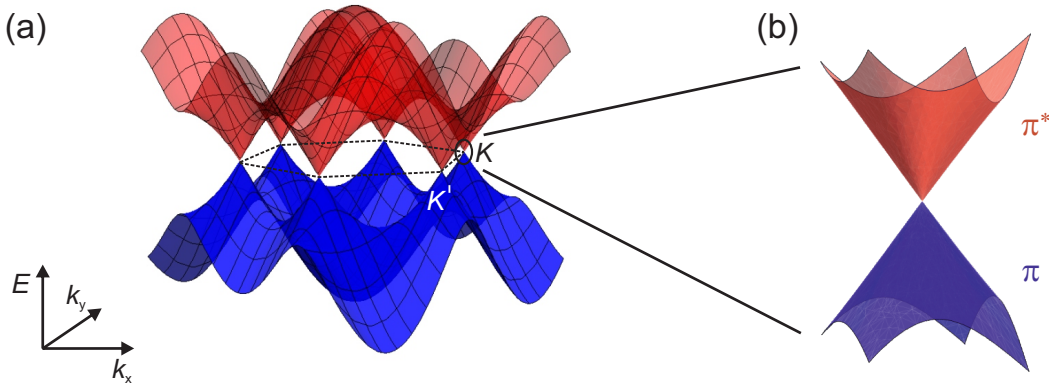


Figure 3.2: (a) Energy dispersion of the π and π^* bands in graphene calculated with Eq. 3.4. (b) Detail view of one so-called Dirac cone, which are located at the K and K' points in the Brillouin zone. Here the valence (π) and conduction (π^*) bands touch and the dispersion relation is linear.

There is a large amount of possibilities how a CNT can be formed from a graphene sheet. The chiral vector $\vec{C} = n\vec{a}_1 + m\vec{a}_2 \equiv (n, m)$, along which a CNT is rolled up, uniquely characterizes each of these possibilities. By definition, owing to the hexagonal symmetry, the range $0 \leq |m| \leq n$ for the parameters m, n is sufficient. The length of the chiral vector $|\vec{C}| = a\sqrt{n^2 + m^2 + nm}$ corresponds to the circumference of the nanotube.

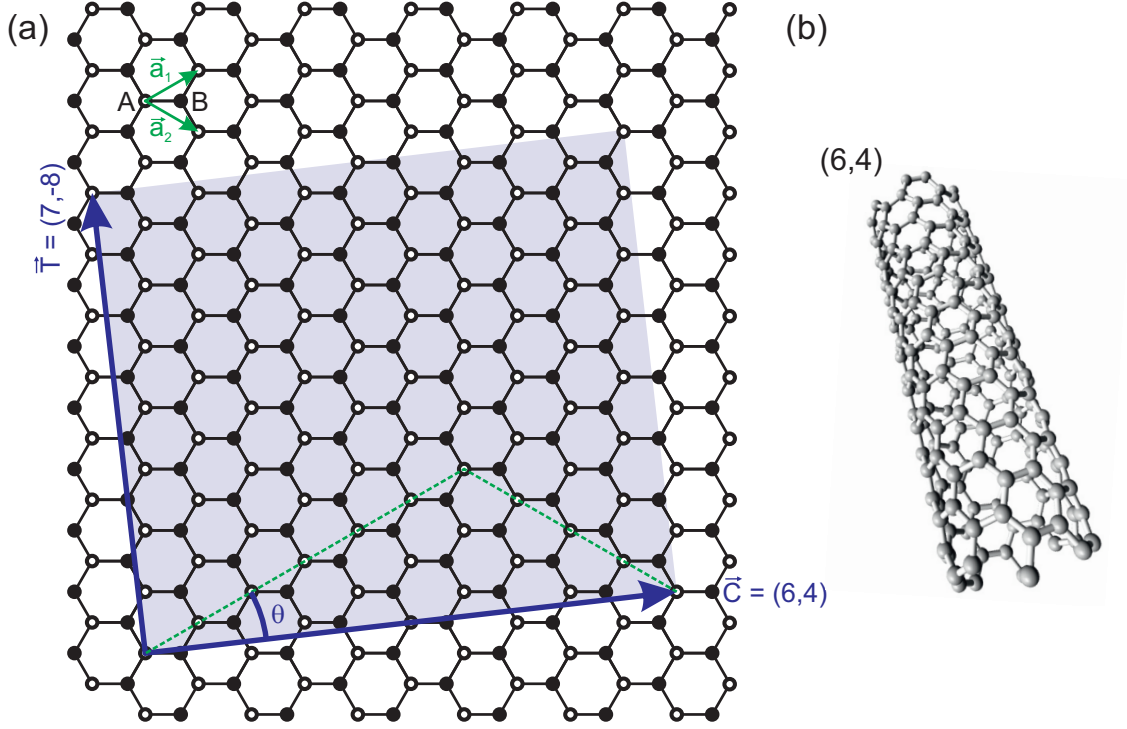


Figure 3.3: (a) Schematic drawing of the graphene lattice. The blue arrows define the unit cell of a (6,4) CNT, spanned by the chiral vector \vec{C} and the perpendicular vector \vec{T} . (b) Sketch of a rolled-up (6,4) nanotube segment generated with *Nanotube Modeler* (© JCrystalSoft, 2013).

The angle between the chiral vector \vec{C} and \vec{a}_1 is called chiral angle θ . It is restricted to the range $0 \leq |\theta| \leq 30^\circ$ due to the hexagonal symmetry of the graphene lattice. This chiral angle θ can be expressed in terms of the chiral indices as

$$\cos(\theta) = \frac{\vec{C} \cdot \vec{a}_1}{|\vec{C}| |\vec{a}_1|} = \frac{2n + m}{2\sqrt{n^2 + m^2 + nm}}. \quad (3.5)$$

In particular, zigzag and armchair nanotubes correspond to $\theta = 0^\circ$ ($m = 0$) and $\theta = 30^\circ$ ($m = n$), respectively.

To define a carbon nanotube unit cell one also needs a vector that gives the periodicity of the CNT in direction of its axis – the so-called translation vector

$$\vec{T} = t_1 \vec{a}_1 + t_2 \vec{a}_2, \quad (3.6)$$

with integers t_1 and t_2 , which can be expressed by

$$t_1 = \frac{2m + n}{d_R} \quad \text{and} \quad t_2 = -\frac{2n + m}{d_R}, \quad (3.7)$$

where d_R is the greatest common divisor of $(2m + n)$ and $(2n + m)$.

With the unit cell of a nanotube, spanned by \vec{C} and \vec{T} , the structure of the nanotube is unambiguously defined. As an example, Fig. 3.3 shows the unit cell of a $(n, m) = (6, 4)$ CNT, with $d_R = 2$, $t_1 = 7$ and $t_2 = -8$.

”Rolling up” a graphene sheet has consequences for the electronic structure of the resulting single-wall carbon nanotube (SWCNT). A novel boundary condition is introduced. Due to the finite circumference of the CNT the wave vector in \vec{C} direction k_\perp becomes quantized, while the longitudinal wave vector in \vec{T} direction k_\parallel remains continuous as long as one assumes infinitely long nanotubes.

Due to this boundary condition (the phase of the wave function has to be identical modulo 2π after one circulation) the energy dispersion relation of each band of graphene (π, π^*) collapses into one-dimensional parallel subbands, also called transversal modes, with spacing

$$\Delta k_\perp = \frac{2\pi}{|\vec{C}|}. \quad (3.8)$$

Thus only discrete wave vectors along the \vec{C} -direction are allowed, while a continuous dispersion in the nanotube axis direction, along \vec{T} , remains. Restricting to one subband the Brillouin zone becomes one-dimensional. The one-dimensional band structure of a (n, m) nanotube is given by the zone-folding relation deduced from the two-dimensional band structure of graphene:

$$E(k_\parallel, \mu) = E_{\text{graphene}} \left(k \frac{\vec{K}_2}{|\vec{K}_2|} + \mu \vec{K}_1 \right). \quad (3.9)$$

Here k_\parallel is the longitudinal wave vector ($-\pi/T < k_\parallel < \pi/T$; $T = |\vec{T}|$ is the translation period of the nanotube in Eq. 3.6) and μ is a discrete quantum number ($\mu = 1, 2, \dots, N$ where N is the number of carbon pairs in the unit cell of the nanotube). An example for the collapse of the dispersion is shown in the Fig. 3.4.

The vectors \vec{K}_1 and \vec{K}_2 are expressed by the reciprocal lattice vectors \vec{b}_1 and \vec{b}_2 of the graphene sheet as

$$\vec{K}_1 = \frac{-t_2 \vec{b}_1 + t_1 \vec{b}_2}{N} \quad \text{and} \quad \vec{K}_2 = \frac{m \vec{b}_1 - n \vec{b}_2}{N}. \quad (3.10)$$

If a K -point, where the valence and the conduction band of graphene are degenerate, fulfills the boundary condition, the CNT is metallic. A metallic behavior can for instance be found in the case of a $(3, 3)$ CNT in Fig. 3.4 where the line cuts intersect the K -points. Otherwise, for low energies it has approximately parabolic bands separated by an energy gap, and the nanotube displays semiconducting behavior.

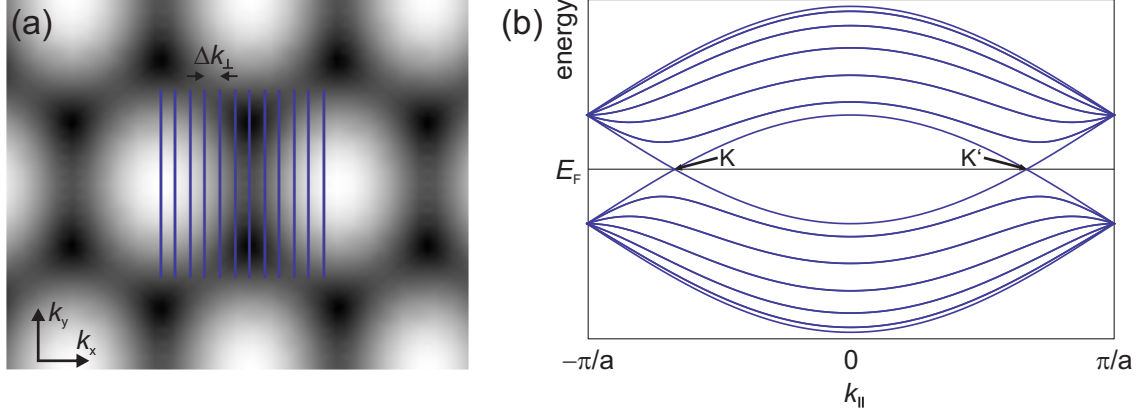


Figure 3.4: (a) Rolling up the CNT leads to a restriction of allowed wave vectors. The case of a (3,3) CNT is indicated as blue lines on top of the graphene dispersion gray scale plot. (b) The corresponding energy dispersion for the one-dimensional subband of a (3,3) CNT shows a degeneracy at the K and K' point. This causes metallic behavior.

This behavior can be traced even by room temperature transport measurements where nanotubes are electrically contacted on a substrate and capacitively coupled to a gate. Applying a voltage to the gate changes the chemical potential of the electrons in the nanotube shifting them with respect to the Fermi energy of the leads. Figure 3.5 displays a sketch of the resulting typical dependence of the conductance on the gate voltage at room temperature. In the case of a metallic nanotube (Fig. 3.5(a)) the conductance does not depend on the back gate voltage, since no band gap exists: one CNT subband intersects the K or K' Dirac point. The condition for metallic conduction can be derived from Eq. 3.8. One obtains for the chirality (n, m) the condition

$$n - m = 3q, \quad (3.11)$$

where q is an integer number. As a consequence, following this model, statistically one third of the single-wall carbon nanotubes are metallic, two third are semiconducting. For semiconducting CNTs, the conductance drops to zero in the band gap (Fig. 3.5(c)).

This zone-folding approximation neglects curvature effects like changing bond lengths and not perfectly parallel p_z - orbitals. Taking the curvature into consideration, only armchair nanotubes ($n = m$) remain really metallic, the other ones fulfilling Eq. 3.11 develop a small band gap E_g leading to a dip in $G(V_g)$ at room temperature as depicted in Fig. 3.5(b), since $E_g \simeq k_B T$. For more details see [Charlier et al., 2007]. A further effect of the curvature is the induced spin-orbit coupling in CNT, which is almost absent near Dirac points in graphene [Huertas-Hernando et al., 2006]. The

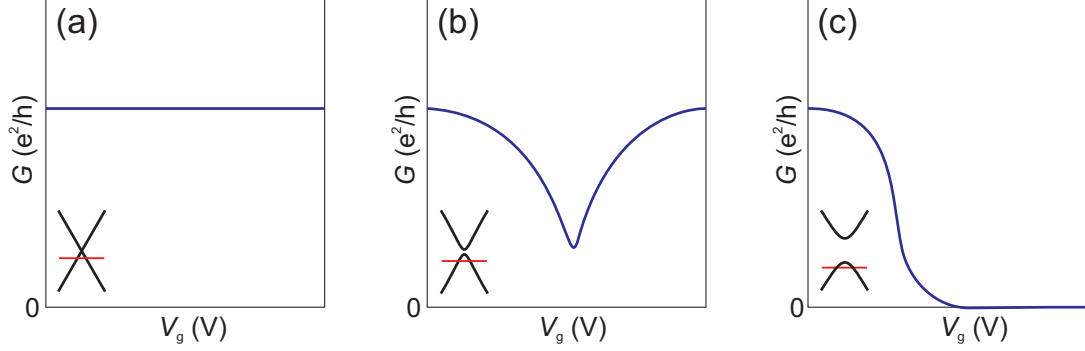


Figure 3.5: Sketches of conductance traces $G(V_g)$ at room temperature for (a) metallic (b) small-bandgap and (c) semiconducting CNTs. The insets depict the lowest subbands for the respective type of CNT. These are shifted by the gate voltage V_g with respect to the electro-chemical potential of the leads (red line).

spin-orbit coupling can be revealed by transport spectroscopy, as e.g. demonstrated in the Chapters 5.1 and 5.2.

3.2 Electronical properties of carbon nanotube quantum dots

The one-dimensional CNT band structure can be further reduced by forming a so-called quantum dot (QD) [Tans et al., 1997], a conducting island separated from leads by tunnel barriers.

Different methods exist to create QDs, e.g. self-assembled metal clusters, lateral QDs which are electro-statically defined in two-dimensional electron gases (2DEG), or contacted nanowires. In this work, the quantum dot is defined in the suspended part of a carbon nanotube at low temperatures. In the following the relevant QD theory is deduced starting with a metallic island, which forms a classical single electron transistor, where the number of charges is quantized. Reducing the charge carrier density leads to an increase of the size quantization induced energy spacing giving rise to quantum Coulomb blockade.

A survey of the different transport regimes is given in the Table 3.1.

3.2.1 From classical to quantum Coulomb blockade

We assume an electrically isolated conductor, which is connected to leads by tunnel barriers. In Fig. 3.6(a) a replacement circuit is depicted. For electronical transport measurements the QD has to be coupled to source (S) and drain (D) leads enabling

(a) $\Delta\epsilon \lesssim e^2/C_\Sigma \ll k_B T$	no discreteness of charge due to: <ul style="list-style-type: none"> • temperature too high • quantum dot not small enough • tunneling resistance too low
(b) $\Delta\epsilon \ll k_B T \ll e^2/C_\Sigma$	classical or metallic Coulomb blockade regime: <ul style="list-style-type: none"> • many levels contribute to tunneling • many levels excited by thermal fluctuations
(c) $k_B T \ll \Delta\epsilon < e^2/C_\Sigma$ $\hbar\Gamma \ll k_B T$	quantum Coulomb blockade regime: <ul style="list-style-type: none"> • only one or a few levels participate in transport • width of conductance peaks set by temperature

Table 3.1: Transport regimes for a conducting island coupled to leads.

the modification of the QD charging state. The coupling is provided by tunnel barriers between leads and QD with tunnel rates Γ_S, Γ_D , which can be modeled as resistors parallel to capacitors C_S, C_D . In order to modify the electro-chemical potential of the electrons on the island a gate voltage can be applied to a nearby gate electrode (G), which is capacitively coupled to the quantum dot (QD) via the capacitance C_g .

Depending on the relevant energy scales one has access to different transport regimes. As long as the thermal energy is dominating the tunnel barriers will not be effective and the transport through the conducting island will behave in a classical way, the charge quantization will not be noticed. This case is listed in (a) of the Table 3.1.

To obtain charge quantization on the island its size has to decrease leading to a low capacitance. As consequence, the electrostatic charging energy $E_C = e^2/2C_\Sigma$ will reach values of some tens of meV exceeding the thermal energy $E_{th} = k_B T$ at low temperatures, i.e. $k_B T \ll E_C = e^2/2C_\Sigma$. Here C_Σ is the total capacitance of the conducting island. In a setup as illustrated in Fig. 3.6(a), the total capacitance is given by the sum of gate C_g , source C_S , and drain C_D capacitance plus parasitic ones: $C_\Sigma = C_g + C_S + C_D + C_{env}$. The consequence is an electrostatic suppression of the current due to Coulomb interaction which is called *Coulomb blockade*. Here, the Coulomb repulsion prevents an additional electron from tunneling onto the QD. A further requirement for the occurrence of Coulomb blockade is that the tunnel resistances from the source and drain lead $R_{S,D}$ to the dot must be bigger than the quantum resistance $R_{S,D} \gg R_K \simeq 25.8 \text{ k}\Omega$ in order to suppress quantum fluctuations of the charge on the island. If these conditions are fulfilled the current through the island is blocked by the Coulomb repulsion and the charge on the dot is fixed, as has been first observed in metallic islands [Grabert et al., 1993], [Ralph et al., 1995].

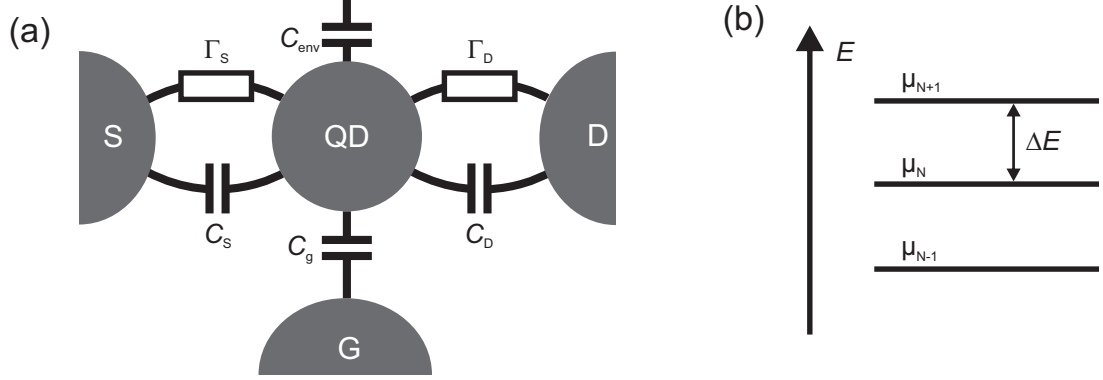


Figure 3.6: (a) Replacement circuit of a quantum dot coupled to a source (S) and a drain (D) contact by tunnel barriers with tunnel rates $\Gamma_{S,D}$ and capacitances $C_{S,D}$. A gate (G) is capacitively coupled to the QD to change the electro-chemical potential of the QD states. (b) Discrete "charging levels" in a classical QD with equidistant level spacing $\Delta E = E_C = e^2/2C$ given by the classical charging energy.

Due to the small Fermi wavelength in metallic islands the energy level separation $\Delta\epsilon$ is usually much smaller than the charging and thermal energy, i.e. $\Delta\epsilon \ll k_B T \ll E_C$, and can be neglected. The charging energy is assumed to be independent of the charging state and thus the energy required to put an additional electron on the dot is constant. This is indicated in Fig. 3.6(b) showing the "charging levels" which are equally spaced by the charging energy $\Delta E = E_C$.

The conditions for this classical Coulomb blockade, as summarized in Table 3.1(b), can be technologically met nowadays in terms of micro- and nano-fabrication and by dilution cryostats with temperatures down to $T \simeq 10$ mK.

If the density of states n_s of the QD is low, as e.g. in two-dimensional semiconductors, the Fermi wavelength λ_F can reach values around 50 nm, since $\lambda_F = \sqrt{2\pi/n_s}$ [Beenakker, 1991], [Kouwenhoven et al., 1997], and the quantum mechanical quantization energy $\Delta\epsilon$ can attain the same order of magnitude as the charging energy (see Table 3.1(c)). Then the energy differences ΔE are not equal anymore but now consist of both the classical charging energy E_C , which is constant within the so-called constant interaction model [Glazman and Shekhter, 1989], [McEuen et al., 1991], plus the single-particle level spacing $\Delta\epsilon$, which is required to reach the next unoccupied quantum level. The latter one originates from the quantum mechanical size quantization in all three dimensions and is in general dependent on the charging state. Further details of the QD physics can be found in [Kouwenhoven et al., 1997]. In the simplest model assuming twofold spin-degenerate states and neglecting any exchange interactions, one expects a finite $\Delta\epsilon$ only for every second electron induc-

ing a transition of the spin quantum number $S = 0 \rightarrow 1/2$. This is the case of $SU(2)$ symmetry.

In the special case of CNTs, besides the spin degeneracy additionally the KK' valley degree of freedom has to be taken into account, which originates from the underlying graphene lattice. For the highly symmetric case the QD levels in CNTs are thus fourfold both spin and valley degenerate, as has been seen in experiments [Liang et al., 2002], [Sapmaz et al., 2005]. As shown in Fig. 3.7, the longitudinal quantization leads to spin-degenerate levels equidistant in k_{\parallel} direction for both valleys. If the levels are symmetric in the different valleys (K, K'), the respective levels are energetically equal leading to fourfold degeneracy. Hole and electron states are separated by the band gap E_g .

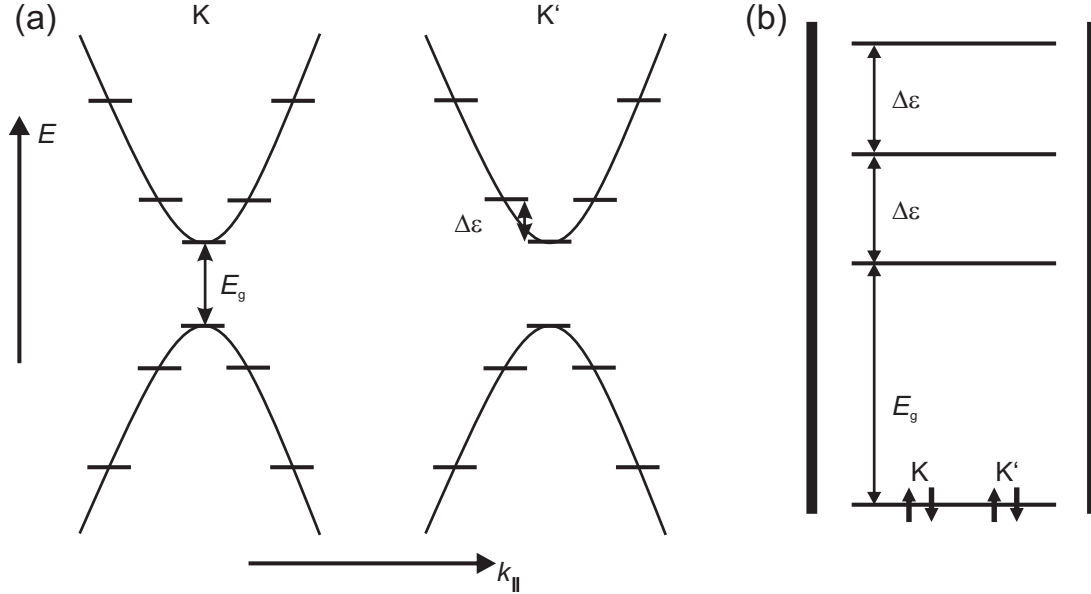


Figure 3.7: (a) Lowest transversal subbands of K and K' valley for a maximum degenerate ($\Delta_{SO} = \Delta_{KK'} = 0$) semiconducting CNT with indicated quantum dot levels caused by the longitudinal quantization of the one-dimensional nanotube. (b) Energy level diagram in an exemplary CNT QD with spin- and valley- degenerate longitudinal modes, indicated by the spin-up and spin-down arrows for the K and K' valley. The separation of hole and electron levels is given by the band gap size E_g and $\Delta\epsilon$ represents the "quantum energy". Note that the diagram does not include the electrostatic charging energy which has to be paid for each additional electron on the QD.

3.2.2 Influence of spin-orbit coupling, KK' -mixing, and magnetic fields on the quantum dot levels

In the following, based on the $SU(4)$ symmetry, as discussed above, we will now also take into account symmetry breaking. The CNT levels are modeled without any electron-electron interactions, assuming only one electron occupying a longitudinal mode.

It is sufficient in a good approximation to use a minimal Hamiltonian for a single longitudinal mode of a CNT-QD. Including spin-orbit coupling, KK' -mixing and a magnetic field forming an angle φ with the nanotube axis. Then, the Hamiltonian reads

$$\begin{aligned} \hat{H}_{\text{CNT}} = & \varepsilon_d \hat{I}_\sigma \otimes \hat{I}_\tau + \frac{\Delta_{KK'}}{2} \hat{I}_\sigma \otimes \hat{\tau}_z + \frac{\Delta_{\text{SO}}}{2} \hat{\sigma}_z \otimes \hat{\tau}_x + \\ & + \frac{1}{2} g_s \mu_B |\vec{B}| (\cos \varphi \hat{\sigma}_z + \sin \varphi \hat{\sigma}_x) \otimes \hat{I}_\tau + g_{\text{orb}} \mu_B |\vec{B}| \cos \varphi \hat{I}_\sigma \otimes \hat{\tau}_x. \end{aligned} \quad (3.12)$$

The basis is formed by the states $\{|a \uparrow\rangle, |b \uparrow\rangle, |a \downarrow\rangle, |b \downarrow\rangle\}$, where

$$|a\rangle = \frac{|K\rangle + |K'\rangle}{\sqrt{2}}, \quad |b\rangle = \frac{-|K\rangle + |K'\rangle}{\sqrt{2}} \quad (3.13)$$

are the anti-bonding and bonding combination of the different valley eigenstates $|K\rangle$ and $|K'\rangle$, respectively. The operators $\hat{\tau}_i$ and $\hat{\sigma}_i$ ($i = x, y, z$) act in the valley and spin spaces, respectively, such that $|a\rangle, |b\rangle$ are the eigenstates of $\hat{\tau}_z$, while $|\uparrow\rangle, |\downarrow\rangle$ are the eigenstates of $\hat{\sigma}_z$. Spin-orbit interaction splits the fourfold degeneracy, forming two Kramers doublets at $B = 0$ with energy spacing Δ_{SO} . These are further hybridized by the valley mixing, which is typically referred to disorder but can also be induced by the axial boundary conditions. The pure valley and spin states are restored in the high field range $g_s \mu_B |\vec{B}| \gg \Delta_{\text{SO}}, \Delta_{KK'}$.

The first term in the Hamiltonian 3.12 gives the reference energy ε_d of the considered longitudinal mode, the second term takes into account the valley mixing with the corresponding energy $\Delta_{KK'}$. The last term in the first line incorporates the spin-orbit interaction energy Δ_{SO} . In the second line the effect of a magnetic field is included, where the first term stands for the Zeeman effect, while the last one takes into account the Aharonov-Bohm effect caused by the cylindrical topology of the CNT and the parallel component of the field.

The magnetic field dependence of the eigenstates both in perpendicular ($\phi = \pi/2$) and parallel ($\phi = 0$) orientation to the nanotube axis are obtained by the diagonalization of the Hamiltonian 3.12 and is shown in Fig. 3.8 for different values of the parameters Δ_{SO} and $\Delta_{KK'}$. In this figure, the behavior of the states in a magnetic field is plotted for perpendicular orientation of the magnetic field to the CNT axis

on the left side, and for parallel orientation on the right side.

In the zero field case with $\Delta_{\text{SO}} = \Delta_{\text{KK}'} = 0$, Fig. 3.8(a), the quantum state is four times degenerate. In finite field the levels split linearly according to their magnetic moment. The orbital magnetic moment $g_{\text{orb}}\mu_{\text{B}}$ depends on the CNT diameter and is typically bigger than the spin magnetic moment $g_{\text{s}}\mu_{\text{B}}$. In Fig. 3.8 the orbital g -factor is set to twice the spin g -factor resulting in steeper slopes of the state with parallel aligned spin and orbital magnetic moment in the parallel magnetic field. While in the perpendicular case only the Zeeman splitting of valley degenerate states occurs, in the parallel orientation also the orbital momentum couples to the field with an overlying Zeeman splitting.

For finite spin-orbit coupling $\Delta_{\text{SO}} > 0$, depicted in Fig. 3.8(b), the quadruplet splits at $B = 0$ into so-called Kramers doublets with energy spacing Δ_{SO} . As a consequence of the spin-orbit coupling the spin perpendicular to the nanotube is not a good quantum number anymore, since the spin aligns with the orbital moment in the direction of the nanotube axis. In parallel field the different slopes of the states show the distinct ways to couple spin and the valley quantum numbers K, K' .

In Fig. 3.8(c) the finite KK' -mixing leads again to a splitting into doublets at zero field with spacing $\Delta_{\text{KK}'}$. The situation becomes even more complicated in 3.8(d) for both finite $\Delta_{\text{KK}'}$ and Δ_{SO} , where the doublet spacing Δ at zero field is a function of both energies, $\Delta = \sqrt{\Delta_{\text{KK}'}^2 + \Delta_{\text{SO}}^2}$. Additionally, in both field orientations an anti-crossing mixes the states. This case will be discussed in more detail in Chapter 5.1 and 5.2.

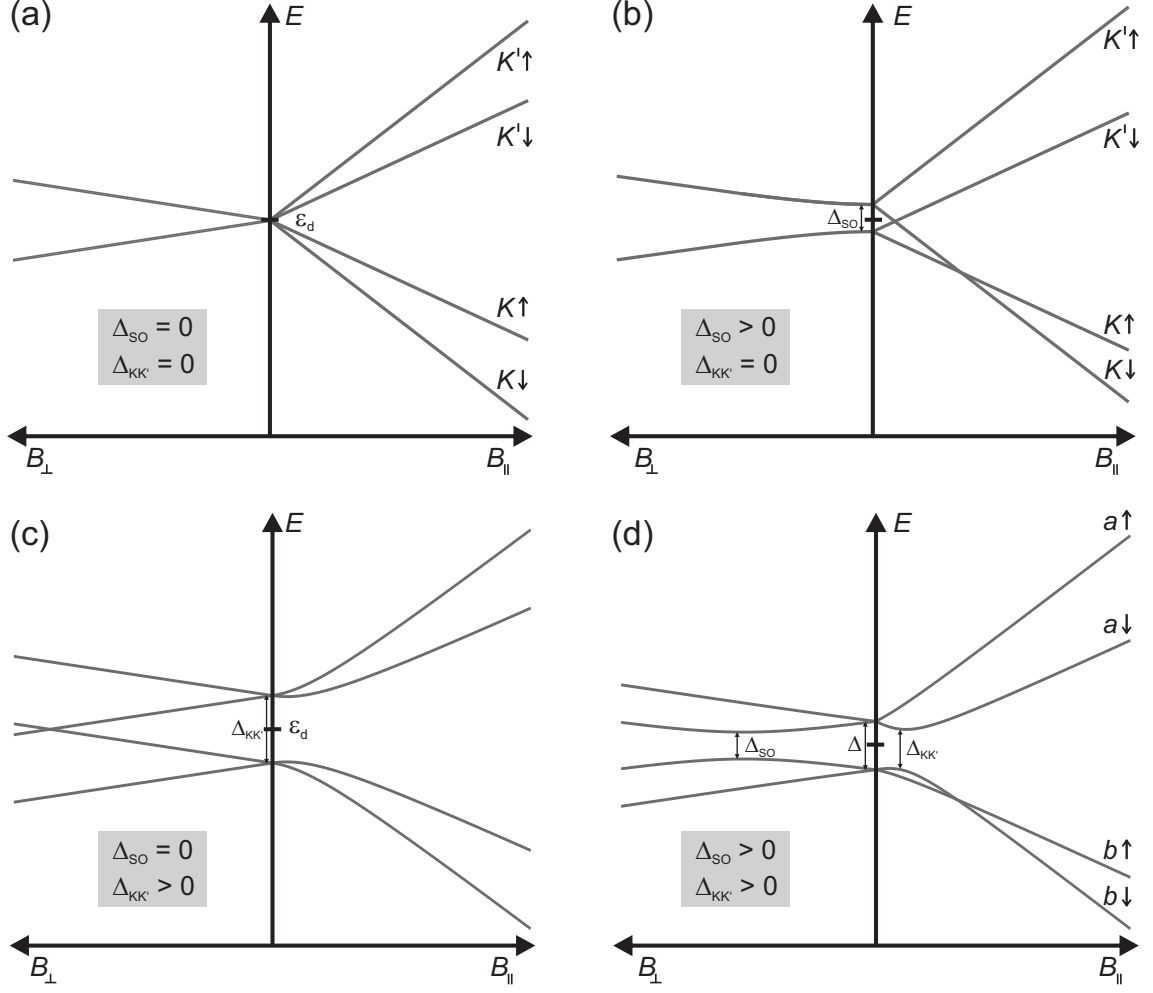


Figure 3.8: Single particle level spectrum of a CNT longitudinal mode located at the reference energy ε_d in an external magnetic field perpendicular (B_{\perp}) and parallel (B_{\parallel}) to the CNT axis. (a) Fourfold degenerate ground state manifested in an $SU(4)$ symmetry at $B = 0$. (b) The degeneracy is lifted by spin-orbit coupling Δ_{SO} . Two Kramers pairs occur at $B = 0$. (c) Finite KK' -mixing also lifts the degeneracy forming Kramers pairs with energy spacing $\Delta_{KK'}$. (d) Spectrum for the case of both finite spin-orbit coupling and KK' -mixing. The energies Δ_{SO} and $\Delta_{KK'}$ manifest in a splitting of the zero-field states with spacing $\Delta = \sqrt{\Delta_{SO}^2 + \Delta_{KK'}^2}$ and as avoided crossings at finite fields.

3.3 Quantum dot spectroscopy

In the case of electronic spectroscopy a bias voltage V_{sd} is applied between the source and drain electrode, which are both coupled to the quantum dot via tunnel barriers. Additionally, a gate voltage can be applied to change the electro-chemical potential of the QD electrons. The response of the conductance to the bias and gate voltage allows us to deduce information about the quantum states of the QD. In such mesoscopic systems also external parameters such as, e.g., temperature and magnetic field are well controllable.

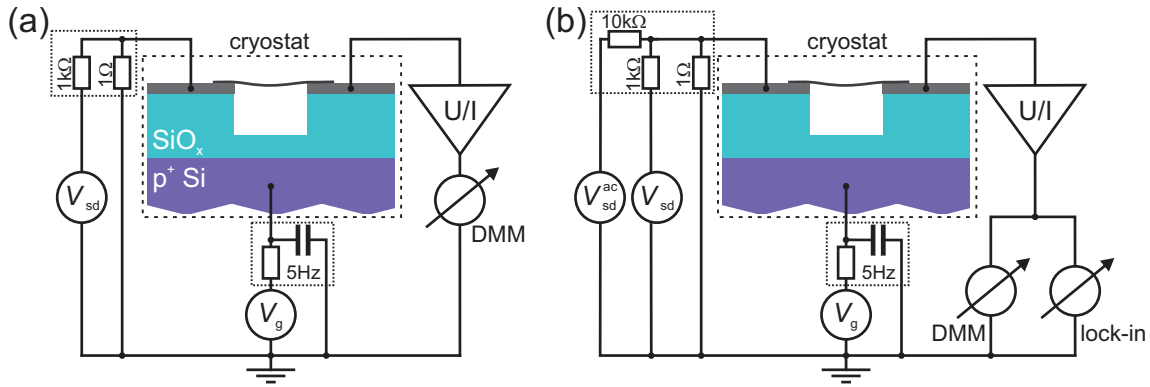


Figure 3.9: (a) Schematics of a DC measurement setup. The bias voltage V_{sd} is reduced by a voltage divider (upper dotted box) and applied to the source contact. The current is detected at the drain contact with a current-to-voltage amplifier and the resulting voltage is read out with a digital multimeter (DMM). Furthermore, a gate voltage V_g is applied to the highly doped silicon substrate via a 5Hz lowpass filter (lower dotted box). (b) Sketch of an AC measurement setup with an ac-voltage superimposed on a dc-voltage, $V_{sd}^{tot} = V_{sd} + V_{sd}^{ac}$. They are combined in a voltage divider (upper dotted box) where the constant ac-voltage is divided by a factor 10^4 and the dc-voltage is divided by 10^3 . At the drain contact the composed dc- and ac-current is amplified and measured with a multimeter and a lock-in amplifier, respectively.

Typical measurement setups are sketched in Fig. 3.9 showing both methods used in this work. For pure dc measurement, depicted in Fig. 3.9(a), a bias voltage is applied to the source contact via a voltage divider $1/1000$, while the current is measured at the drain contact using a current-to-voltage amplifier (with, e.g., $U/I = 10^9 \text{ V/A}$). A gate voltage V_g is applied to the highly doped silicon substrate capacitively coupled to the quantum dot. To reduce ac noise a 5Hz lowpass filter is installed at room temperature directly on the cryostat. This method is mainly used in highly resistive samples with very low currents to allow high integration times in the amplifier.

However, if the sample is more transparent the differential conductance in dependence on the dc-bias voltage can be measured directly with an ac-setup as shown in Fig. 3.9(b). Here a dc-voltage from a voltage source and an ac-voltage with constant amplitude (typically $V_{sd}^{ac} = 5 \mu\text{V}$) and frequency (typically $f \simeq 130 \text{ Hz}$) from a lock-in are combined in a voltage divider and applied to the source contact as bias voltage $V_{sd}^{tot} = V_{sd} + V_{sd}^{ac}$. The current now has a dc- and ac-component which are both amplified and readout by a digital multimeter (DMM) and a lock-in amplifier, respectively.

In a typical characterization measurement the differential conductance is measured in dependence of gate and dc-bias voltage $dI/dV_{sd}(V_g, V_{sd})$. For the charge occupation N the electro-chemical potential of the quantum dot $\mu(N)$ is defined as the energy difference to the adjacent charge occupation $N + 1$, hence

$$\mu(N) = E(N + 1) - E(N). \quad (3.14)$$

Transport through the QD is then only possible if one electro-chemical potential level lies within the "bias window", i.e. between the electro-chemical potential of source (μ_S) and drain (μ_D) electrode: $\mu_S \geq \mu \geq \mu_D$ with $-|e|V_{sd} = \mu_S - \mu_D$. In the zero-bias case ($V_{sd} = 0$) the alignment of the QD level with the source or drain potential can be achieved by tuning the gate voltage to shift the ladder of states with respect to the lead potential. If one varies also the bias voltage one can define a resonance condition of the QD level with at least one lead potential forming the edges of diamonds in the $V_g - V_{sd}$ -plane.

In Fig. 3.10(a) a so-called *Coulomb diamond* (CD) is sketched with resonance lines framing diamond shaped areas of fixed charge number N on the QD. The slopes λ_1 and λ_2 are determined by the gate, source and drain capacitances. The gate conversion factor $\alpha = \Delta E / \Delta V_g$, which connects the energetic difference with a change in the gate voltage, is given by the ratio $\alpha = C_g / C_\Sigma$, which can be also expressed by the slopes of the Coulomb diamond (as sketched in Fig. 3.10(a)): $\alpha = (|1/\lambda_1| + |1/\lambda_2|)^{-1}$ [Glazman and Shekhter, 1989]. Note, that this gate conversion factor depends in general on the number of charges on the quantum dot. In Fig. 3.10(a) the exemplary additional resonance line ending in the CD with charge N corresponds to an excited state of the charge state N , where an additional excited level enters the bias window. This extra channel leads to a step in $I(V_{sd})$. In the derivative $dI/dV_{sd}(V_{sd})$ this step appears as a line in the single electron tunneling (SET) region parallel to one edge of the CD.

Figure 3.10(b) depicts the different situations in the bias vs. gate voltage plane marked in (a) with (I – IV). The point (I) defines the charge degeneracy point, where the equation $\mu_S = \mu = \mu_D$ holds, i.e. the QD level is in resonance with source and drain potential. This resonance condition can be lifted by applying a gate

voltage leading to Coulomb blockade in (II) where all QD levels are either occupied or energetically not accessible. In this configuration the number of charges N on the QD is well defined. Providing energy by a bias voltage V_{sd} between source and drain electrode lifts the blockade at a certain point and single electron tunneling (SET) is possible again (III). If additionally an excited level lies within the bias window, another conductance channel is provided, and the current shows a step leading to a line in $dI/dV_{sd}(V_g, V_{sd})$ parallel to a diamond edge (IV). Note that the number of charges on the quantum dot still can only vary by one electron which tunnels either through the ground state or through the excited state. Both states can not be occupied simultaneously, since the additional charging energy is not provided.

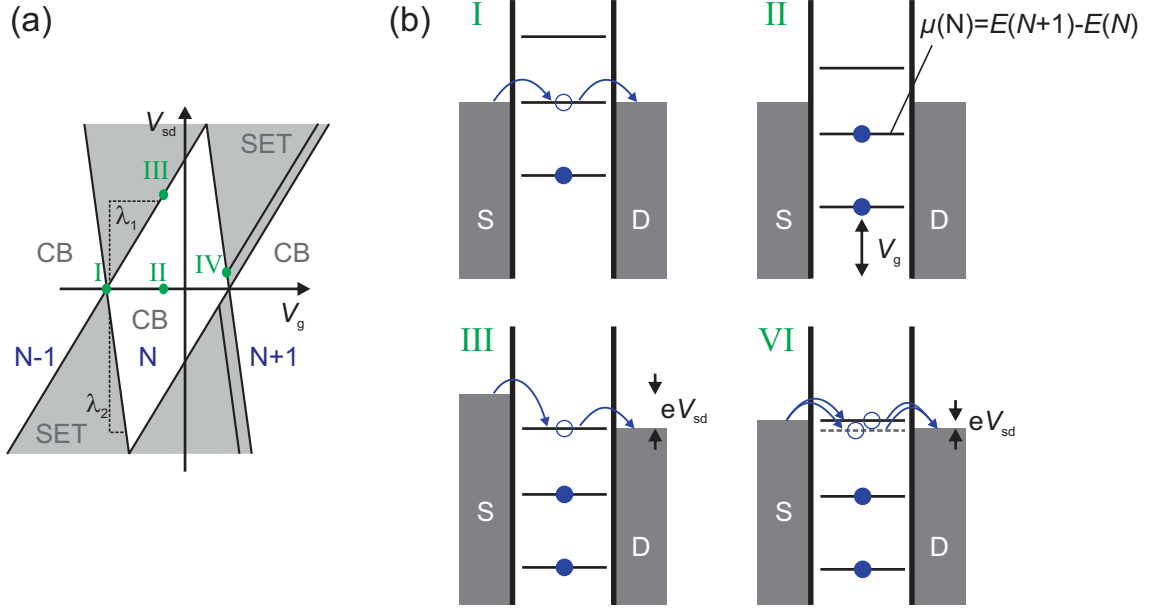


Figure 3.10: (a) Schematic of a measurement $dI/dV_{sd}(V_g, V_{sd})$ in the Coulomb blockade regime. The diamond-shaped regions around $V_{sd} = 0$ where current is blocked by the Coulomb blockade (CB) are usually called *Coulomb diamonds* (CD). The slopes λ_1, λ_2 are determined by the capacitances C_g, C_S, C_D, C_Σ and also yield the gate conversion factor α (see text). (b) Energy diagrams for different situations marked in (a). For linear response (I), i.e. $V_{sd} = 0$, the resonance condition is fulfilled for a QD aligned to the Fermi level of source (S) and drain (D) contact. This is the so-called degeneracy point of two adjacent charging states $N - 1, N$. Changing the electro-chemical potential by a finite gate voltage drives the system out of resonance (II) leading to Coulomb blockade with a fixed number N of electrons on the dot. By applying a finite bias voltage (III) the blockade can be lifted if the QD level lies within the bias window. If additionally excited levels lie in the bias window (IV) this additional channel leads to a step in $I(V_{sd})$. In the derivative $dI/dV_{sd}(V_{sd})$ this steps appears as a line in the SET region parallel to the CD edge.

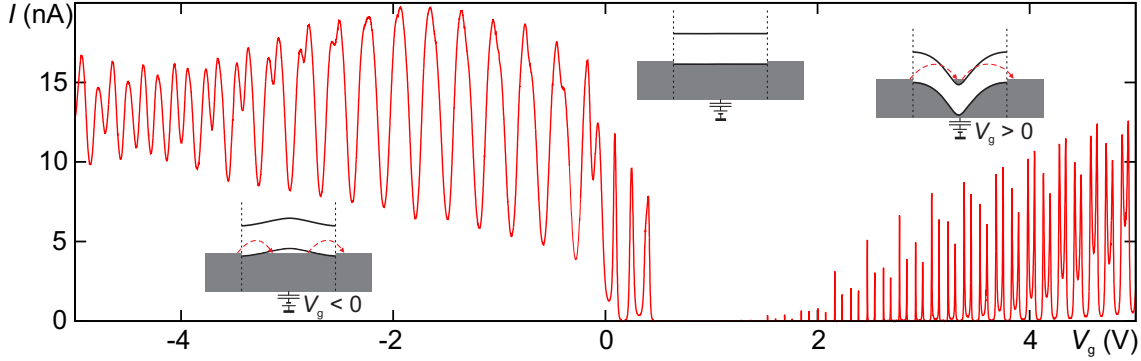


Figure 3.11: Measured current as function of gate voltage V_g , for $V_{sd} = 0.2$ mV and $T = 300$ mK. For $V_g < 0$ the contacts are very transparent leading to Fabry-Pérot like conductance. In the band gap the current is suppressed and for electron conduction at $V_g > 0$ the QD is weakly coupled to the leads by broad tunnel barriers resulting in sharp Coulomb oscillations and Coulomb blockade in between. The insets show a sketch of the band structure at the given gate position, which explains the difference in the tunnel rates for electrons and holes caused by different tunnel barrier widths. *Cool down 1.*³

In our experiment the formation of a quantum dot in an originally one-dimensional CNT is achieved by attaching metal contacts as described in Chapter 2. On the electron conduction side p-n-junctions are formed within the CNT by band deformations, as schematically depicted in the inset in Fig. 3.11 for $V_g > 0$. For negative gate voltages, on the hole conduction side, there seems to be a small Schottky barrier at the metal-nanotube interface, which leads to a transparent, highly conductive system. The metal contacts tend to dope the CNT slightly positive, aligning the Fermi energy close to the valence band.

In a first characterization measurement the current is traced as a function of the gate voltage applied to the highly doped silicon substrate as shown in Fig. 3.11. We can see different coupling regimes which can be explained by the doping in combination with a deformation of the band structure by the applied gate voltage. While on the hole conduction side the band is shifted upwards by the negative gate voltage which leads to very narrow tunnel barriers and thus to highly transparent contacts resulting in Fabry-Pérot features [Liang et al., 2001], on the electron conduction side these tunnel barriers are very broad and the QD is strongly de-coupled from the leads. In the latter case the Coulomb charging energy E_C is the dominant energy, leading to Coulomb blockade at sufficiently low temperature $k_B T \ll E_C = e^2/2C_\Sigma$.

³All the transport measurements have been done on one CNT sample, but in three different cool-downs, which is declared for each plotted measurement within this thesis. Details on the exact measurement setups are given in the Appendix B.

Coulomb oscillation peaks occur at the point of resonance between QD level and the lead potentials – as expected from the schematics in (I) in Fig. 3.10(b). At higher electron numbers N_{el} the gate voltage narrows the barriers leading to an increase of the tunnel rate. In addition this gives rise to co-tunneling effects which are proportional to higher orders of the tunnel coupling. The enhanced current in every second Coulomb valley stems from the Kondo effect inducing a zero-bias peak for odd electron occupation numbers.

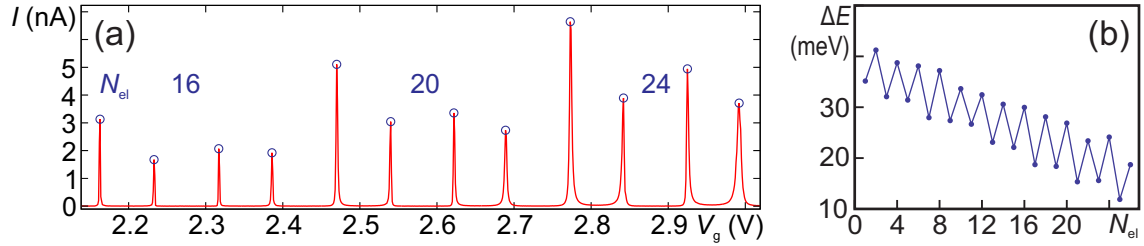


Figure 3.12: (a) Detail of the measurement of Fig. 3.11 at few electrons. A clear fourfold pattern in the Coulomb oscillation height can be observed. The bias voltage is $V_{\text{sd}} = 0.2 \text{ mV}$, the temperature is $T = 300 \text{ mK}$. (b) Peak distance in the gate trace, converted into an energy spacing ΔE using the gate conversion factor $\alpha(N_{\text{el}})$. It shows the charging state dependent addition energy $\Delta E = E_C + \Delta\epsilon$ with a twofold alternation on top of an overall linear decrease. *Cool down 1.*

A zoom into the first Coulomb oscillations in Fig. 3.12(a) reveals a CNT specific fourfold periodicity in the Coulomb oscillation height. This is caused by the each twofold spin and valley degeneracy; each "orbital shell" can be filled by four electrons.

The peak positions in the Coulomb blockade dominated electron conduction region are extracted (see blue circles in Fig. 3.12(a)) yielding the gate distance $\Delta V_g(N_{\text{el}})$ as function of the electron number N_{el} . This can be converted into an addition energy $\Delta E(N_{\text{el}}) = \alpha(N_{\text{el}}) \cdot \Delta V_g(N_{\text{el}})$ as described above. Here the gate conversion factor $\alpha = C_g/C_\Sigma$ has been determined for $0 < N_{\text{el}} < 6$ and for $24 < N_{\text{el}} < 26$. Interpolation of α for different number of electrons on the QD shows a linear dependence with $\alpha(N_{\text{el}} + 1) - \alpha(N_{\text{el}}) \simeq 0.01$ over the covered range with $\alpha(N_{\text{el}} = 1) = 0.46$.

In Fig. 3.12(b) the resulting addition energy ΔE is plotted versus the electron number N_{el} . It reveals a twofold pattern of alternating addition energies on top of a linear decrease. Each second electron charging the quantum dot requires a single electron energy $\Delta\epsilon$ in addition to the classical charging energy E_C . The lack of a fourfold periodicity can be attributed to a broken $SU(4)$ degeneracy as will be discussed in detail in the sections 5.1 and 5.2.

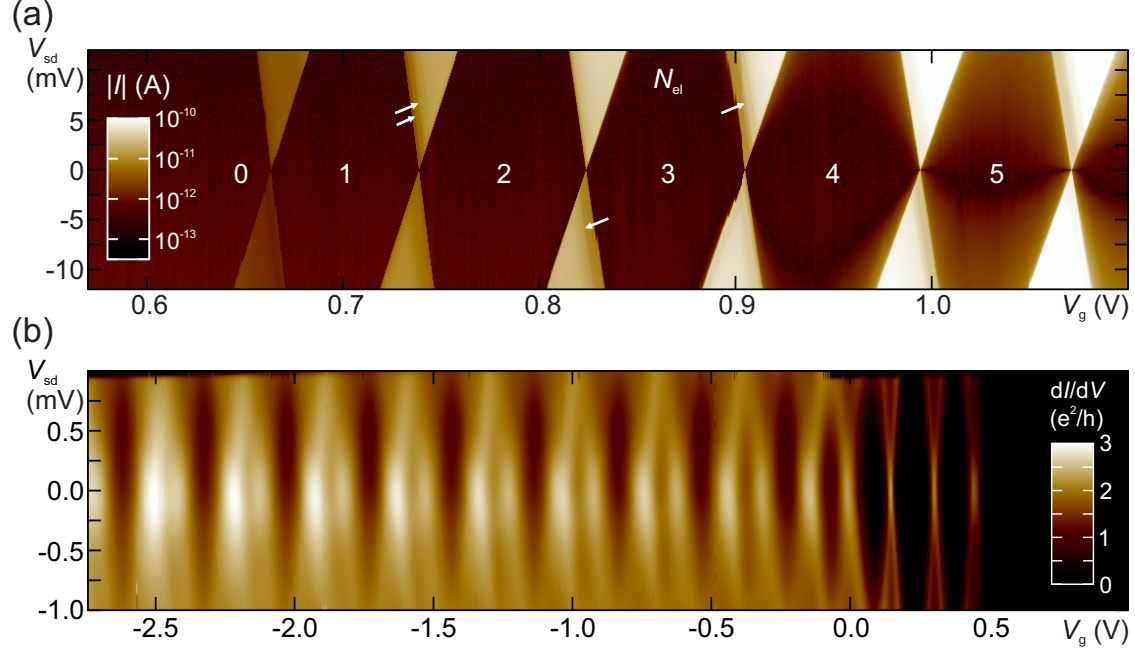


Figure 3.13: (a) Current $|I|$ as function of gate voltage V_g and bias voltage V_{sd} . Regular Coulomb diamonds are observed down to the zero charging state in the band gap. Steps within the single electron tunneling areas (see white arrows) are due to excited electronic states. *Cool down 2.* (b) Differential conductance as function of gate and bias voltage on the hole conduction side. The transition from a Coulomb blockade dominated regime near the band gap into Fabry-Pérot like structures for lower gate voltages is caused by an increase of the tunnel coupling. *Cool down 1.*

The stability diagram of the quantum dot is obtained by measuring the current as a function of both gate and bias voltage $I(V_g, V_{sd})$. On the electron conduction side extremely clear and sharp Coulomb diamonds can be seen down to the charge neutrality in the band gap (Fig. 3.13(a)), meaning that we have access even to the very first electron on the quantum dot in high quality. The absence of further Coulomb oscillations for lower gate voltages has been affirmed by measuring the gate dependence of the current across the band gap at high bias voltages $V_{sd} = 100$ mV. This implies that the number of electrons on the QD at $V_g = 0.7$ V in Fig. 3.13(a) has the absolute value $N_{el} = 1$, and the number of charges at any other gate voltage can be deduced. Steps in the current occur within the single electron tunneling (SET) areas (see white arrows), where excited electronic states provide an additional channel for tunneling through the QD. These steps in the current are peaks in the differential conductance measurements. It can be shown that the excited states of the N -electron system are parallel to the CD edges, and they end in the Coulomb

diamond with the electron number N (compare with Fig. 3.10). On the highly transparent hole conduction side, as shown in Fig. 3.13(b), Coulomb blockade soon evolves into a Fabry-Pérot like conductance pattern. The differential conductance reaches values about $dI/dV_{sd} \simeq 3e^2/h$, slightly below the theoretical value of four conductance quanta, which can be attributed to a small asymmetry in the source and drain coupling rates $\Gamma_{S,D}$.

Chapter 4

The Kondo effect in quantum dots

The Kondo effect has been first proposed by Jun Kondo in 1964, describing the abnormal temperature dependence of a metallic bulk conductor with magnetic impurities using third-order perturbation theory [Kondo, 1964]. Due to the interaction between the localized magnetic moments of the impurities and the spins of the itinerant conduction band electrons the resistance diverges for temperatures approaching zero. This effect becomes dominant below a characteristic temperature, the so-called Kondo temperature T_K . However, the divergence in Jun Kondo's explanation is unphysical. The so-called Anderson model could first give a physical description for temperatures below T_K [Anderson, 1961], and finally Wilson's numerical renormalization method could fully explain this phenomenon by avoiding the restrictions of a perturbative approach [Wilson, 1975].

Theoretically predicted by [Ng and Lee, 1988], [Glazman and Raikh, 1988], [Meir et al., 1993], [Wingreen and Meir, 1994], the Kondo effect in quantum dots has finally been demonstrated experimentally by [Cronenwett et al., 1998], [Goldhaber-Gordon et al., 1998]. In such mesoscopic systems the free metal electrons correspond to the lead electrons, while the localized spin on the QD forms the analogon to the ferromagnetic impurity in the bulk metal. Such systems are highly controllable and allows the experimentalist to adjust the Kondo temperature by gate voltages. Furthermore, due to the access to the precise charging state, a very accurate study of this effect becomes possible, looking at a single unpaired spin instead of an huge ensemble in bulk systems. Below the characteristic temperature T_K , a sharp resonance is formed within the QD at the energy of the Fermi level of the leads due to the singlet formation between a localized spin on the quantum dot with odd charge occupation and the spins of the lead electrons. This is depicted in Fig. 4.1(a) and leads to an enhanced conductance in Coulomb blockade at zero bias voltage (instead of a diverging resistance in bulk materials). The resonance width is proportional to the Kondo temperature and typically much narrower than the tunnel rate induced level

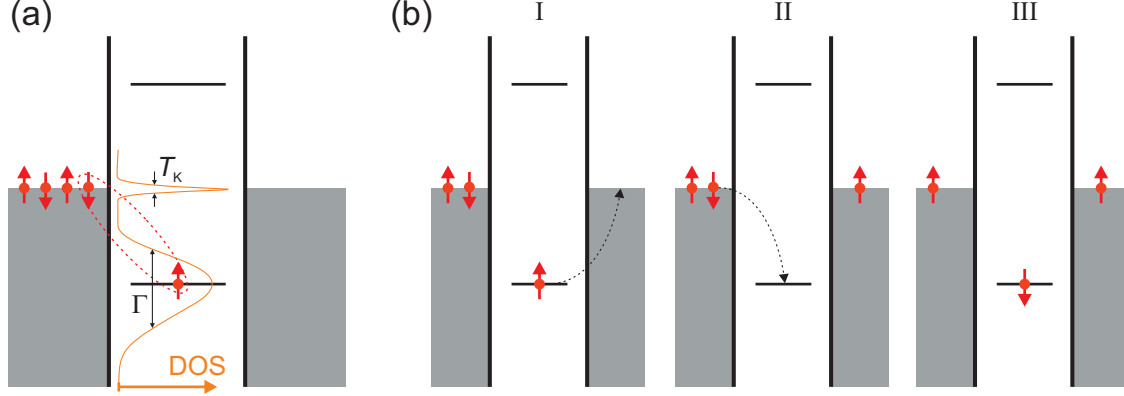


Figure 4.1: (a) The formation of a spin singlet between a localized electron on the QD and an electron on a lead induces a sharp resonance in the QD at the Fermi level of source and drain electrode. While the width of the QD levels are proportional to the total tunnel rate to the leads Γ , this Kondo resonance is proportional to the Kondo temperature T_K . (b) In a co-tunneling picture, the Kondo-effect can be illustrated by a second-order process including a spin-flip of the QD electron.

broadening Γ . Using a co-tunneling picture in Fig. 4.1(b) the Kondo effect can be visualized as a higher-order process where the electron from an unpaired spin state (I) first tunnels off the dot leading to a virtual intermediate state (II). Afterwards the quantum dot level gets occupied by an electron with opposite spin (III). While being a simplification, this correctly implies that a necessary condition for a Kondo resonance is a local state degeneracy, which is in zero magnetic field typically but not necessarily provided by the spin-1/2-degeneracy of a quantum dot level.

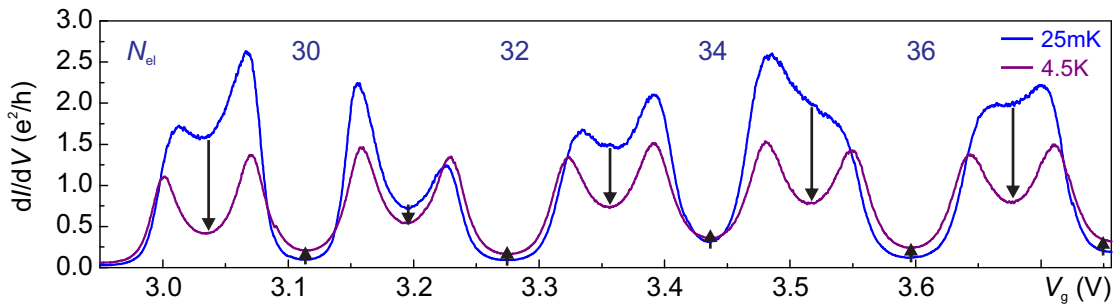


Figure 4.2: The differential conductance $dI/dV_{sd}(V_g)$ in the Kondo regime (here at $28 \leq N_{el} \leq 38$) shows opposite temperature behavior of even and odd Coulomb blockade "valleys". While the conductance increases in even valleys for higher temperature the conductance in the odd valleys decreases. *Cool down 2.*

The Kondo effect in QDs leads to a distinct increase of the conductance for an odd electron charge state where an unpaired spin is present in the QD at temperatures below T_K . The gate trace in Fig. 4.2 nicely shows the weakened Kondo correlations at higher temperatures as the conductance for odd N_{el} decreases while it increases in even valleys (indicated by arrows).

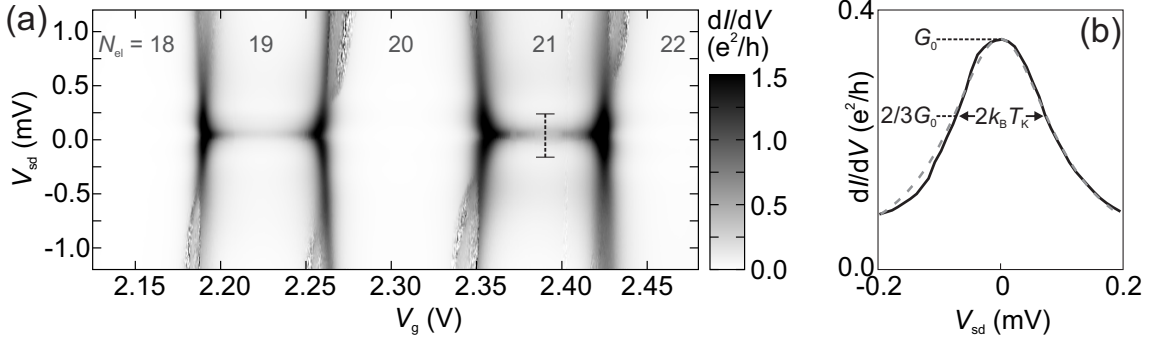


Figure 4.3: (a) Stability diagram $dI/dV_{\text{sd}}(V_g, V_{\text{sd}})$ in the intermediate coupling regime ($18 \leq N_{\text{el}} \leq 22$) showing sharp zero-bias Kondo ridges. The temperature is $T \simeq 80 \text{ mK} \simeq T_K/15$. (b) A bias voltage trace $dI/dV_{\text{sd}}(V_{\text{sd}})$ taken at a fixed gate voltage in the center of the Coulomb diamond with $N_{\text{el}} = 21$ in the low-bias regime –marked by the dashed line in (a)– shows a sharp Kondo peak. The width at $2/3 \cdot G_0$ corresponds to the Kondo temperature $T_K = 0.86 \text{ K}$. A Lorentzian curve (gray dashed line) is plotted on top to indicate the universal line shape. *Cool down 2.*

In the stability diagram the spin-1/2 Kondo effect manifests as a ridge at $V_{\text{sd}} = 0$ across the Coulomb diamond with odd electron numbers N_{el} . In Fig. 4.3(a) such a measurement is shown, covering the electron numbers $18 \leq N_{\text{el}} \leq 22$. To avoid high currents the bias voltage is restricted to a small range $-1.2 \text{ mV} < V_{\text{sd}} < 1.2 \text{ mV}$ making the diamond shaped Coulomb blockade regions hardly visible. The noisy regions around the source and drain lines of the Coulomb diamond are caused by mechanical instabilities as explained in Sec. 6.2. The striking features however are the sharp ridges at $V_{\text{sd}} = 0$ for $N_{\text{el}} = 19, 21$. Especially in the line trace $dI/dV_{\text{sd}}(V_{\text{sd}})$ in the center of the Coulomb diamond $N_{\text{el}} = 21$ one can see the Kondo effect induced zero-bias anomaly in the low-bias regime (see Fig. 4.3(b)). The width of the central Kondo peak is directly proportional to the characteristic Kondo temperature T_K . The relation is given by

$$dI/dV \Big|_{V_{\text{sd}}=k_B T_K/e} = 2/3 \cdot dI/dV \Big|_{V_{\text{sd}}=0}, \quad (4.1)$$

meaning that the width of the central peak at $2/3 \cdot G(V_{\text{sd}} = 0)$ is equal to $2 k_B T_K$ as sketched in Fig. 4.3(b) [Kretinin et al., 2012].

Besides the $SU(2)$ spin-1/2-Kondo in CNTs additionally an $SU(2)$ orbital Kondo effect can appear where the required degenerate state is provided by the KK' valley instead of the spin degeneracy. As shown in Fig. 4.4 the transitions involving spin-flip processes (a) can be adapted to an orbital quantum number flip in (b). If both degeneracies are present there is an $SU(4)$ symmetry leading to a strongly enhanced $SU(4)$ Kondo effect (see Fig. 4.4(c)).

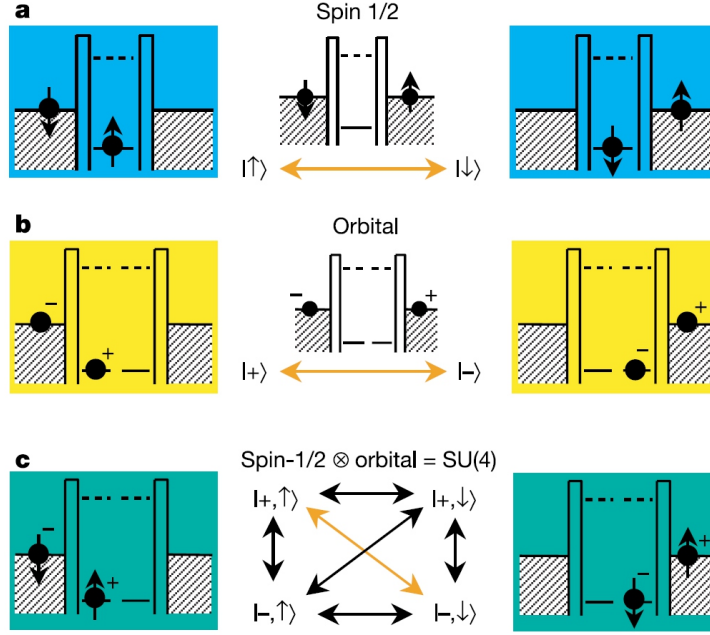


Figure 4.4: (a) Higher order tunnel processes for common spin-1/2-Kondo effect involving a spin-flip between initial and final state. (b) In the case of orbital Kondo effect the orbital quantum number corresponding to the KK' valley degeneracy in CNTs is flipped. (c) The presence of both spin and valley (fourfold) degeneracy leads to an entanglement of spin and orbital states causing an enhanced $SU(4)$ Kondo effect. Reproduced from [Jarillo-Herrero et al., 2005b].

Chapter 5

Electronic spectroscopy of ultra-clean carbon nanotube quantum dots

A motivation for quantum transport measurements on carbon nanotubes is the initial one-dimensionality of the electronic system, which provides a model system for physical effects like Luttinger liquid [Bockrath et al., 1999], 1D Wigner crystal [Deshpande and Bockrath, 2008] or Mott insulator [Deshpande et al., 2009] formation. Further restriction to a zero dimensional system, a quantum dot (QD), can be easily achieved by means of micro- and nano-fabrication. Due to the inherent strong electronic confinement in radial direction, a longitudinal confinement in the range of hundreds of nanometers already induces confinement energies $\Delta\epsilon$ of some tens of meV. These can easily be resolved in transport spectroscopy measurements at cryogenic temperatures, where $k_B T \ll \Delta\epsilon$. Here, CNTs establish a highly versatile quantum system, permitting tuning from strongly decoupled, Coulomb blockade dominated transport via an intermediate regime with higher-order effects as, e.g., the Kondo effect up to Fabry-Pérot like conductance.

Using a modified device fabrication process which shifts the CNT growth to the very last step keeps the nanotubes as clean as possible. The electronic states display regular shell behavior as expected for electrons trapped in the unperturbed nanotube band structure. This enables us for instance to examine the electronic properties down to the neutral charging state by electronic spectroscopy of the first electron's ground and excited states. Furthermore the resolution of fine structures of Kondo resonances can be used to trace the internal parameters and symmetries.

This fabrication method can serve as basis for further advanced sample structures, such as, e.g., chips combined with integrated antenna structures for plasma en-

hanced Raman measurements. In this case structural properties of an ultra-clean CNT obtained by electronic spectroscopy can be compared with results from the Raman spectrum. Finally, devices with ferromagnetic or superconducting electrode materials may lead to very rich physics studying tunnel magneto-resistance effects, spin-polarized currents, proximity-induced superconductivity, and the interactions of all these phenomena.

5.1 Single particle spectrum in the presence of spin-orbit coupling and KK' -mixing

This section focuses on the first Coulomb oscillation next to the semiconducting band gap on the electron conduction side, i.e. on the charge transition $0 \rightarrow 1$ electron, where electron-electron interaction is absent and the single-particle level spectrum is directly visible in the spectroscopy of ground and excited levels. Due to the weak coupling to the leads the total tunnel rate Γ , corresponding to the state decay rate, is very low which causes very sharp features in the stability diagram. The transport is dominated by single electron tunneling and the broadening of the conductance peaks is temperature induced: $\hbar\Gamma \ll k_B T \ll E_C$. For this reason very low temperatures lead to high spectroscopic resolution. The suspended CNT sample is mounted in a $^3\text{He}/^4\text{He}$ dilution cryostat, where the sample itself is immersed into the diluted phase of the $^3\text{He}/^4\text{He}$ mixture at fixed temperature $T \simeq 30$ mK. This makes a better thermal contact, and in particular mechanical motion is strongly damped by the highly viscous ^3He , preventing electronical instabilities caused by self-excited mechanical motion [Schmid et al., 2012]. A rotatable sample holder allows us to change the orientation of the CNT axis with respect to an in-plane magnetic field, which is generated in a superconducting magnet with a flux density up to 17 T, from perpendicular to parallel.

5.1.1 Angle calibration

In a first angle calibration step the current $I(V_g, \theta)$ is measured for different rotation angles θ of the chip carrier with respect to the fixed finite field $|\vec{B}| = 10$ T at zero bias voltage, as depicted in Fig. 5.1.

A strong modification of the level energies is caused by the parallel component of the field due to a large orbital magnetic moment (large orbital g -factor g_{orb}),¹ which couples to magnetic fields parallel to the CNT axis. Therefore one expects that

¹The orbital magnetic moment is due to a circular motion of the electron around the nanotube, clockwise in K and counter-clockwise in the K' state. Its value depends on the CNT diameter.

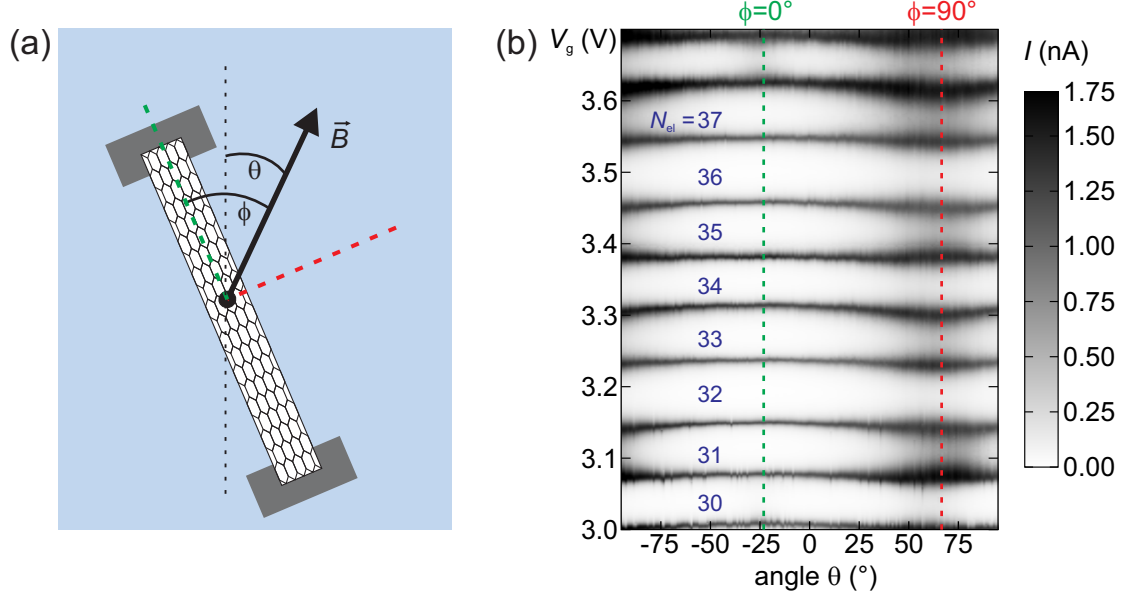


Figure 5.1: (a) Sketch of the in-plane magnetic field orientation relative to the chip carrier (θ), and with respect to the nanotube axis (ϕ). (b) Current as function of the gate voltage V_g at different rotation angles θ of the chip carrier with respect to the external magnetic field. The extracted perpendicular ($\phi = 90^\circ$, red dashed line) and parallel ($\phi = 0^\circ$, green dashed line) field orientation with respect to the CNT axis are indicated. The applied bias voltage is zero at a fixed magnetic field magnitude $|\vec{B}| = 10$ T. *Cool down 3.*

the angle dependence of the energy spectrum is strongest around the perpendicular alignment, where the change in the parallel magnetic field component is maximum. This is exactly what one observes in Fig. 5.1(b), where around $\phi = 90^\circ$ (red dashed line) the Coulomb oscillation width and position shows the maximum dependence on angle deviations. In contrast, around $\phi = 0^\circ$ (green dashed line in Fig. 5.1(b)) the trace $I(V_g)$ is hardly affected by small misalignments to $\phi = 0^\circ$.

This measurement is used as reference for the following experiments, where a parallel magnetic field ($\phi = 0^\circ$) is denoted by B_{\parallel} , and magnetic fields in perpendicular orientation to the CNT axis ($\phi = 90^\circ$) are expressed by B_{\perp} .

5.1.2 Parallel magnetic field

Instead of a direct ac measurement of the differential conductance a dc-setup is used (see Fig. 3.9(a) in Sec. 3.3) with a high amplification and a long integration time to achieve detection of low signals.

In Fig. 5.2 the current is measured versus gate and bias voltage, followed by low-pass

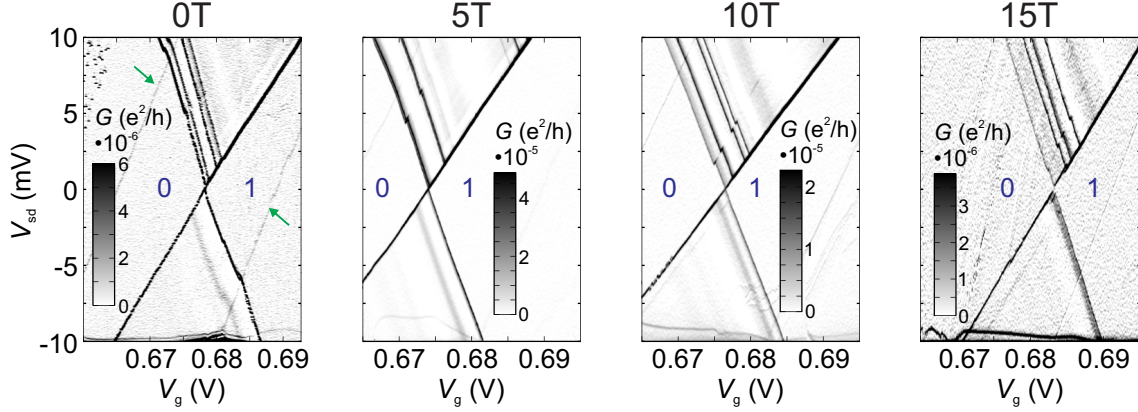


Figure 5.2: Stability diagrams of the first Coulomb oscillation ($0 < N_{el} < 1$) at different magnetic fields parallel to the nanotube axis. The plotted differential conductance $G(V_g, V_{sd})$ is the numerical derivative of the measured dc-current $\partial I(V_g, V_{sd})/\partial V_{sd}$. The number of charges on the quantum dot are indicated by the blue numbers in the Coulomb blockade regions. The faint extra lines, marked with the green arrows, can not be attributed to noise, rather this could be an effect of an additional quantum dot weakly coupled to the leads. *Cool down 3.*

filtering and numerical derivation with respect to the bias voltage. This yields the differential conductance $dI/dV_{sd}(V_g, V_{sd}) \equiv G(V_g, V_{sd})$. Aside an overall shift of the diamond with respect to the gate voltage V_g the excited states show a clear energy dependence on the parallel field B_{\parallel} .

As depicted in Fig. 5.3(a) the gate voltage is now set to a constant value "left" of the Coulomb resonance and the bias voltage is swept, intersecting the ground (1) and excited states (2, 3, 4), for different magnetic field values. In order to obtain the energy spacing δE between the ground and excited states one has to scale the distance δV_{sd} in the measured bias trace by a geometric factor deduced from the sketch in Fig. 5.3(b). This scaling is required since the energy of the excited states can be read off from the bias value where the excited line crosses the edge of the diamond (see e.g. [Cobden and Nygard, 2002]). The scaling is given by

$$\delta E = e \delta V_{sd} \cdot \frac{\sin(\alpha) \cos(\beta)}{\sin(\pi - \alpha - \beta)}, \quad (5.1)$$

where the angles α and β as sketched in Fig. 5.3(b) are extracted from the experiment. They are given by the sample specific values of source, drain, and gate capacitances C_S, C_D, C_g , as defined in Fig. 3.6(a) in Section 3.2. For the $0 < N_{el} < 1$ transition we obtain $\delta E = 0.33 \cdot e \delta V_{sd}$.

In Fig. 5.3(c) at zero field one can identify the four conductance maxima (1, 2, 3, 4)

with the lower and upper pair corresponding to first and second shell (longitudinal mode of the CNT), consisting each of a quadruplet of states. These quadruplets are for $B = 0$ paired in so-called Kramers doublets, with an energy spacing Δ between the doublets. In finite field these doublets split up into two peaks moving apart until an anti-crossing occurs at $B_{\parallel} \simeq 0.3 \text{ T}$ (*). For higher magnetic field the levels behave linearly with individual characteristic slopes.

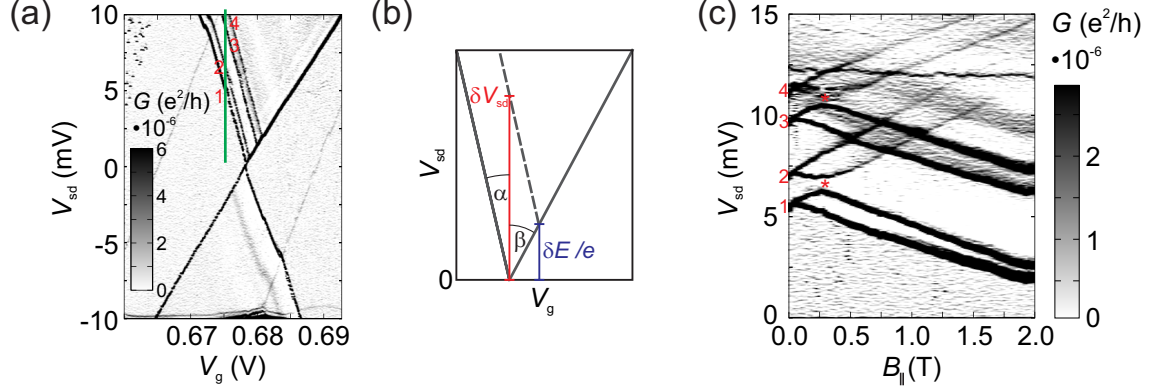


Figure 5.3: (a) Stability diagram of the first Coulomb oscillation at $B = 0$. The sketched bias trace (green line) intersects the ground (1) and the excited state lines (2, 3, 4) of the first electron. (b) Sketch of a Coulomb oscillation for positive bias voltage with one excited line (dashed). The relevant entities to calculate the energy difference δE from the spacing δV_{sd} in the measured bias trace are depicted. (c) Magnetic field dependence of the bias trace $G(V_{sd})$ through the first diamond (as indicated by the green line in (a)) in parallel field orientation with respect to the nanotube axis. Anti-crossings at finite B_{\parallel} are indicated (*). *Cool down 3.*

5.1.3 Linear low field range

This section is based on evaluations performed by Dr. M. Marganska.

In order to evaluate the low field range of one longitudinal mode it is sufficient to start with a linearized Hamiltonian in valley and spin basis $\{|K \uparrow\rangle, |K \downarrow\rangle, |K' \uparrow\rangle, |K' \downarrow\rangle\}$, which is given by

$$\begin{aligned}
 H = & \frac{1}{2} g_s \mu_B B \begin{pmatrix} 1 & 0 & 0 & 0 \\ 0 & -1 & 0 & 0 \\ 0 & 0 & 1 & 0 \\ 0 & 0 & 0 & -1 \end{pmatrix} + \frac{1}{2} \begin{pmatrix} \Delta_{SO} & 0 & \Delta_{KK'} & 0 \\ 0 & -\Delta_{SO} & 0 & \Delta_{KK'} \\ \Delta_{KK'} & 0 & -\Delta_{SO} & 0 \\ 0 & \Delta_{KK'} & 0 & \Delta_{SO} \end{pmatrix} \\
 & + B \begin{pmatrix} \mu_{orb}^p & 0 & 0 & 0 \\ 0 & \mu_{orb}^a & 0 & 0 \\ 0 & 0 & -\mu_{orb}^a & 0 \\ 0 & 0 & 0 & -\mu_{orb}^p \end{pmatrix} + a |B| \begin{pmatrix} 1 & 0 & 0 & 0 \\ 0 & 1 & 0 & 0 \\ 0 & 0 & 1 & 0 \\ 0 & 0 & 0 & 1 \end{pmatrix}. \quad (5.2)
 \end{aligned}$$

The first term takes into account the Zeeman energy, the second one introduces the spin-orbit coupling by the energy Δ_{SO} and the KK' -mixing $\Delta_{KK'}$. The third term considers the orbital magnetic moment which stems from the cylindrical topology of the CNT. The orbital momenta are allowed to be different for the two Kramers doublets: $\mu_{orb}^a = (\mu_{orb}(K \downarrow) - \mu_{orb}(K' \uparrow))/2$ is the orbital moment of the *antiparallel* Kramers doublet while $\mu_{orb}^p = (\mu_{orb}(K \uparrow) - \mu_{orb}(K' \downarrow))/2$ is the orbital moment of the *parallel* Kramers doublet.

For good agreement with the experiment one also has to take into account an "valley asymmetry" term proportional to the norm of the magnetic field $|B|$ weighted by the constant a . The physical origin of this last term in Eq. 5.2 is so far not understood. The energy spacing between different longitudinal momentum states (QD shells) is expressed by Δ_{\parallel} .

The theoretical modeling has been done by Dr. M. Marganska in the group of Prof. Grifoni, yielding the fit parameters for the first and second quantum dot shell in Table 5.1. The fitted energy dispersion is plotted in Fig. 5.4 on top of the conductance measurement as function of the external magnetic field B_{\parallel} and the applied bias voltage V_{sd} . We find a very good quantitative agreement despite the linear approximation of the Hamiltonian in Eq. 5.2.

From the orbital moments $\mu_{orb}^{a/p}$ one can estimate the radius of the CNT with the relation

$$\mu_{orb} \simeq \hbar v_F \frac{\pi R}{\phi_0}.$$

We obtain

$$R \simeq \frac{\phi_0 \mu_{\text{orb}}}{\pi \hbar v_F} \simeq \frac{4.136 \cdot 10^5 \text{ T} \cdot \text{\AA}^2 \cdot 0.81 \text{ meV} \cdot \text{T}^{-1}}{\pi \cdot 5.79 \cdot 10^3 \text{ meV} \cdot \text{\AA}} \simeq 1.8 \text{ nm} ,$$

where ϕ_0 denotes the magnetic flux quantum, and $v_F \simeq 8 \cdot 10^5 \text{ m/s}$ is the Fermi velocity in the CNT. Assuming quantum box boundary conditions the longitudinal quantization energy Δ_{\parallel} can be approximated by

$$\Delta_{\parallel} \simeq \hbar v_F \cdot \Delta k_{\parallel} \simeq \hbar v_F \frac{\pi}{L} .$$

Thus one can make an estimation of the QD extension in the CNT axis direction:

$$L^{\text{theory}} \simeq \frac{\pi \hbar v_F}{\Delta_{\parallel}} = \frac{\pi \cdot 5.79 \cdot 10^3 \text{ meV} \cdot \text{\AA}}{1.4 \text{ meV}} = 1.3 \mu\text{m} .$$

Evaluation and interpretation of the data is still ongoing. One central open question is the origin of the asymmetry term. Since it differs between the two shells and is completely absent at the $1 < N_{\text{el}} < 2$ transition (evaluation not shown), it cannot be due to experimental errors such as, e.g., magnetic field miscalibration, but must be inherent to the nanotube. So far scientific discussions have not brought up any potential mechanism.

In addition, the estimated length of $L^{\text{theory}} = 1.3 \mu\text{m}$ is unlikely a given trench width of $L \simeq 700 \text{ nm}$ and additional depletion zones within the pn-transitions. Here, the model assumption of hard potential walls in longitudinal direction may lead to an overestimation of Δ_{\parallel} . A more realistic description is a smooth distortion of the band structure forming a shallow puddle below the Fermi energy. This puddle is separated from the lead states by broad pn-junctions inducing low tunnel rates. Further the shell spacing Δ_{\parallel} depends on the confinement potential and on the CNT dispersion.

	shell 1	shell 2
μ_{orb}^a	0.89 meV/T	0.77 meV/T
μ_{orb}^p	0.88 meV/T	0.69 meV/T
a	0.17 meV/T	0.05 meV/T
Δ_{SO}	0.48 meV	0.41 meV
$\Delta_{\text{KK}'}$	0.28 meV	0.21 meV
Δ	0.56 meV	0.46 meV
Δ_{\parallel}	1.4 meV	

Table 5.1: Numerical values obtained from fitting the electronic spectroscopy measurement of the excited states of the first electron.

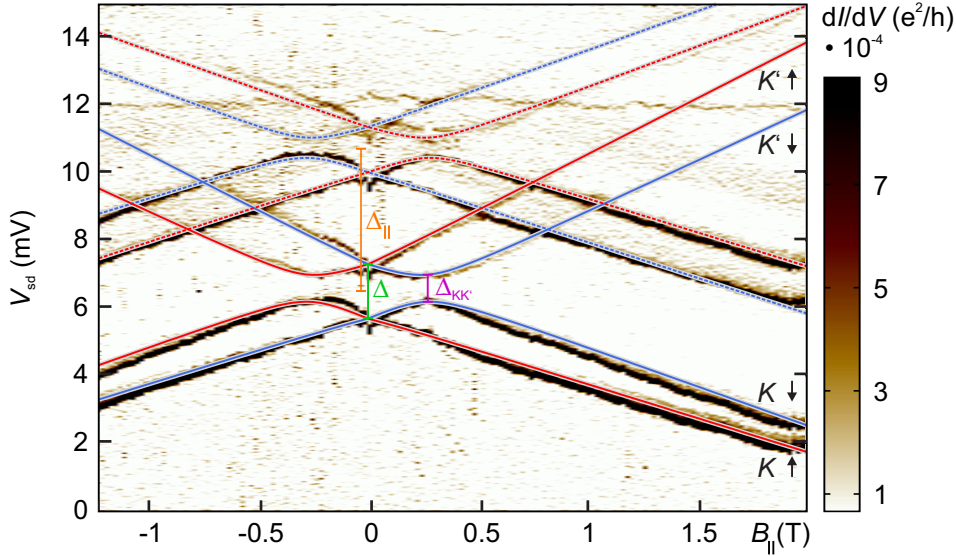


Figure 5.4: The magnetic field dependence of the excited states of the first electron is fitted with the minimal Hamiltonian of Eq. 5.2 including spin-orbit coupling and KK' -mixing, for two shells. The obtained fit parameters are listed in Table 5.1. For the first shell the eigenstates and energies are sketched in with solid lines. Here, $\Delta = \sqrt{\Delta_{\text{SO}}^2 + \Delta_{\text{KK}'}^2}$. The second shell is energetically separated from the first shell by Δ_{\parallel} with slightly differing parameters (dashed lines). Evaluation by Dr. M. Marganska, group Prof. Grifoni. *Cool down 3*.

5.1.4 High field range

The electronic spectroscopy has also been performed on a larger scale up to $B_{\parallel} = 17$ T at lower resolution, as shown in Fig. 5.5. For lower fields we recognize again the splitting of the two Kramers doublets of the first and second shell, where the K' states vanish for increasing field and bias voltage. The discontinuity of the lowest curve is caused by a crossing of the Coulomb resonance through the fixed gate voltage where the bias traces are taken (see in Fig. 5.3(a)). The data evaluation requires to

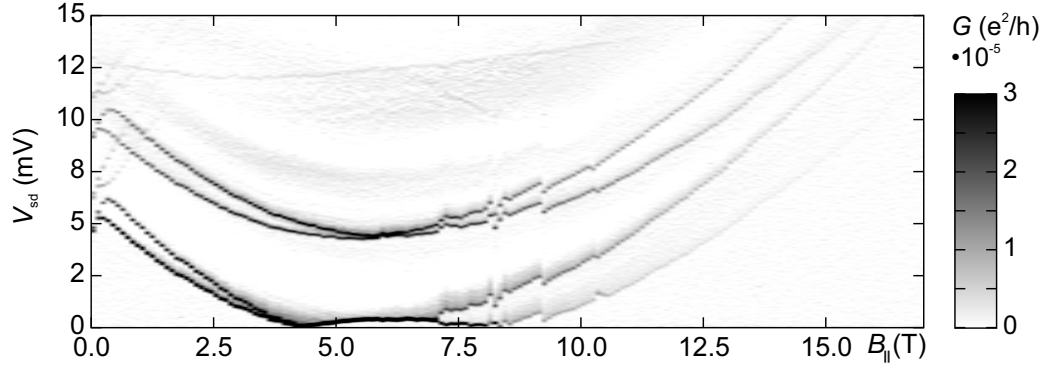


Figure 5.5: Magnetic field dependence of the bias trace $G(V_{sd})$ at $V_g = 0.675$ V through the first diamond in parallel alignment to the nanotube axis in the high field range. Numerically differentiated dc current. *Cool down 3*.

take into account the full CNT dispersion [Izumida et al., 2009], which reads

$$E(\tau, \sigma, \kappa'_{\parallel}, B) = \hbar v_F \sqrt{\left(\tau \Delta k_{\perp} + \sigma \Delta k_{SO} + \frac{\pi R}{\phi_0} B \right)^2 + (\kappa'_{\parallel})^2 + \sigma \mu_B B + \tau \sigma \varepsilon_{SO}}. \quad (5.3)$$

Depending on whether the nanotube is metallic or semiconducting, $\Delta k_{\perp} = \Delta k_{\perp}^c$ (if metallic) or $\Delta k_{\perp} = \frac{\nu}{3R} + \Delta k_{\perp}^c$ (if semiconducting), where $\nu = (m_1 - m_2) \bmod 3$. The axial momentum κ'_{\parallel} results from the longitudinal boundary conditions.

In Fig. 5.6 a first attempt of the fitting of the measured data in the high field range, using the full CNT Hamiltonian in Eq. 5.3, is shown. The discrepancy for $B_{\parallel} > 9$ T is mainly caused by potential jumps due to discrete charging/ discharging events close to the device. The effect of these events is equivalent to a sudden change in the gate voltage V_g , here inducing an overall downwards shift of the resonance lines.

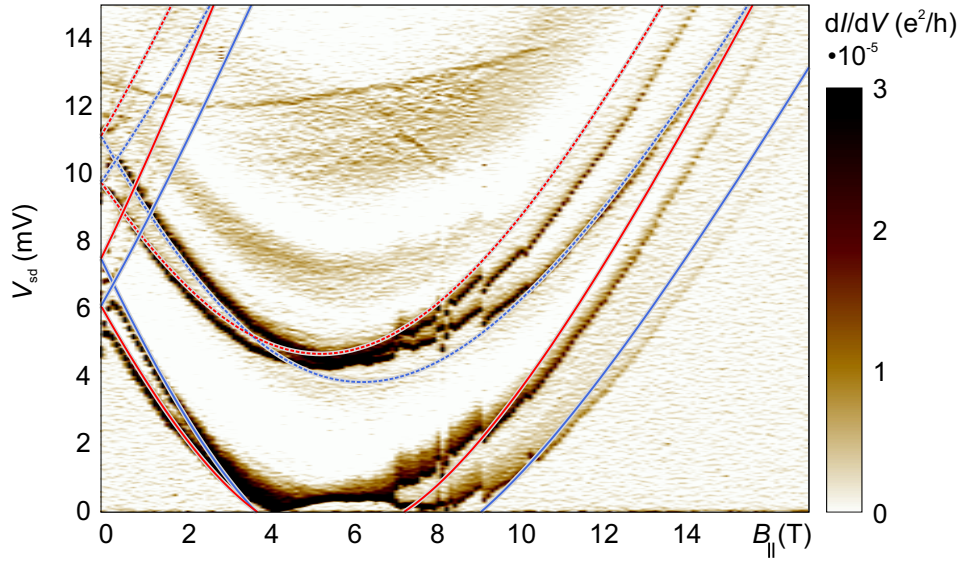


Figure 5.6: Energy dispersion of the first electron excited states, fitted up to high fields ($0 < B_{\parallel} < 17$ T) using the full CNT dispersion given in Eq. 5.3. Here, the valley mixing term $\Delta_{KK'}$ has been omitted. Evaluation by Dr. M. Marganska, group Prof. Grifoni.

5.2 Kondo spectroscopy of CNT quantum dot with finite spin-orbit coupling and KK' -mixing

Towards higher electron numbers the tunnel barriers from QD to source and drain contact decrease, increasing the overall conductance and enhancing higher-order tunneling processes.

All measurements in this section have been conducted with an ac-setup using a lock-in amplifier as depicted in Fig. 3.9(b) of Sec. 3.3. An ac-signal is added to a dc bias voltage V_{sd} and applied to the source electrode of the CNT. The current from the drain contact is amplified at room temperature with a current-to-voltage amplifier, and the dc and ac output is read out with a multimeter and the lock-in amplifier, respectively. A gate voltage V_g is applied to the highly doped silicon substrate acting as global back gate to modify the electro-chemical potential of the quantum dot (QD), allowing us to change the QD charging state N_{el} . A 5 Hz low-pass filter reduces ac noise in the gate voltage.

The data were obtained with the same sample in two cool-downs in different dilution cryostats, both with base temperatures of $T \simeq 30$ mK.

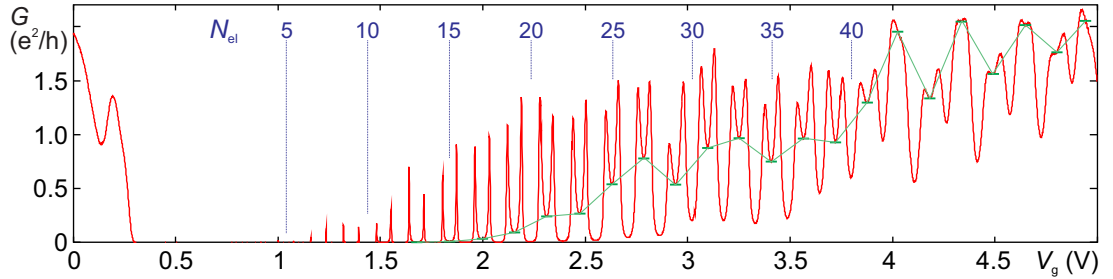


Figure 5.7: Gate dependence of the conductance $G(V_g) \equiv dI/dV_{sd}(V_g)$ at low bias voltage $V_{sd} = 0.2$ mV with denoted charging state N_{el} . It corresponds to the measurement in Fig. 3.11 with focus on the electron conduction side and at lower temperature $T = 30$ mK. The green line indicates the gradually increasing conductance in the Coulomb valleys of odd electron numbers N_{el} for increasing gate voltages. *Cool down 3.*

As already mentioned in Sec. 4, one of the distinctive features of the Kondo effect is a zero-bias peak in the bias trace $G(V_{sd})$ at sufficiently low temperatures T and magnetic fields B . In the gate dependence of the conductance trace $G(V_g)$ at $V_{sd} = 0$ the Kondo effect emerges as an elevated conductance in the valleys with odd electron numbers N_{el} . This we exactly see in our measurement, plotted in Fig. 5.7, where Coulomb blockade at $V_g > 0.6$ V blocks the current in the low charging states, but for higher electron numbers ($N_{el} \gtrsim 17$) the Kondo effect gradually enhances the

conductance in the Coulomb valleys with odd N_{el} . It is illustrated by the green bars and lines, tracing the zero-bias conductance in the odd Coulomb valleys. In the case of equal tunnel barriers causing identical tunnel rates to source and drain contact, the conductance should reach the so-called unitary limit $G = 2e^2/h$ for $SU(2)$ and $G = 4e^2/h$ for $SU(4)$ symmetry, respectively. The values reached in our experiment are slightly above the $SU(2)$ limit for $N_{\text{el}} = 43, 47, 51$, which may be caused by the reduction of the $SU(4)$ limit by asymmetric tunnel rates to the source and drain contact. It could also be a hint for a weakly broken $SU(4)$ symmetry [Fang et al., 2008], [Galpin et al., 2010].

Measuring the bias voltage dependence of the differential conductance $G(V_{\text{sd}})$ at various electron numbers N_{el} and in each case at a fixed gate voltage V_g in the center of the Coulomb blockade valley in the gate trace (Fig. 5.7) yields a strong even-odd electron number periodicity. This can be seen in Fig. 5.8, where the $G(V_{\text{sd}})$ curves are arranged according to the shell filling. In the even valleys (first and third panel) the $G(V_{\text{sd}})$ traces are quite flat except for tiny double peak structures around zero bias voltage. These may be attributed to the superconductivity of the rhenium leads; they vanish at magnetic fields $B > 1$ T. For an odd electron number on the QD (second and fourth panel in Fig. 5.8), however, there are pronounced zero-bias peaks plus broad satellite peaks at finite bias voltages $V_{\text{sd}} = \pm\Delta/e$.

To link the observed Kondo features to transitions within one longitudinal mode of the QD, one has to analyze the symmetry behavior of the CNT Hamiltonian and its eigenstates $|1\rangle, |2\rangle, |3\rangle, |4\rangle$ with the respective eigenenergies $\varepsilon_1, \varepsilon_2, \varepsilon_3, \varepsilon_4$.

5.2.1 Theory of Kondo transitions and selection rules

As discussed in Sec. 5.1, one CNT QD quadruplet, formed by the spin and valley states of one longitudinal mode, is well described by the minimal Hamiltonian given in Eq. 3.12. To understand the unconventional Kondo features observed in the bias dependence of the conductance in the odd Coulomb valleys the effect of the discrete symmetries of the CNT Hamiltonian in zero and finite magnetic field has to be investigated.

In [Schmid et al., 2014] it has been reported that the time-reversal symmetry (TRS) $\hat{\mathcal{T}}$, the particle-hole symmetry (PHS) $\hat{\mathcal{P}}$, and the chiral symmetry (CS) $\hat{\mathcal{C}}$ operators are explicitly given by

$$\begin{aligned}\hat{\mathcal{T}} &= -i\hat{\sigma}_y \otimes \hat{\tau}_z \kappa, \\ \hat{\mathcal{P}} &= \hat{\sigma}_z \otimes (-i\hat{\tau}_y) \kappa, \\ \hat{\mathcal{C}} &= \hat{\mathcal{P}}\hat{\mathcal{T}}^{-1} = \hat{\sigma}_x \otimes \hat{\tau}_x.\end{aligned}\tag{5.4}$$

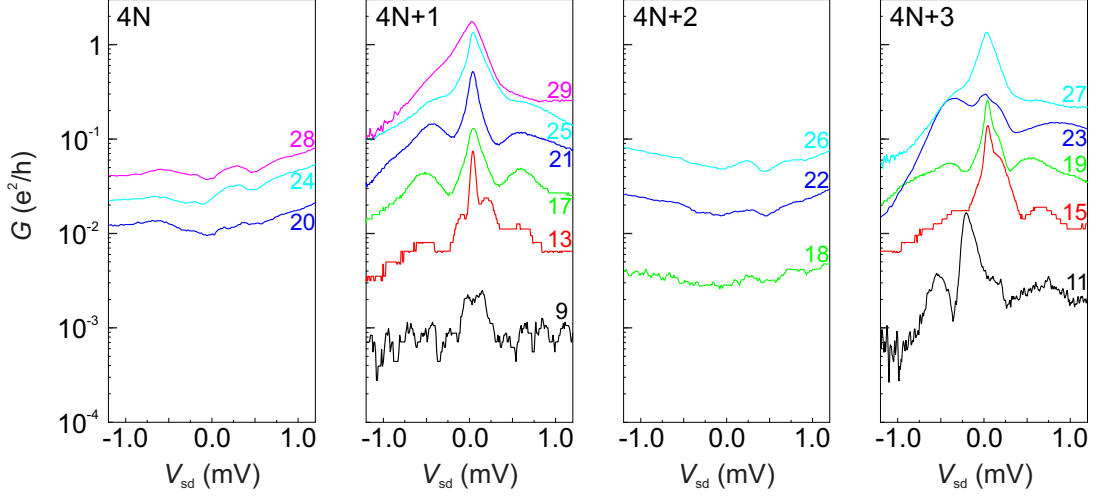


Figure 5.8: Bias trace $G(V_{sd})$ are shown for different Coulomb valleys sorted according to the shell filling state. At odd electron number ($N_{el} = 4N+1$, $N_{el} = 4N+3$) the traces are dominated by Kondo originating zero-bias peaks and finite-bias satellites. *Cool down 2.*

Here the basis is formed by the bonding and anti-bonding combinations of the K , K' states as depicted in Eq. 3.13. The operators $\hat{\sigma}_i$ and $\hat{\tau}_i$ ($i = x, y, z$) act on spin and valley space, respectively, and κ stands for the complex conjugation.

In the following, the minimal Hamiltonian is investigated with respect to these symmetry transformations first in zero and then in finite perpendicular magnetic field.²

The Hamiltonian is identical to Eq. 3.12 but rearranged in terms of magnetic fields perpendicular B_{\perp} and parallel B_{\parallel} to the CNT axis, and reads

$$\begin{aligned}
 \hat{H}_{\text{CNT}} &= \overbrace{\left(\varepsilon_d \hat{I}_{\sigma} \otimes \hat{I}_{\tau} + \frac{\Delta_{KK'}}{2} \hat{I}_{\sigma} \otimes \hat{\tau}_z + \frac{\Delta_{\text{SO}}}{2} \hat{\sigma}_z \otimes \hat{\tau}_x \right)}^{\hat{H}_{\text{CNT}}^{(0)}} + \\
 &+ \underbrace{\left(\frac{1}{2} g_s \mu_B B_{\perp} \hat{\sigma}_x \otimes \hat{I}_{\tau} \right)}_{\hat{H}_{\perp}} + \underbrace{\left(g_{\text{orb}} \mu_B B_{\parallel} \hat{I}_{\sigma} \otimes \hat{\tau}_x + \frac{1}{2} g_s \mu_B B_{\parallel} \hat{\sigma}_z \otimes \hat{I}_{\tau} \right)}_{\hat{H}_{\parallel}} = \quad (5.5) \\
 &= \hat{H}_{\text{CNT}}^{(0)} + \hat{H}_{\perp} + \hat{H}_{\parallel}.
 \end{aligned}$$

At zero magnetic field the Hamiltonian reduces to $\hat{H}_{\text{CNT}} = \hat{H}_{\text{CNT}}^{(0)}$.

For a purely perpendicular and parallel magnetic field the energy level spectrum is plotted in Fig. 5.9(a) and (b) for one longitudinal mode taking into account

²As depicted in Sec. 5.1.1 the orientation of the magnetic field is with respect to the CNT axis.

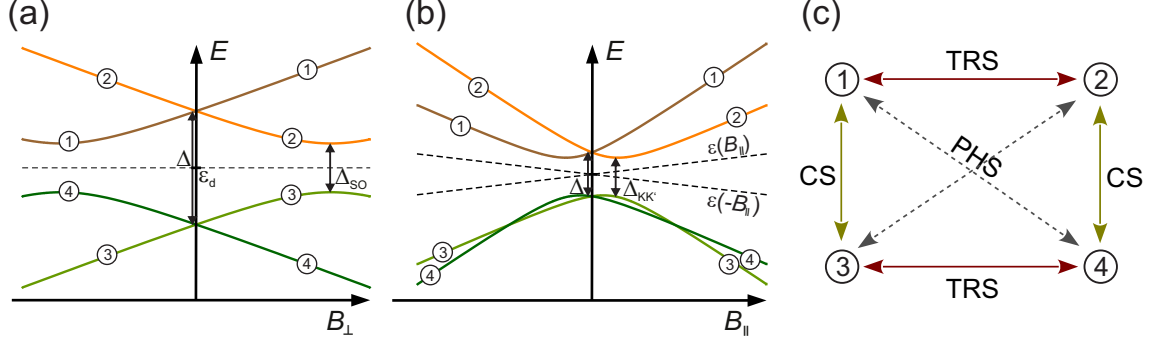


Figure 5.9: (a,b) Eigenenergies of the single-particle Hamiltonian 5.5 with finite spin-orbit coupling and KK' valley mixing in (a) perpendicular ($\phi = \pi/2$) and (b) parallel ($\phi = 0$) field orientation. The fourfold degeneracy is already lifted at $B = 0$ by $\Delta = \sqrt{\Delta_{\text{SO}}^2 + \Delta_{\text{KK}'}^2}$ forming two Kramers doublets symmetrically located around the reference energy ε_d . (c) The four eigenstates of one longitudinal shell with indicated conjugation by the different discrete symmetries: time-reversal symmetry (TRS), particle-hole symmetry (PHS), and chiral symmetry (CS).

finite spin-orbit interaction and finite KK' -mixing. This plot reproduces Fig. 3.8(d), where the fourfold degeneracy at $B = 0$ is lifted forming two Kramers doublets with spacing $\Delta = \sqrt{\Delta_{\text{SO}}^2 + \Delta_{\text{KK}'}^2}$. The eigenstates are labeled 1–4.

Zero magnetic field

In zero magnetic field one finds that the operator \hat{T} commutes with $\hat{H}_{\text{CNT}}^{(0)}$:

$$\hat{T} \hat{H}_{\text{CNT}}^{(0)} \hat{T}^{-1} = \hat{H}_{\text{CNT}}^{(0)}, \quad \text{or} \quad [\hat{T}, \hat{H}_{\text{CNT}}^{(0)}] = 0, \quad (5.6)$$

and the \hat{T} -conjugated pairs of states are connected by

$$\hat{T}|1\rangle = \kappa|2\rangle, \quad \hat{T}|2\rangle = \kappa|1\rangle, \quad \hat{T}|3\rangle = \kappa|4\rangle, \quad \hat{T}|4\rangle = \kappa|3\rangle. \quad (5.7)$$

From diagonalization of the Hamiltonian in Eq. 5.5 one finds that the level pairs $(1, 2)_T$ and $(3, 4)_T$ form the Kramers pairs at $B = 0$ with energy spacing $\Delta = \sqrt{\Delta_{\text{SO}}^2 + \Delta_{\text{KK}'}^2}$.

Similar, the operator \hat{P} anti-commutes with $(\hat{H}_{\text{CNT}}^{(0)} - \varepsilon_d \hat{I}_{\sigma} \otimes \hat{I}_{\tau})$:

$$\begin{aligned} \hat{P}(\hat{H}_{\text{CNT}}^{(0)} - \varepsilon_d \hat{I}_{\sigma} \otimes \hat{I}_{\tau}) \hat{P}^{-1} &= -(\hat{H}_{\text{CNT}}^{(0)} - \varepsilon_d \hat{I}_{\sigma} \otimes \hat{I}_{\tau}), \quad \text{or} \\ \{\hat{P}, (\hat{H}_{\text{CNT}}^{(0)} - \varepsilon_d \hat{I}_{\sigma} \otimes \hat{I}_{\tau})\} &= 0, \end{aligned} \quad (5.8)$$

with the corresponding \hat{P} -conjugated pairs

$$\hat{P}|1\rangle = \kappa|4\rangle, \quad \hat{P}|2\rangle = -\kappa|3\rangle, \quad \hat{P}|3\rangle = -\kappa|2\rangle, \quad \hat{P}|4\rangle = \kappa|1\rangle, \quad (5.9)$$

and ε_d stands for the reference energy of the considered longitudinal mode of the nanotube quantum dot.

Finally, the anti-commutation of the $\hat{\mathcal{C}}$ with $(\hat{H}_{\text{CNT}}^{(0)} - \varepsilon_d \hat{I}_\sigma \otimes \hat{I}_\tau)$ is given by

$$\begin{aligned} \hat{\mathcal{C}}(\hat{H}_{\text{CNT}}^{(0)} - \varepsilon_d \hat{I}_\sigma \otimes \hat{I}_\tau) \hat{\mathcal{C}}^{-1} &= -(\hat{H}_{\text{CNT}}^{(0)} - \varepsilon_d \hat{I}_\sigma \otimes \hat{I}_\tau), \quad \text{or} \\ \{\hat{\mathcal{C}}, (\hat{H}_{\text{CNT}}^{(0)} - \varepsilon_d \hat{I}_\sigma \otimes \hat{I}_\tau)\} &= 0, \end{aligned} \quad (5.10)$$

with the $\hat{\mathcal{C}}$ -conjugated pairs

$$\hat{\mathcal{C}}|1\rangle = |3\rangle, \quad \hat{\mathcal{C}}|2\rangle = |4\rangle, \quad \hat{\mathcal{C}}|3\rangle = |1\rangle, \quad \hat{\mathcal{C}}|4\rangle = |2\rangle. \quad (5.11)$$

Figure 5.9(c) shows how the four eigenstates of one longitudinal CNT mode are conjugated by these symmetries.

Finite (perpendicular) magnetic field

Now we investigate the symmetry behavior of the minimal Hamiltonian at a finite field perpendicular to the CNT axis. The effect of TRS is equal to a switching of the field orientation ($\vec{B} \rightarrow -\vec{B}$) in Fig. 5.9(a). The states $1 \leftrightarrow 4$ and $2 \leftrightarrow 3$ are conjugated by the PHS which is equivalent to the mirroring of the states on the reference energy ε_d . Note that PHS does not refer here to the symmetry of electrons and holes, but to the energetic symmetry with respect to ε_d . The CS is a combination of TRS and PHS and connects the levels $1 \leftrightarrow 3$ and $2 \leftrightarrow 4$.

While the TRS and CS are broken at $B_\perp \neq 0$,

$$\hat{\mathcal{T}} \hat{H}_\perp(B_\perp) \hat{\mathcal{T}}^{-1} = -\hat{H}_\perp(B_\perp) = \hat{H}_\perp(-B_\perp), \quad \text{or} \quad \{\hat{\mathcal{T}}, \hat{H}_\perp(B_\perp)\} = 0, \quad (5.12)$$

$$\hat{\mathcal{C}} \hat{H}_\perp(B_\perp) \hat{\mathcal{C}}^{-1} = \hat{H}_\perp(B_\perp) = -\hat{H}_\perp(-B_\perp), \quad \text{or} \quad [\hat{\mathcal{C}}, \hat{H}_\perp(B_\perp)] = 0, \quad (5.13)$$

the comparison with Eq. 5.8 shows that the PHS persists:

$$\hat{\mathcal{P}} \hat{H}_\perp(B_\perp) \hat{\mathcal{P}}^{-1} = -\hat{H}_\perp(B_\perp) = \hat{H}_\perp(-B_\perp), \quad \text{or} \quad \{\hat{\mathcal{P}}, \hat{H}_\perp(B_\perp)\} = 0, \quad (5.14)$$

which implies

$$\begin{aligned} \hat{\mathcal{P}}(\hat{H}_{\text{CNT}} - \varepsilon_d \hat{I}_\sigma \otimes \hat{I}_\tau) \hat{\mathcal{P}}^{-1} &= -(\hat{H}_{\text{CNT}} - \varepsilon_d \hat{I}_\sigma \otimes \hat{I}_\tau), \quad \text{or} \\ \{\hat{\mathcal{P}}, (\hat{H}_{\text{CNT}} - \varepsilon_d \hat{I}_\sigma \otimes \hat{I}_\tau)\} &= 0. \end{aligned} \quad (5.15)$$

As shown in the Supplementary Material of [Schmid et al., 2014] the same behavior can be found in parallel field, with the constraint that one has to define a reference energy $\varepsilon(B_\parallel)$ which depends on the parallel magnetic field component (see dashed

lines in Fig. 5.9(b)). In conclusion this means that the PHS stays intact in finite perpendicular and parallel field and one can affirm that this is also true for arbitrary field orientations.

The important outcome of the consideration of the symmetry operations in finite field is that the conjugation relations impose certain constraints in the many-body theory based on the Keldysh field integral [Altland and Simons, 2010], introducing a new many-body selection rule which suppresses the transitions between the $\hat{\mathcal{P}}$ -conjugated pairs $1 \leftrightarrow 4$ and $2 \leftrightarrow 3$.

Kondo transitions

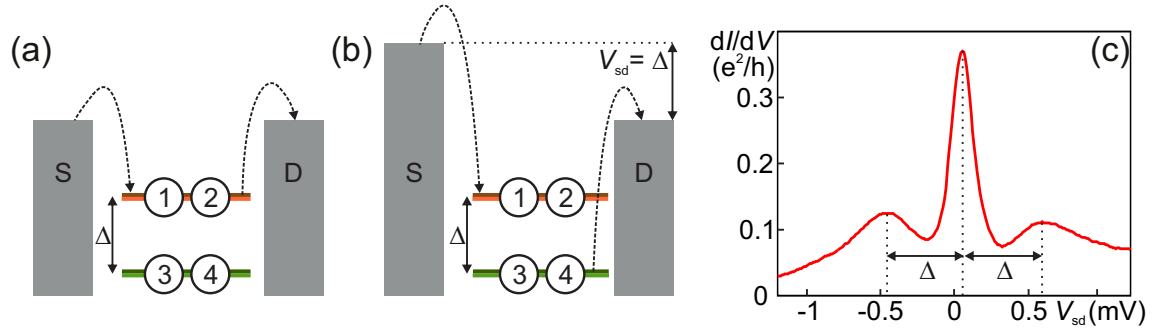


Figure 5.10: (a) Elastic Kondo transition at $V_{sd} = 0$ between the TRS pair. Here the arrows illustrate as example the intra-Kramers transition $1 \rightarrow 2$. (b) Inelastic chiral inter-Kramers Kondo transition at $V_{sd} = \Delta$ between the CS pairs, $4 \rightarrow 2$ or $3 \rightarrow 1$. (c) Differential conductance as function of the bias voltage for $N_{el} = 21$ ($V_g = 2.38$ V). The central peak originates in elastic processes (as in (a)) and satellite peaks at $V_{sd} = \pm\Delta$ are explained by inelastic tunneling processes (as in (b)).

The observed features at zero magnetic field, namely the central zero-bias peak and the satellite peaks, can be attributed to the transitions which are allowed by the symmetry consideration. As depicted in the Figs. 5.10(a),(b) there are two different Kondo transitions possible between the two times degenerate Kramers pairs with spacing Δ at $B = 0$. For zero bias voltage in (a) the TRS pairs are involved, leading to so-called intra-Kramers transitions. Since both level pairs ($|1\rangle, |2\rangle$) and ($|3\rangle, |4\rangle$) are degenerate, the condition for the occurrence of the zero-bias peak in Fig. 5.10(c) is fulfilled. A bias voltage $V_{sd} = \pm\Delta$ enables the inelastic, in this case so-called chiral inter-Kramers transitions between the CS pairs. These processes lead to Kondo enhanced co-tunneling for $V_{sd} = \pm\Delta$, inducing satellite peaks in the experiment.

5.2.2 Characterization of the Kondo effect at zero field

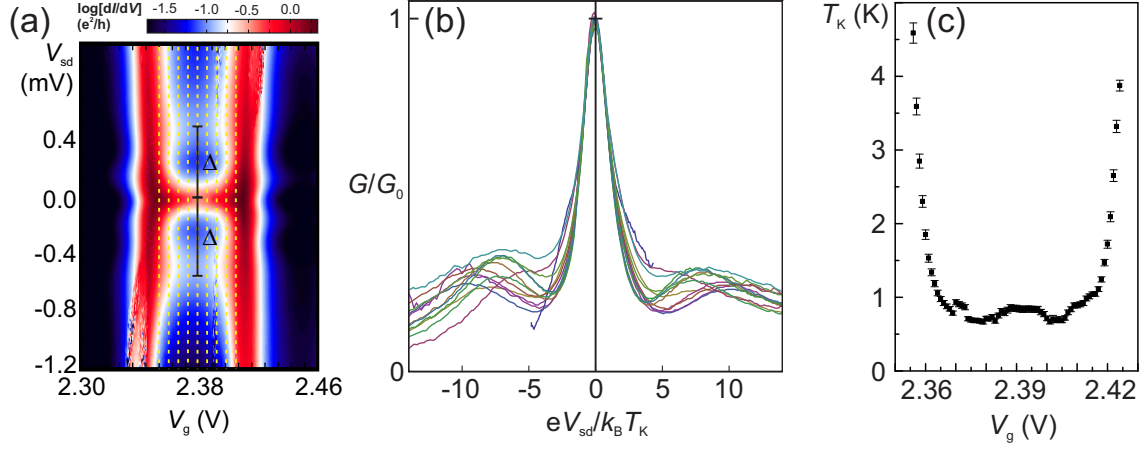


Figure 5.11: (a) Stability diagram at $N_{el} = 21$ showing a pronounced zero-bias peak at $V_{sd} = 0$ mV and broad satellite peaks at finite bias $V_{sd} = \pm\Delta \simeq \pm 0.5$ mV. (b) Bias traces extracted along the dashed yellow lines in (a), rescaled by the corresponding Kondo temperature T_K , and normalized by $G_0 = G(V_{sd} = 0)$. The traces collapse onto a single curve at low bias, proving the Kondo origin. (c) Kondo temperature T_K for several bias traces in (a) within the Coulomb diamond $N_{el} = 21$ as function of the gate voltage V_g . *Cool down 2*.

In order to prove the Kondo origin of the zero-bias anomaly the bias dependence of the conductance traces $G(V_{sd})$ is measured at different gate voltages within the Coulomb diamond with $N_{el} = 21$, indicated by the yellow dashed lines in Fig. 5.11(a). For every single curve T_K is determined from non-equilibrium measurements of the central Kondo peak obeying $G(eV_{sd}/k_B T_K)/G_0 \simeq 2/3$ with $G_0 = G(V_{sd} = 0)$ (see Eq. 4.1, Fig. 4.3(b), and [Kretinin et al., 2012], [Pletyukhov and Schoeller, 2012]). The traces are normalized and the bias voltage is rescaled to universal units for each curve with the respective Kondo temperature T_K . In Fig. 5.11(b) the collapse of all curves onto a universal line shape in the low-bias region confirms the Kondo origin of the observed features. The loss of the universality in the satellite peaks in Fig. 5.11(b) is expected since full universality is, according to [Yamada et al., 1984], only given if the ratio T_K/Δ is constant. This is not fulfilled, since the satellite peak position Δ is constant for one charging state but T_K varies with the gate voltage. This gate voltage dependence of the Kondo temperature T_K is plotted in Fig. 5.11(c). A U-shape with a strong enhancement of T_K close to the charge degeneracy points of the QD is observed, similar to [Cronenwett et al., 1998], [van der Wiel et al., 2000]. This increase of T_K is caused by the exponential dependence of the Kondo

temperature on the QD potential with respect to the Fermi level of source and drain lead:

$$T_K \propto \exp[-\pi(\mu_L - \mu)/2\Gamma],$$

where the Fermi potential of the leads is $\mu_L = \mu_S = \mu_D$ for $V_{sd} = \mu_S - \mu_D = 0$, and Γ is the total tunnel rate on and off the quantum dot. Tuning the gate voltage to the charge degeneracy points brings the QD potential in resonance with the Fermi levels of the leads, i.e. $(\mu_L - \mu) \rightarrow 0$. An enhancement of the Kondo temperature above the measurement error also occurs in the center of the Coulomb diamond with a maximum at $V_g \simeq 2.39$ V. The origin of this feature is so far unexplained.

5.2.3 Evolution of the Kondo resonances in a perpendicular magnetic field

The data presented here focus on the Coulomb blockade valley $N_{el} = 21$. The chip carrier rotation is chosen such that the magnetic field is perpendicular to the chip surface and thus perpendicular to the CNT axis. The conductance is measured as function of magnetic field and bias voltage at fixed $V_g = 2.39$ V in the center of the Coulomb diamond. Fig. 5.12(a) shows the evolution of central and satellite peaks in the field perpendicular to the nanotube axis. As expected, the central peak splits above a certain critical field in a first sub-linear then linear way according to the Zeeman energy $E_Z = 2\delta_\perp = g'_s\mu_B B$. The satellite peaks, on contrary, remain nearly constant up to 3 T.

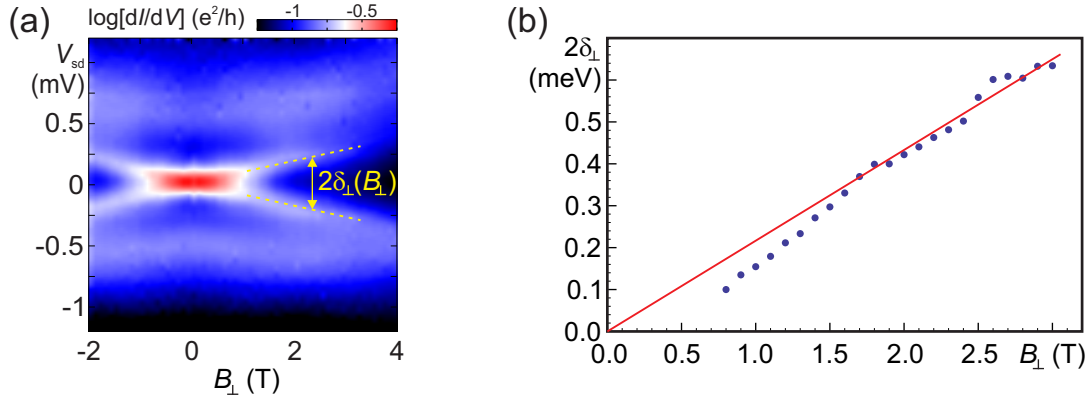


Figure 5.12: (a) Differential conductance $G(B_\perp, V_{sd})$ as function of a perpendicular magnetic field and of the bias voltage applied between source and drain contact in valley $N_{el} = 21$. The yellow dashed line highlights the linear splitting $2\delta_\perp(B_\perp)$ of the central peak. (b) Extracted peak distances $2\delta_\perp$ in (a) for increasing perpendicular magnetic fields B_\perp . *Cool down 2.*

In Fig. 5.12(b) the peak distances $2\delta_{\perp}$ are extracted from the measurement shown in (a) and plotted versus the magnetic field. The peak distance displays a sub-linear behavior evolving into a linear splitting for higher field values. To extract the effective g -factor g'_s the linear fitting is done for different sets of data points, where gradually data points on the low-field range are rejected up to some threshold value B_{linear} . In Fig. 5.13(a) the resulting g'_s -factor is plotted versus this cut-off field B_{linear} . Neglecting the values for high B_{linear} where the fitting is poor due to the small number of data points, the g'_s -factor increases for higher cut-off fields since the sub-linear regime is gradually discarded. For $0.9 \text{ T} < B_{\text{linear}} < 2.7 \text{ T}$ we obtain a result of $g'_s = 1.85 \pm 0.05$. This value is used for the evaluation of the ratio of $\Delta_{\text{SO}}/\Delta_{\text{KK'}}$ (see below) and for the plot in Fig. 5.13(b), where the energy difference is rescaled by the Zeeman energy using $g'_s = 1.85$ and plotted versus the perpendicular magnetic field. In this kind of plot the sub-linear regime below $B \approx 1.6 \text{ T}$ is better visible and shows the importance of the extensive effort in selecting the correct range for fitting the g'_s -factor.

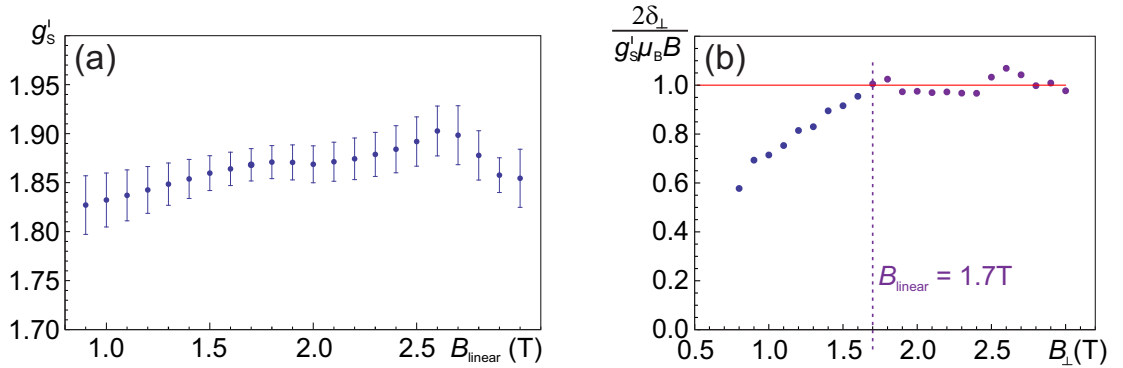


Figure 5.13: (a) Fitted g'_s -factor versus cut-off field B_{linear} . (b) Energy difference of split central peak $2\delta_{\perp}$ divided by Zeeman energy $E_Z = g'_s \mu_B B$ shows sub-linear behavior in the low-field region evolving into a linear behavior at higher fields. The effective g -factor is set to $g'_s = 1.85$.

In Fig. 5.14 the peak positions from the measurement shown in Fig. 5.12(a) have been extracted and plotted in universal units, where the energies are scaled by the Kondo energy $k_B T_K$. The Kondo temperature $T_K = 0.86$ for the fixed gate voltage in valley $N_{\text{el}} = 21$ is determined by the condition $G(eV_{\text{sd}}/k_B T_K \simeq 2G_0/3)$, where $G_0 = G(V_{\text{sd}} = 0, T = 30 \text{ mK})$. The absence of a splitting of the satellite peaks is explained by the lack of the transitions $1 \leftrightarrow 4$ and $2 \leftrightarrow 3$, being a direct consequence of the many-body selection rule suppressing these PHS transitions as explained in Sec. 5.2.1. This is in contrast to previous measurement by [Jespersen et al., 2011], where the co-tunneling lines in the Coulomb diamonds have been

traced in dependence of an external magnetic field and all transition could be seen.

In Fig. 5.14 the experimental central peak positions (orange dots) are fitted with the energies of the intra-Kramers transitions $1 \leftrightarrow 2$ and $3 \leftrightarrow 4$ (gray lines), while the satellites (blue dots) are in good agreement with the chiral inter-Kramers transitions $1 \leftrightarrow 3$ and $2 \leftrightarrow 4$ (blue lines). At sufficiently low perpendicular fields $g_s \mu_B B_\perp < \Delta_{SO}$, as fulfilled in our measurement, the chiral inter-Kramers transitions do not depend on the magnetic field, leading to a constant satellite peak position Δ . In this low-field limit the energy splitting δ_\perp of both Kramers doublets is linear and identical resulting in a constant energy distance Δ between the chiral pairs $1 \leftrightarrow 3$ and $2 \leftrightarrow 4$.

The single-particle energy spectrum is used to fit the data points allowing us to extract the internal parameters of the CNT quantum dot which are listed in Table 5.2. The satellite peak position Δ is extracted directly from the experiment and the ratio $\Delta_{SO}/\Delta_{KK'}$ is obtained by the relation

$$g'_s = \frac{g_s}{\sqrt{1 + (\Delta_{SO}/\Delta_{KK'})^2}}. \quad (5.16)$$

The effective g -factor g'_s has been determined by the splitting of the central peak in the linear regime as shown in detail in Fig. 5.13, and $g_s = 2$. The details of the evaluation are given in the Supplementary Material of [Schmid et al., 2014].

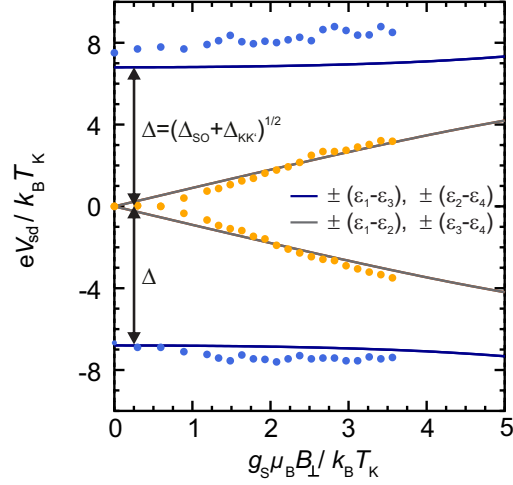


Figure 5.14: Extracted peak positions (points) from the measurement $G(B_\perp, V_{sd})$ in Fig. 5.12(a) in rescaled units (see text) plus underlying single-particle energy differences (lines) with fitted energies $\Delta_{SO} = 3.0 k_B T_K$ and $\Delta_{KK'} = 6.2 k_B T_K$. The gray lines represent the intra-Kramers transitions while the blue lines correspond to chiral inter-Kramers transitions describing the satellite peaks.

$N_{\text{el}} = 21$	g'_s	Δ	Δ_{SO}	$\Delta_{\text{KK}'}$
$T_K = 0.86 \text{ K}$	1.85 ± 0.05	0.51 meV $6.9 k_B T_K$	$(0.19 \pm 0.03) \text{ meV}$ $(2.8 \pm 0.2) k_B T_K$	$(0.47 \pm 0.01) \text{ meV}$ $(6.3 \pm 0.1) k_B T_K$

Table 5.2: Carbon nanotube quantum dot parameters for $N_{\text{el}} = 21$ obtained by fitting the dependence of the Kondo resonance peaks on a perpendicular magnetic field in Fig. 5.14 using the minimal Hamiltonian in Eq. 3.12.

5.2.4 Evolution of the Kondo resonances in a parallel magnetic field

Figure 5.15 displays a similar measurement on the same sample, now in parallel orientation of the in-plane magnetic field with respect to the CNT axis. It reveals a much richer structure, which can be explained by the additional Aharonov-Bohm term in the minimal Hamiltonian in Eq. 3.12. The measurement of the differential conductance versus parallel magnetic field and bias voltage is depicted in Fig. 5.15(a).

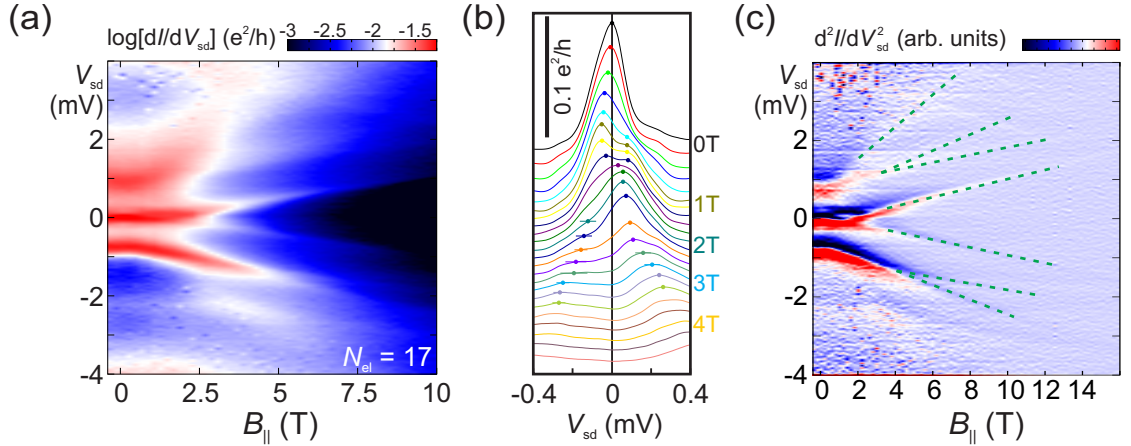


Figure 5.15: (a) Differential conductance $G(B_{\parallel}, V_{\text{sd}})$ as function of a parallel field and bias voltage, $N_{\text{el}} = 17$. (b) Detailed conductance traces $G(V_{\text{sd}})$ of the central low-bias peak for various magnetic field values with spacing $\Delta B_{\parallel} = 0.2 \text{ T}$. The traces are shifted for clarity. (c) Numerical derivative of the differential conductance measurement in (a) with respect to the bias voltage V_{sd} highlighting the evolution of the satellite peaks. *Cool down 3.*

Additionally, in Fig. 5.15(c) the derivative of the differential conductance is shown to emphasize the peaks in $G(V_{sd})$, where now, besides the splitting of the central zero-bias peak, also the satellites move and split in parallel field orientation. This is due to the magnetic field dependent energy spacing between the CS pairs. Hardly visible in this color scale is the peculiar behavior of the central peak at low fields. Therefore in Fig. 5.15(b) extracted conductance traces $G(V_{sd})$ around the central peak (low bias range in (a)) are shown for increasing magnetic field. The increment in $B_{||}$ is 0.2 T, and the lines are shifted for clarity. The central peak splits into two peaks at $B_{||} = 1$ T, which merge again at $B_{||} = 1.6$ T before they finally split at $B_{||} = 2.4$ T. An asymmetry appears in the heights of the two peaks, which changes from an enhanced conductance of the negative bias voltage peak for low fields to an enhancement of the peak at positive bias voltage for higher fields. A possible explanation is a different coupling of the two states involved in the transition to the leads. The states cross and change their relative position to each other.

Again, the peak positions are extracted from several bias traces $G(V_{sd})$ and plotted in rescaled units versus $g_s\mu_B B_{||}/k_B T_K$, see Fig. 5.16. The Kondo temperature is determined in the center of the Coulomb diamond $N_{el} = 17$ from the bias voltage dependence $G(V_{sd})$ as $T_K = 1.12$ K.

Also in the parallel field orientation, the single-particle Hamiltonian is used to explain the behavior of the Kondo zero-bias and satellite peaks. Due to the additional Aharonov-Bohm term the energy diagram in Fig. 5.9(b) looks less symmetric than for the perpendicular field. Since the sample and thus the nanotube is the same, there is again finite spin-orbit coupling and valley mixing, which have to be included in the Hamiltonian. The detailed parameters are slightly different for $N_{el} = 17$ compared to $N_{el} = 21$, see Table 5.2. The additional Aharonov-Bohm term leads to a crossing of level 3 and 4 at finite field, explaining the splitting, merging and final splitting of the zero-bias peak. This qualitative agreement is nicely visible in the low-field zoom plotted in Fig. 5.16(b), where the data points describe an eye-like shape, which is qualitatively reproduced by the corresponding single-particle energy differences $\pm(\varepsilon_3 - \varepsilon_4)$ (gray solid line). Since our linear theory is not able to capture the full range of the magnetic field, Fig. 5.16(a) is divided into a low-field region (yellow shaded) and a high field region with respectively adjusted parameters. In the two regions different orbital magnetic momentum values g_{orb}, g'_{orb} result from fitting. This becomes visible as discontinuity in the fit lines in Fig. 5.16(a).

In the high field regime the magnetic field dependence of the spectrum becomes linear with slopes α depending on the high-field orbital magnetic moment g'_{orb} . Additionally, according to our theory in the high field regime, i.e. $g_s\mu_B B_{||} \gg \Delta$, one

can expand the energy dispersion in linear order to obtain the expression

$$[\varepsilon_1(B_{\parallel}) - \varepsilon_2(B_{\parallel})] - [\varepsilon_4(B_{\parallel}) - \varepsilon_3(B_{\parallel})] \simeq 2\Delta_{\text{SO}}. \quad (5.17)$$

This relation provides a direct access to the spin-orbit coupling energy Δ_{SO} and thus, in combination with Δ , also $\Delta_{\text{KK}'}$. Furthermore, from the high field asymptotes one can extract the orbital magnetic moment g'_{orb} via

$$[\varepsilon_1(B_{\parallel}) - \varepsilon_3(B_{\parallel})] + [\varepsilon_2(B_{\parallel}) - \varepsilon_4(B_{\parallel})] \simeq 4g'_{\text{orb}}\mu_{\text{B}}B_{\parallel}. \quad (5.18)$$

For more details, see [Schmid et al., 2014]. The resulting fit parameters are listed in Table 5.3.

$N_{\text{el}} = 17$	g_{orb}	g'_{orb}	Δ	Δ_{SO}	$\Delta_{\text{KK}'}$
$T_{\text{K}} = 1.12 \text{ K}$	4.8	2.74	0.80 meV $8.3 k_{\text{B}}T_{\text{K}}$	0.35 meV $3.6 k_{\text{B}}T_{\text{K}}$	0.72 meV $7.5 k_{\text{B}}T_{\text{K}}$

Table 5.3: Level spectrum parameters for $N_{\text{el}} = 17$ obtained by fitting the dependence of the Kondo resonance peaks on a low parallel magnetic field using the minimal Hamiltonian in Eq. 3.12. For good agreement over the full examined field range the orbital magnetic moment has to be considered independently for the low- and high-field range as g_{orb} and g'_{orb} , respectively.

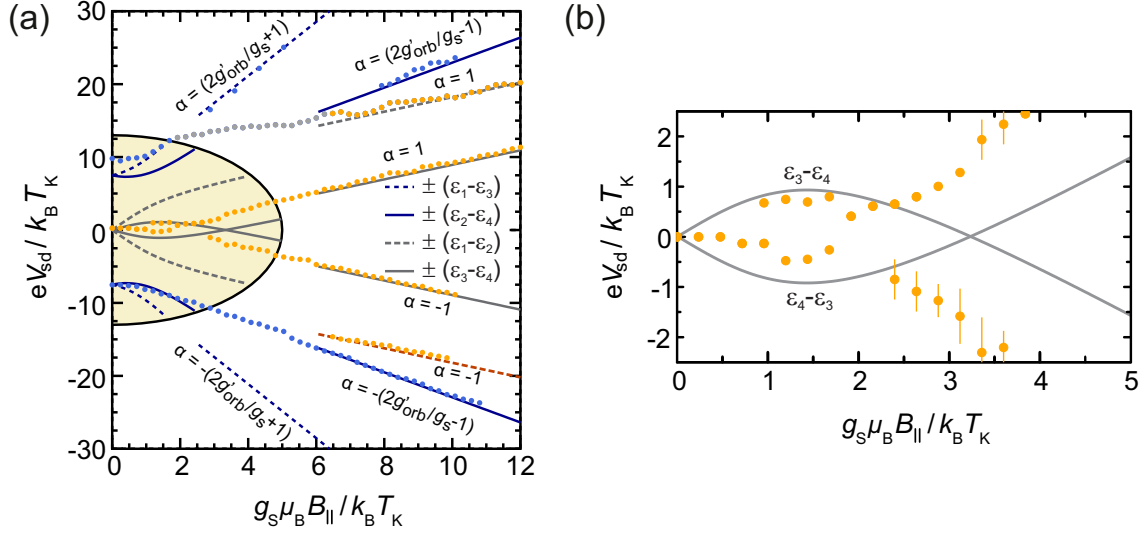


Figure 5.16: (a) Extracted peak positions (points) from Fig. 5.15 in rescaled units (see text) plus underlying single-particle energy spectrum (lines) using the fit parameters Δ_{SO} and $\Delta_{KK'}$. The magnetic field dependence of the satellite peaks is fitted with the chiral inter-Kramers transitions (solid and dashed blue lines). (b) A zoom into the low-bias and low-field region in (a) emphasizes the peculiar behavior of the central peak caused by the level crossing of the lower Kramers pair at finite field. The data points correspond to the values marked in Fig. 5.15(b). The gray lines show the fitted energy differences of the single-particle spectrum (intra-Kramers transitions) for the values given in Table 5.3.

5.2.5 Modeling with non-equilibrium many-particle theory

In the theory group of Prof. Dr. M. Grifoni (University of Regensburg) a non-equilibrium field theory has been developed, which can – by taking into account the symmetry relations of the CNT-Hamiltonian and the underlying single-particle spectrum – reproduce the measured conductance traces and the Kondo fine structure with very good agreement. While the $SU(2)$ symmetry case of this so-called slave boson Keldysh effective action formalism has already been published by [Smirnov and Grifoni, 2013a], [Smirnov and Grifoni, 2013b] the $SU(4)$ version is presented in [Schmid et al., 2014]. This theory is able to describe the dependence of the differential conductance on bias voltage, temperature, and magnetic field for the whole energy range relevant for Kondo physics in transport. It is also able to include the $SU(4)$ symmetry breaking due to the finite spin-orbit interaction Δ_{SO} and KK' -valley mixing $\Delta_{\text{KK}'}$ in our sample. Their effect are the inelastic Kondo enhanced co-tunneling features inducing the satellite peaks at $V_{\text{sd}} = \pm\Delta/e$ with $\Delta = (\Delta_{\text{SO}}^2 + \Delta_{\text{KK}'}^2)^{1/2}$. The selection rule deduced from the transformation behavior of the single-particle Hamiltonian enters the many-body theory and suppresses the Kondo transitions between the PHS pairs $1 \leftrightarrow 4$ and $2 \leftrightarrow 3$.

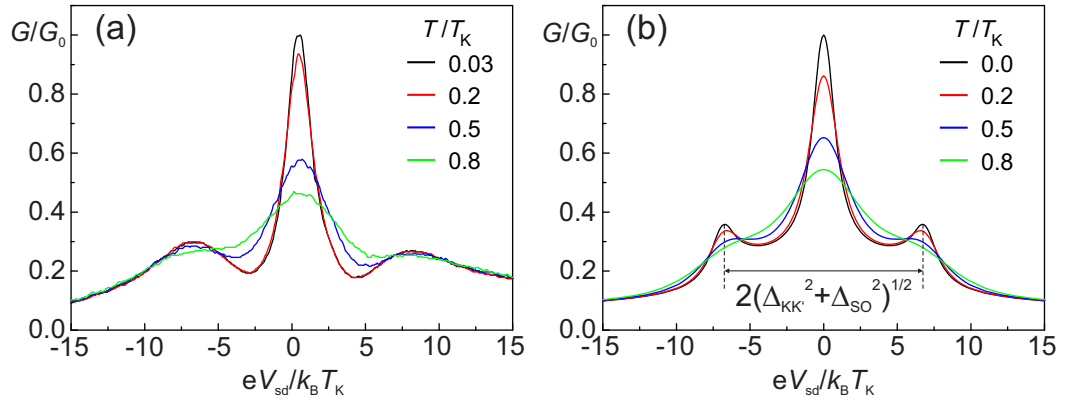


Figure 5.17: (a) Measured differential conductance as function of the rescaled bias voltage for different temperatures in units of the Kondo temperature $T_K = 0.86$ K. (b) Calculated bias traces for temperatures corresponding to the experiment in (a). The satellite peak spacing 2Δ is given by the obtained energies $\Delta_{\text{KK}'}$, Δ_{SO} and orbital g -factor g_{orb} .

In a first step the temperature dependence of the zero-bias peak and the satellites (Fig. 5.17(a)) in the center of the Coulomb diamond with $N_{\text{el}} = 21$ ($T_K = 0.86$ K) can be quantitatively reproduced by this theory (see Fig. 5.17(b)).

The central peak strongly depends on the temperature in agreement with the $SU(2)$ and $SU(4)$ Kondo effect, while the finite-bias peaks get increasingly washed out for

higher temperatures. The slower decay of the experimental conductance trace at higher V_{sd} leading to broader peaks compared with the theory can be explained by additional inelastic co-tunneling in the experiment, which is not captured by the effective action theory.

The magnetic field dependence of $G(V_{sd})$ in perpendicular orientation to the nanotube axis is accurately reproduced by the calculation, which explains the splitting of the central peak at a certain critical field in a first sub-linear and then linear way. In Fig. 5.18(b) theoretically calculated conductance curves for different perpendicular magnetic fields are shown, using the values listed in the Table 5.2. This work has been performed by Dr. S. Smirnov.

In the parallel field additionally the Aharonov-Bohm term has to be included leading to an orbital g -factor g_{orb} . The conductance traces can be reproduced with the non-equilibrium many-body theory by adjusting the two free parameters $\Delta_{SO}/\Delta_{KK'}$ and g_{orb} . In particular the qualitative behavior of the central peak is well reproduced, as can be seen in the insets of the Figs. 5.18(c),(d). The temporary splitting, merging and final splitting of the central peak is a consequence of the single electron level crossing as displayed in Fig. 5.9(b). Note that the numerical values of the energies given in the Figs. 5.18(b),(d) are in units of the Kondo energy $k_B T_K$.

In conclusion, we have measured the Kondo resonances in the case of a weakly broken $SU(4)$ symmetry, which induces satellite peaks at finite bias voltage. These features and their behavior in an external magnetic field are well understood in terms of a single-particle Hamiltonian plus a selection rule induced by the discrete symmetries in the CNT. Dr. S. Smirnov, theory group Prof. M. Grifoni, has developed a non-equilibrium many-body field theory based on the Keldysh formalism, where the selection rule naturally emerges from the symmetries in the $SU(4)$ case including symmetry breaking by a finite Δ_{SO} and $\Delta_{KK'}$. This theory is able to reproduce the differential conductance $G(V_{sd}, T, \vec{B})$ in the here accessed regime $k_B T_{min} \ll k_B T_K < \Delta$, $\Delta_{SO}, \Delta_{KK'} \ll E_C$, i.e. for a Kondo temperature which is much higher than the reachable base temperature T_{min} , $T_K \simeq 15 T_{min}$, but sufficiently small, $k_B T_K \simeq 0.13 \Delta$, to allow us to resolve the fine structure of the quantum dot.

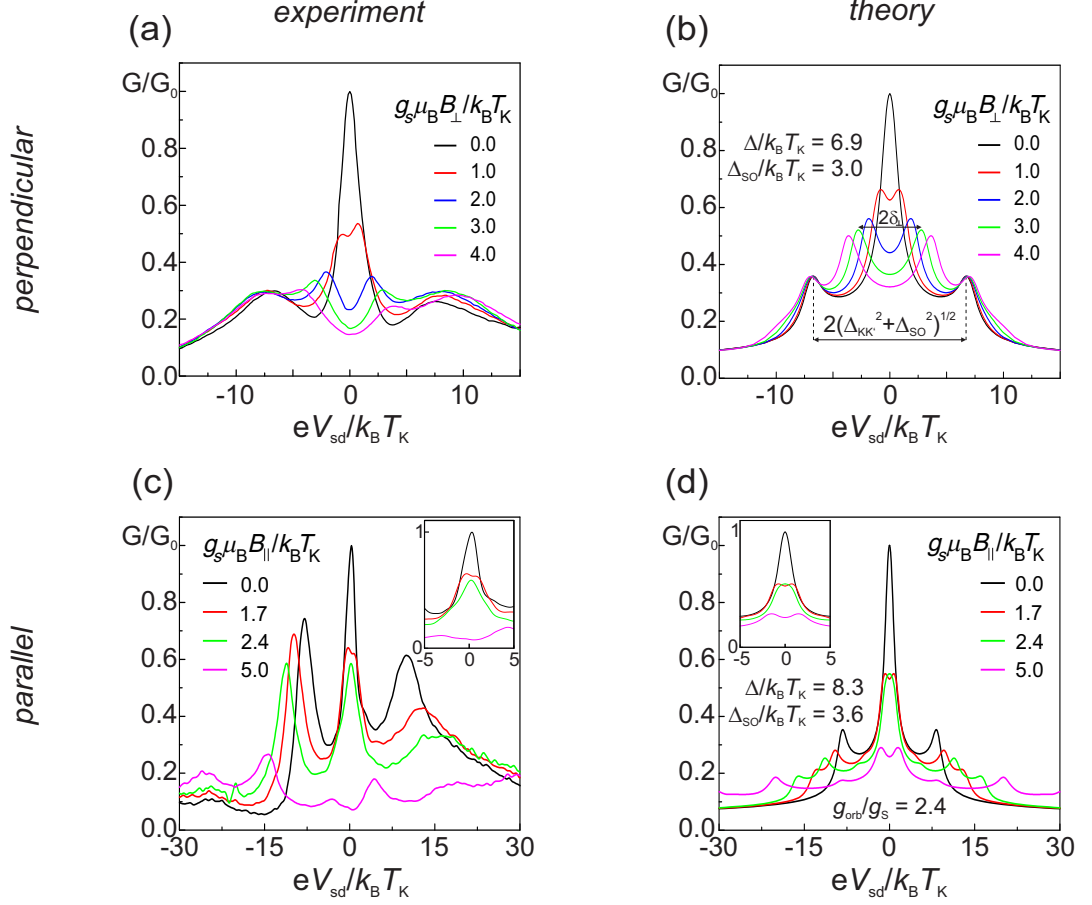


Figure 5.18: (a) Conductance traces taken from the measurement in Fig. 5.12(a) at different perpendicular magnetic fields. The axes are rescaled by the Kondo temperature $T_K = 0.86$ K. (b) Calculated conductance traces for different magnetic fields corresponding to the experiment in (a), which reproduce the exact behavior of zero-bias and satellite peaks in the experiment. (c) Conductance traces $G(V_{sd})$ from the measurement in the Coulomb valley $N_{el} = 17$ as shown in Fig. 5.15(a) at different magnetic fields with parallel orientation to the nanotube axis. The inset gives a zoom on the zero-bias peak behavior in the low-field range. The axes have been rescaled with the Kondo temperature $T_K = 1.12$ K. (d) Theoretical curves qualitatively reproduce the magnetic field dependence of the Kondo peak structure, including the peculiar splitting, merging and re-splitting of the central peak for low B_{\parallel} (see inset).

5.3 Additionally recorded data

This section presents an extract of preliminary results from further spectroscopy measurements which are still to be evaluated. The first section goes back to the Coulomb blockade regime, i.e. $\hbar\Gamma \ll k_B T \ll \Delta\epsilon$, and pursues excited states spectroscopy in an external magnetic field for the second Coulomb oscillation. The next section gives an outlook on the higher electron number regime, where the gate voltage dependence of the conductance has been investigated for increasing parallel magnetic fields. Finally, the Section 5.3.3 focuses on the Fabry-Pérot regime at the first holes. In a parallel magnetic field the zero-bias conductance develops a very rich structure which requires further analysis and theoretical efforts for a full understanding.

5.3.1 Two electron spectrum

Starting at the one-electron charging state which is well understood in the low-field range, the spectroscopy of the excited states of the two electron state requires a much deeper analysis. In this case, the exchange field – caused by electron-electron interaction – leads for instance to a splitting of singlet and triplet states.

In Fig. 5.19 the complex case of two electrons on the QD can be observed, which has been recorded in the same measurement run as the data in Fig. 5.2. The differential conductance is obtained by numerically differentiating the measured dc-current. In Fig. 5.19(a) the differential conductance is plotted versus gate and bias voltage around the second Coulomb oscillation, i.e. at the transition $1 < N_{\text{el}} < 2$. We recognize again three resonance lines (marked with yellow arrows) corresponding to the excited states of the first electron. They end in the charging state $N_{\text{el}} = 1$. The magnetic field dependence in Fig. 5.19(c) is identical to the measurements on the first electron in Sec. 5.1, but now symmetrically present at positive and negative bias voltages.

A much richer structure is formed by the excited lines of the two electron system, which run in the other direction into the Coulomb diamond with $N_{\text{el}} = 2$. In order to identify the states which contribute to the transport, the magnetic field dependence of the bias traces $dI/dV_{\text{sd}}(B_{\parallel}, V_{\text{sd}})$ is measured at gate voltage fixed both on the left and right side of the charge degeneracy point.³ This is indicated in Fig. 5.19(a) by the green and purple line and the corresponding measurements are shown in the Figs. 5.19(b) and (c), respectively.

The magnetic field dependent gate position of the charge degeneracy point in (a)

³The left side of the charge degeneracy point is defined by the charge occupation $N_{\text{el}} = 1$ of the quantum dot at $V_{\text{sd}} = 0$, while on the right side $N_{\text{el}} = 2$ at zero bias voltage.

induces in the Figs. 5.19(b,c) the modulation of the width in V_{sd} -direction, where the QD is in Coulomb blockade and the conductance is zero.

The magnetic field dependent measurement in Fig. 5.19(b) at the green line in (a) clearly shows the dispersion of the two-electron states. Already at $B_{||} = 0$ all degeneracies of the states are lifted. Well defined anti-crossings at finite field are indications for mixing terms in the corresponding Hamiltonian.

The magnetic field dependence of the bias traces $dI/dV_{sd}(B_{||}, V_{sd})$ at the gate position marked by the dashed purple line in Fig. 5.19(a) is mainly dominated by the single electron states, as can be seen in Fig. 5.19(c). These states show the well understood Kramers pair splitting at $B_{||} = 0$ for the first and second shell, caused by the finite spin-orbit interaction and KK' -mixing (compare with Chapter 5). Note, that energy differences cannot be extracted directly from bias voltage spacings, but they have to be rescaled by the geometric factor defined in Eq. 5.1.

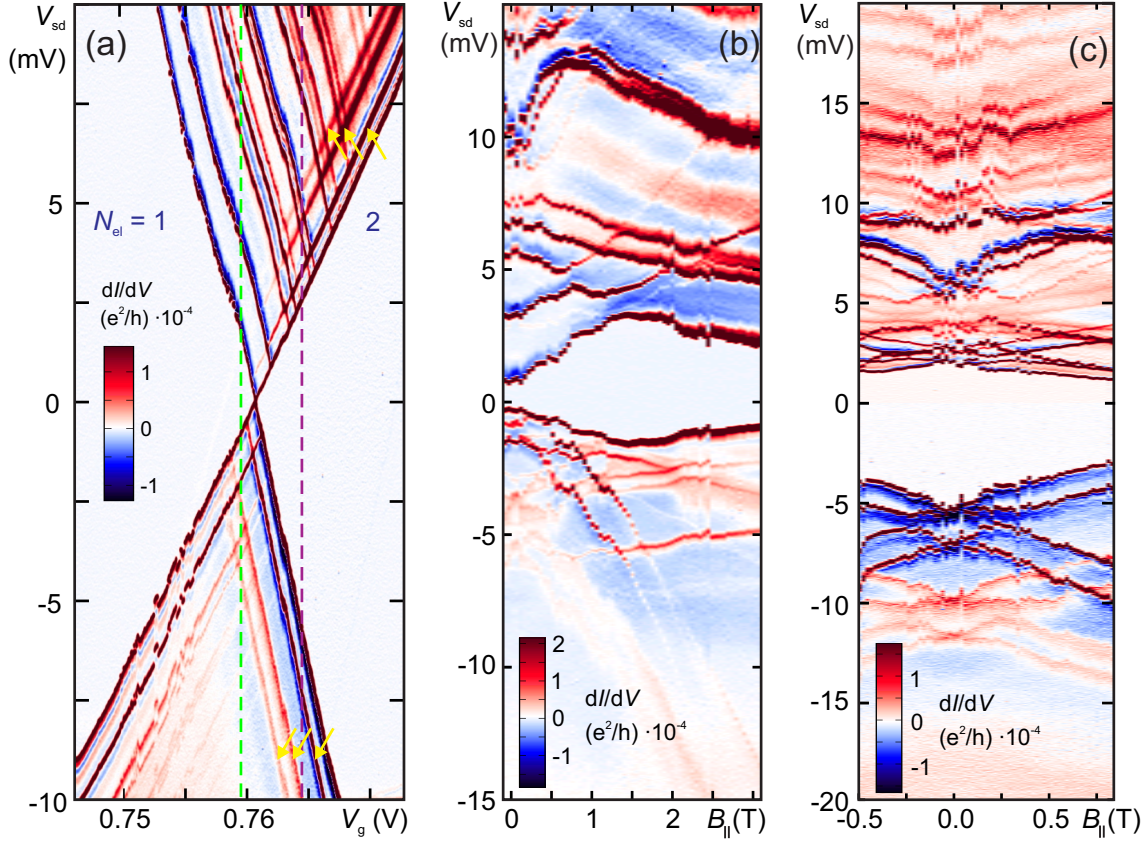


Figure 5.19: (a) Stability diagram of the second Coulomb oscillation $1 < N_{el} < 2$ for $B = 0$. Besides the three excited states of the first electron (marked with yellow arrows) running into the Coulomb diamond with $N_{el} = 1$ the spectroscopy measurement shows many excited states of the 2-electron state running in opposite direction towards $N_{el} = 2$. (b) Differential conductance as function of parallel magnetic field and bias voltage at a fixed gate voltage as indicated by the dashed green line in (a). (c) Same as in (b) but for a slightly modified gate voltage located on the "right side" of the charge degeneracy point (dashed purple line in (a)). *Cool down 3.*

5.3.2 Magnetic field effect on the conductance in the Kondo regime

In the regime dominated by the Kondo effect, in particular at $32 < N_{\text{el}} < 48$, the magnetic field dependence of the gate traces $dI/dV_{\text{sd}}(V_{\text{g}})$ has been measured in perpendicular and parallel orientation of the magnetic field with respect to the CNT axis. While in the perpendicular field there are only minor modifications of the conductance maxima positions with the field strength, the parallel magnetic field exhibits a strong effect on the conductance. This latter case is shown in Fig. 5.20(a). At zero magnetic field the well-known even-odd periodicity in the gate voltage dependence of the conductance due to the Kondo effect is observed, which reproduces the conductance trace shown in Fig. 5.7. The enhanced conductance in the Coulomb valleys with odd charges diminishes for increasing B_{\parallel} due to the suppressed Kondo resonance in a finite field [Jarillo-Herrero et al., 2005a]. However, the most striking features are the high conductance ridges at finite field, which are nearly horizontal for $N_{\text{el}} = 34, 38$, but show two branches with a strong dispersion for $N_{\text{el}} = 42, 48$.

The occurrence of these ridges coincides with kinks in slope of the conductance maxima with respect to the magnetic field, indicating ground state transitions. At the point of a level crossing⁴ a degeneracy is provided causing the $SU(2)$ Kondo enhanced conductance. The origin of the dispersive ridges for $N_{\text{el}} = 42, 46$ could be renormalization effects caused by charge fluctuations between the dot and asymmetrically coupled source and drain contacts [Grove-Rasmussen et al., 2012].

In Fig. 5.20(b) the bias voltage and magnetic field dependence of the differential conductance is shown for fixed gate positions in the center of the Coulomb valleys, which show the aforementioned peculiar conductance behavior at finite magnetic fields. This has been done for the four gate voltages marked with arrows in Fig. 5.20(a). The upper two plots in (b) depict one crossing, i.e. one conductance maximum at $V_{\text{sd}} = 0$, at the magnetic field value where the ridge in (a) occurs ($B_{\parallel} = 10 \dots 11$ T), while the plot for $N_{\text{el}} = 42$ clearly shows two conductance maxima for $V_{\text{sd}} = 0$ where resonance lines develop a crossing. The occurrence of these crossing points coincides exactly with the magnetic field values, where for fixed $V_{\text{g}} = 3.97$ in (a) the high conductance conditions are met. For $N_{\text{el}} = 46$ this peculiar behavior is hardly visible, and the lines are smeared out.

⁴In this case it is not sufficient to restrict to one carbon nanotube quantum dot shell (longitudinal mode).

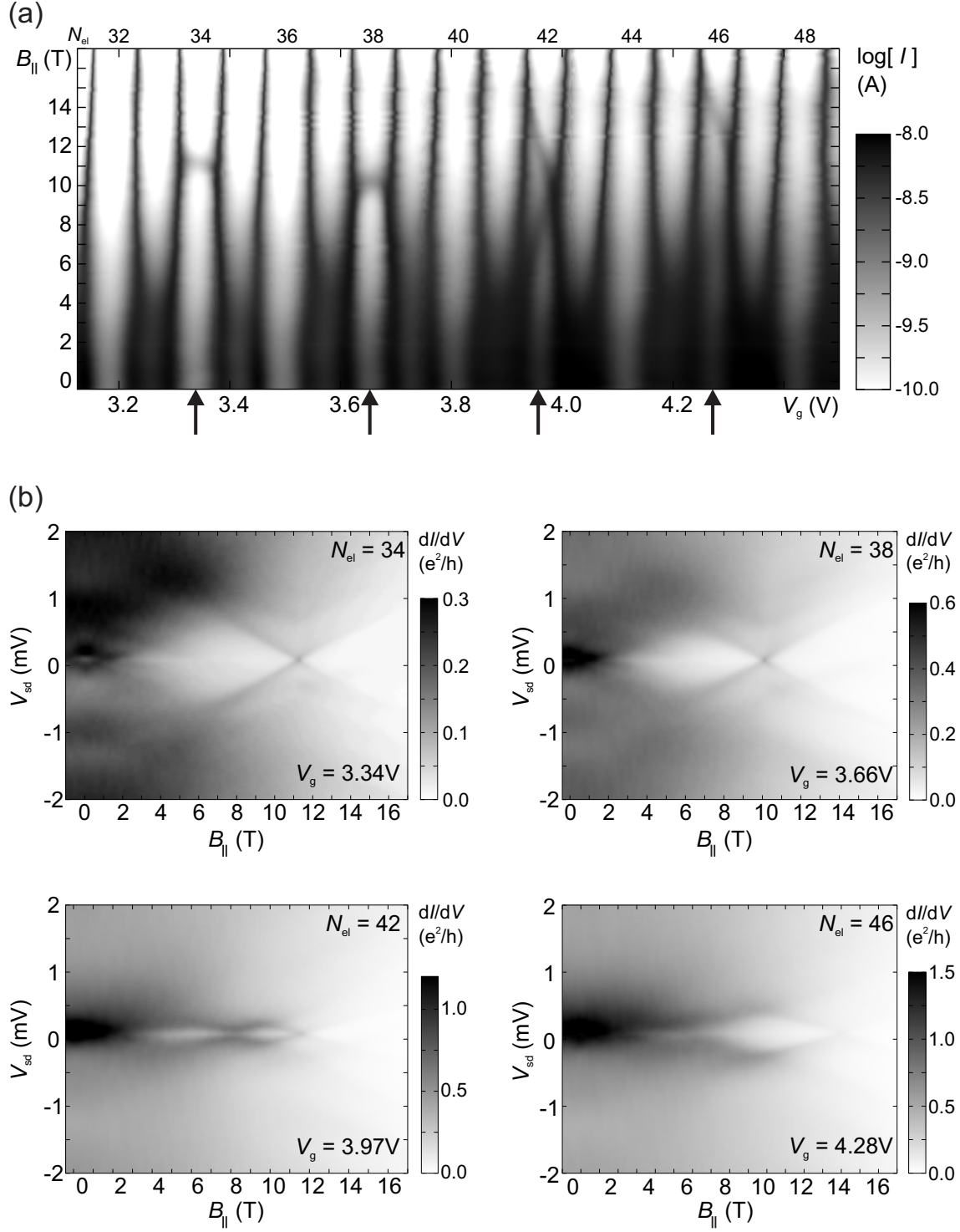


Figure 5.20: (a) Current as function of the gate voltage and a magnetic field parallel to the CNT axis in the regime $32 < N_{el} < 48$ for $V_{sd} = 50 \mu\text{V}$. (b) Bias traces $dI/dV_{sd}(V_{sd})$ for increasing parallel magnetic fields $B_{||}$ at fixed electron number N_{el} and gate voltage V_g (as marked in (a) by black arrows). *Cool down 3*.

5.3.3 Hole conduction

Figure 5.21 shows the differential conductance $G(B_{\parallel}, V_g)$ at $V_{sd} = 0$ on the hole conduction side for increasing magnetic fields parallel to the CNT axis. While in (a) the CNT is fixed to a parallel alignment of magnetic field and CNT axis and the magnetic field is increased stepwise, in (b) the magnetic field strength is at a constant value $|\vec{B}| = 17$ T and the sample orientation is rotated from a perpendicular to a parallel alignment to the CNT axis. This effectively increases the parallel field component as in Fig. 5.21(a) from $B_{\parallel} = 0$ T to $B_{\parallel} = 17$ T. In the zero-field case in Fig. 5.21(a) the conductance shows Fabry-Pérot features with a slow modulation over a broad gate voltage range, which nearly persist in a perpendicular magnetic field $B_{\perp} = 17$ T (this case corresponds to the trace $dI/dV_{sd}(V_g)$ at $B_{\parallel} = 0$ in Fig. 5.21(b)). Both for a pure parallel field (Fig. 5.21(a)) and for the case of an additional finite perpendicular field component in (b) a lot of sharp lines emerge running across the gate range for increasing magnetic field. At maximum parallel magnetic field, $B_{\parallel} = 17$ T, the gate dependence of the conductance exhibits a sharp Coulomb oscillation pattern. Not shown here is that a stability diagram $dI/dV_{sd}(V_g, V_{sd})$ at this high magnetic fields indeed shows the usual Coulomb diamonds according to a Coulomb blockade dominated transport regime.

Besides some transitions of the ground states, caused by the crossing of states, the external parallel magnetic field affects the tunnel coupling between QD and the leads, as reported by [Grove-Rasmussen et al., 2012].

A closer look on Fig. 5.21(a) reveals some nearly horizontal lines (green circles) for even hole numbers $N_h = 4, 8$, which may correspond to Kondo features. Besides some other effect this seems to be the most striking difference between Fig. 5.21(a) and (b). While in pure parallel field this ridges occur, they are clearly absent for an additional finite perpendicular magnetic field component in (b). An additional finite B_{\perp} impedes the level crossing, and the Kondo resonance is suppressed.

A parallel magnetic field strongly couples to the orbital degree of freedom of the quantum dot levels leading to a strong dispersion. If one considers more than one shell and a pure parallel field component, this can lead to a level crossing of states with opposite valley quantum number. The induced level degeneracy at finite field is required for the occurrence of a Kondo zero-bias anomaly (see Chapter 4). Despite the finite Δ_{SO} and $\Delta_{KK'}$ at such high magnetic fields ($B_{\parallel} > 10$ T) pure K and K' states are restored and their crossing results in an orbital $SU(2)$ Kondo effect [Jarillo-Herrero et al., 2005b].

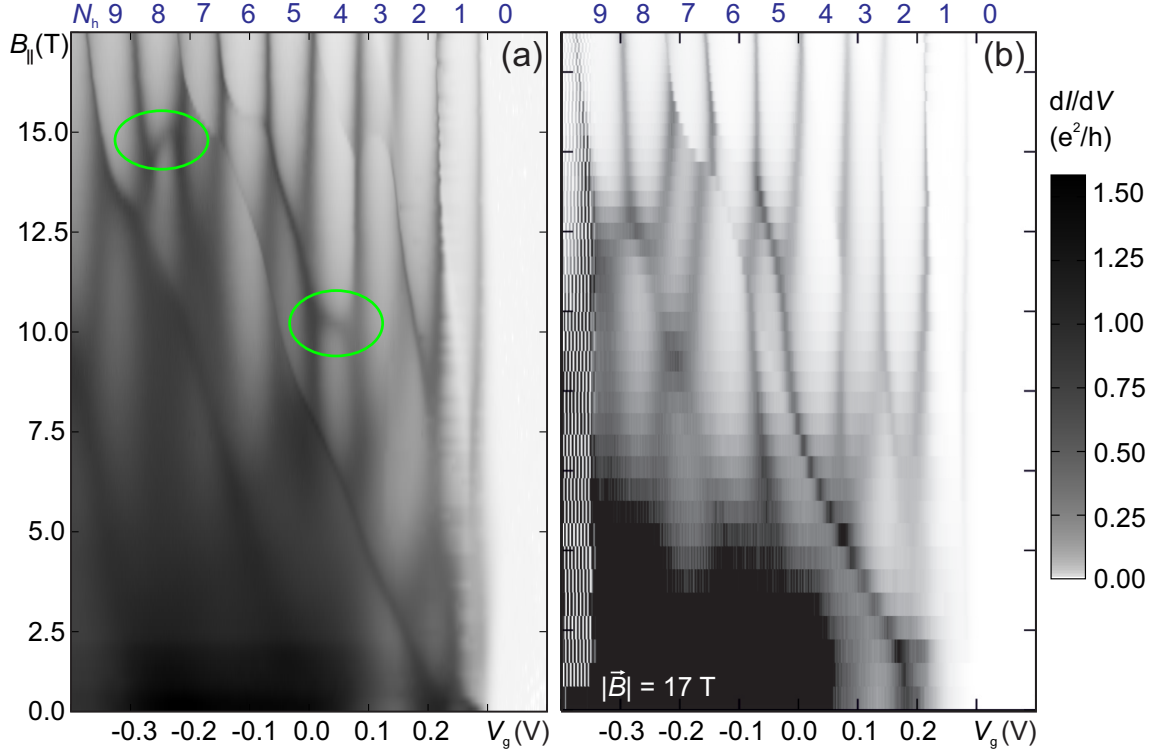


Figure 5.21: (a) Magnetic field dependence of the gate trace $dI/dV_{sd}(B_{||}, V_g)$ at zero bias voltage for $N_h < 10$ with fixed field orientation parallel to the CNT axis. (b) Dependence of the conductance on the gate voltage and of the parallel magnetic field component $B_{||} = |\vec{B}| \cdot \cos(\varphi)$ for zero bias voltage. Here, the total field strength is constant at $|\vec{B}| = 17 \text{ T}$, while the angle φ between CNT axis and magnetic field direction is rotated from perpendicular ($\varphi = 90^\circ$) to parallel ($\varphi = 0^\circ$) alignment, effectively increasing the parallel field component from $B_{||} = 0 \text{ T}$ to $B_{||} = 17 \text{ T}$. *Cool down 3.*

Chapter 6

Nanoelectromechanics with carbon nanotubes

Carbon nanotubes provide an extraordinary electro-mechanical beam resonator system, combining high stiffness with low mass density and an extremely small cross-section. Additionally, overgrown CNTs have shown very low mechanical damping [Hüttel et al., 2009b] allowing the observation of the interaction of single electron charging and tunneling with the mechanical motion [Hüttel et al., 2009b], [Steele et al., 2009]. The transversal vibration of doubly clamped CNTs exhibit very high resonance frequencies f_0 up to the GHz regime [Laird et al., 2012], where the condition for ground state cooling $\hbar f_0 \gg k_B T$ is already accessible with commercial dilution refrigerators ($T_{\text{base}} = 20 \text{ mK}$). This paves the way for fundamental experiments on quantum behaviors [LaHaye et al., 2004]. Due to the low resonator mass m the zero-point motion amplitude $x_{\text{ZP}} = \sqrt{\hbar/2m\omega_0}$ is relatively high, namely around 10 pm for our typical sample geometries, making a direct measurement of this pure quantum effect feasible.

Here, an overview is given over the first CNT resonator experiments in Regensburg, where the resonance frequency is detected via dc-current measurement and its dependence of the gate voltage is understood by the continuum beam model and classical electrostatic analysis. In addition, we have shown that a perpendicular magnetic field damps the CNT oscillation leading to a decrease of the Q -factor, and we employed the mechanical resonance to trace the charging state of the quantum dot in the Kondo regime.

Note, that all measurements presented in the following chapter have been performed on the same sample as the electronic transport spectroscopy in Chapter 5. The different cool-downs are labeled and assigned to the distinct measurement setups in the Appendix B.

6.1 Theoretical background of CNT nano-electro-mechanical systems

6.1.1 Actuation of mechanical vibration in suspended CNTs

Doubly clamped CNTs have several vibration modes with its characteristic energies and corresponding length dependencies as illustrated in Fig. 6.1. According to [Hüttel et al., 2008] the energetically lowest radial breathing mode (RBM), where the nanotube diameter oscillates uniformly, does not depend on the length L . Instead, the resonance frequency f_0 depends on the nanotube diameter d as $\propto 1/d$ resulting in typical energies around $hf_0 \simeq 10$ meV. The longitudinal stretching mode vibrates in axial direction. Here the resonance frequency exhibits a length dependence $\propto 1/L$ and a vibration energy around 0.1 meV. These modes typically are energetically below the electronic excitations which are related to the volume of the quantum confinement. Longitudinal modes have been observed in previous transport measurements as equidistant excitation lines, reflecting their harmonic nature [Sapmaz et al., 2006], [Hüttel et al., 2009a]. Also our measurements have shown such characteristic features, as for example in the charge transition $N_{\text{el}} = 1 \rightarrow 2$, indicating quantized longitudinal vibration modes.

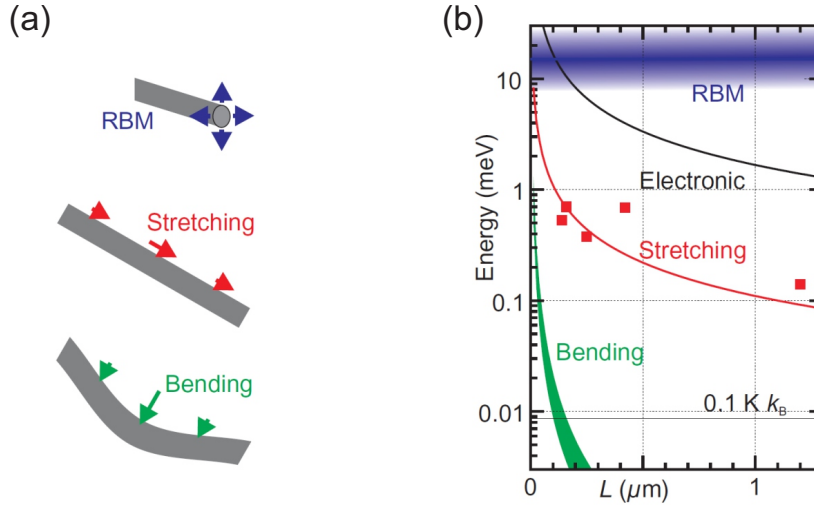


Figure 6.1: (a) Sketch of different CNT vibration modes. (b) Dependence of CNT vibration mode energies on the resonator length L with indication of the thermal energy in dilution refrigerators at typical $T = 0.1 \text{ K}$. Taken from [Hüttel et al., 2008].

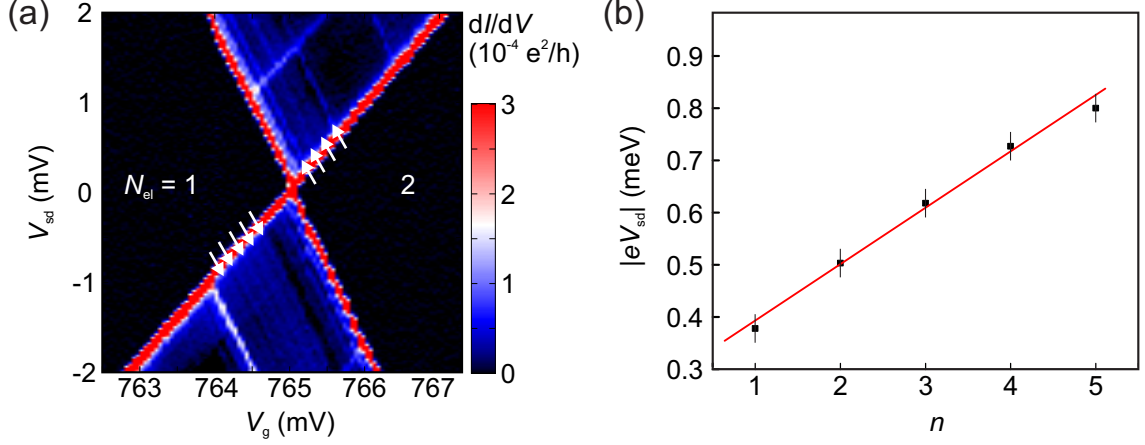


Figure 6.2: (a) Low-energy stability diagram for $1 < N_{el} < 2$ at $B_{||} = 10$ T. Equidistant low-energy excitation lines hint at longitudinal vibration modes. (b) Extracted energies of the five low-energetic resonance lines on the negative bias voltage side marked with white arrows in (a). The equidistant spacing of $\delta(eV_{sd}) \simeq 0.1$ meV is stressed by the linear fit (red line). *Cool down 3.*

Figure 6.2(a) depicts the stability diagram, i.e. the conductance as function of gate and bias voltage at $B_{||} = 10$ T for $N_{el} = 1 \rightarrow 2$. Besides pronounced electronic excited lines of the first electron at $eV_{sd} \simeq \pm 1$ meV, there are several low-energy excitations occurring as equidistant lines indicated by white arrows. In Fig. 6.2(b) the energy of five consecutive excitation lines on the negative bias voltage side are extracted showing an equidistant spacing of $\delta(eV_{sd}) \simeq 0.1$ meV. Comparing the energy spacing with the estimation $\delta \simeq 0.11 \text{ meV}/L[\mu\text{m}]$ in [Sapmaz et al., 2006] gives a theoretical resonator length of $L = 1.1 \mu\text{m}$ which is in fair agreement with the suspended length $L \simeq 700$ nm of the CNT device. Besides the characteristic harmonic spectrum of the observed excitation lines this endorses the hint at longitudinal stretching modes.

The energetically lowest mechanical excitation is given by the transversal bending mode where the CNT vibrates similar to a guitar or piano string, however at frequencies up to $10 - 1000$ MHz with corresponding energies $1 - 1000 \mu\text{eV}$. The frequency depends on the length of the resonator as $\propto 1/L^2$ and on the mechanical tension. The first detection of this mode has been achieved at room temperature using a frequency mixing setup [Sazonova et al., 2004].

In this chapter, the focus is on the transversal bending mode, on its excitation, detection, and its interplay with single electron tunneling and charging. The actuation of vibrations in suspended CNTs can be done in different ways.

Any ac-force at these frequencies can drive the CNT resonator. Several possibilities have been suggested and accomplished in literature to drive NEMS.

As an overview, these are:

- Piezo

In this simplest method the whole structure is mounted on a vibrating piezo substrate [Li and Evoy, 2005]. The actuation mechanism itself relies on the inertia of the resonator. Disadvantages are the low performance of common piezo crystals and the necessary high voltages causing perturbing high electric fields.

- Lorentz force

If the resonator structure is conducting one can apply a constant magnetic field perpendicular to the vibration plane. An additional ac-current through the resonator then induces an oscillatory Lorentz force [Cleland and Roukes, 1996]. However, this method does not work for isolating and highly resistive resonators.

- Electrostatic

The most convenient method is to drive CNT resonators by an alternating electric field from a nearby gate [Carr and Craighead, 1997], or using the irradiated rf-signal of an antenna [Hüttel et al., 2009b]. In general this method can be applied for both charged resonators and neutral ones, since the electric field induces a dipole moment which feels the electric force; in the case of, e.g., a semiconducting CNTs this nano-electro-mechanical system is charged for hole and electron conduction and neutral in the band gap.

In order to apply an rf-signal in a cryogenic measurement setup in a cryostat a high frequency line, in practice a coaxial cable, is installed. It terminates in an antenna without any direct contact to the sample itself. Since there is no thermal connection between antenna and the sample, this setup does not require a careful thermalization of the rf-line.

Figure 6.3 shows an ad-hoc setup, where a high frequency coaxial cable is mounted from room temperature down to the sample stage. Its lowest part, with a removed outer shielding forms a simple antenna, which is placed about one centimeter above the suspended carbon nanotube. The setup follows [Hüttel et al., 2009b].

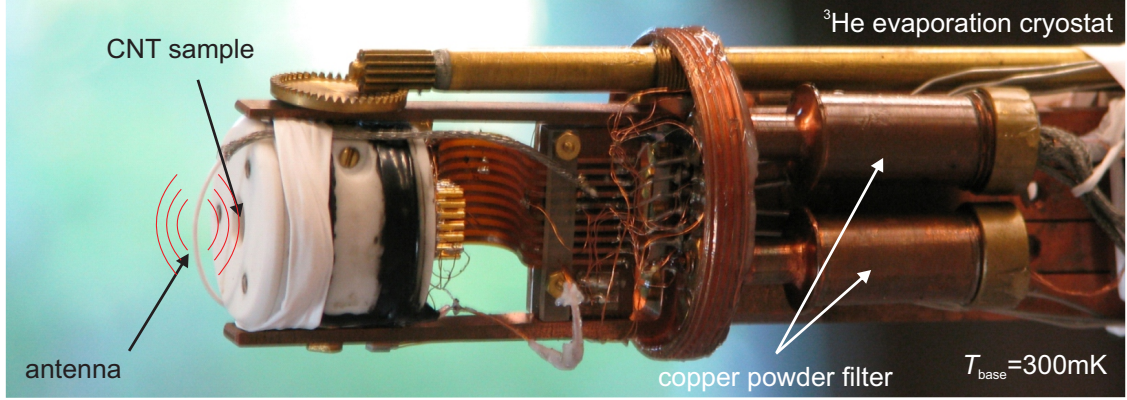


Figure 6.3: Photograph of the sample holder as lowest part in the ^3He evaporation cryostat with installed antenna for rf-signal irradiation.

6.1.2 Continuum mechanics of the transversal bending mode in carbon nanotubes

A suspended CNT can be modeled as a cylindrical beam using the Euler-Bernoulli beam equation [Cleland, 2003], namely

$$\rho A \frac{\partial^2 u}{\partial t^2} + EI \frac{\partial^4 u}{\partial x^4} - T \frac{\partial^2 u}{\partial x^2} = F(x, t), \quad (6.1)$$

where A is the cross-section area, ρ is the mass density, E is the Young's modulus, and I is the torque of inertia. The mechanical tension in the nanotube is expressed by T , and $u(x, t)$ is the deflection at position x along the CNT and time t . The function $F(x, t)$ denotes an external driving force. The damping term has been neglected for simplicity. The first term in Eq. 6.1 represents the acceleration, while the restoring force stems from two contributions: the bending stiffness is proportional to the fourth order derivative of the displacement $u(x)$ with respect to x and proportional to the so-called bending rigidity EI , while the tension depends on the second derivative $\partial^2 u / \partial x^2$. If the bending rigidity of the cylindrical beam is dominating and the tension can be neglected, the resonator behaves as a beam resonator. In the opposite case the CNT is in the limit of a string resonator with a dominating tension term. If one considers a doubly clamped beam with boundary conditions

$$\begin{aligned} u(0, t) &= 0, \\ u(L, t) &= 0, \\ du/dx(0, t) &= 0, \\ du/dx(L, t) &= 0, \end{aligned} \quad (6.2)$$

one obtains the characteristic behavior of the resonator's eigenfrequencies f_n in these two limits.

In the case of a beam resonator the eigenfrequencies are given by

$$f_n = \sqrt{EI/\rho A} \cdot \beta_n^2 / (2\pi L^2) \propto L^{-2}, \quad (6.3)$$

with β_n being the solutions of the equation $\cos(\beta_n) \cosh(\beta_n) = 1$. In contrast, for the string resonator one obtains

$$f_n = \sqrt{T/\rho A} \cdot (n+1)/2L, \quad (6.4)$$

with a sinusoidal mode shapes $\xi_n(x) = \sqrt{2} \sin((n+1)\pi x/l)$ of the fundamental mode ($n=0$) and the higher harmonics ($n=1, 2, \dots$).

Considering the beam resonator in absence of an external force and in the limit of small deflections ($\partial u/\partial x \ll 1$) in the static case, the mechanical tension T_{dc} is given by

$$T_{dc} \simeq T_0 \int_0^L \left[\frac{du_{dc}(x, T_{dc})}{dx} \right]^2 dx, \quad (6.5)$$

with the so-called residual tension $T_0 = EA \cdot (L - L_0)/L_0$ (mechanical tension without additional external force which deflects the resonator). This residual tension stems from the clamping of both ends of the resonator during the fabrication process. It can be positive (resonator is extended) or negative (resonator is compressed), and is proportional to the relative resonator's length deviation from the equilibrium value L_0 . In the case of strong negative residual tension the beam will buckle. For further details it is referred to [Poot and van der Zant, 2012].

6.1.3 Detection mechanism via dc-current measurement through an embedded quantum dot

Figure 6.4(a) displays a schematic drawing of the measurement setup. It is a direct extension of the dc-setup used in the electronic spectroscopy measurements (Sec. 3.3, Fig. 3.9(a)). A dc-bias voltage is applied via a voltage divider (1/1000) to the source contact and the current at the drain electrode is amplified in a current-to-voltage amplifier and measured with a multimeter. Additionally, for the aforementioned electrostatic excitation of the CNT vibration, an antenna is placed close to the sample and connected to a continuous wave generator.

A suspended CNT forms a mutual capacitance C_g with the gate electrode. This can be modeled with a simplifying picture of a wire placed above a conducting plate.

The capacitance depends on the distance $h(x)$ of the CNT resonator to the back gate electrode. Thus the capacitance for an infinitesimal small segment dL of the CNT is approximated by

$$c_g(x) = \frac{2\pi\epsilon_0}{\ln\left[\frac{2h(x)}{r}\right]},$$

where r is the radius of the CNT. The distance $h(x) = h_0 + u(x)$ of the CNT segment to the gate plane is altered by an oscillation amplitude $u(x)$ from the equilibrium position h_0 along the nanotube (see Fig. 6.4(b) and [Witkamp et al., 2006], [Sapmaz et al., 2003]). The integral over the CNT length L gives the total gate capacitance

$$C_g = \int_0^L c_g(x) dx.$$

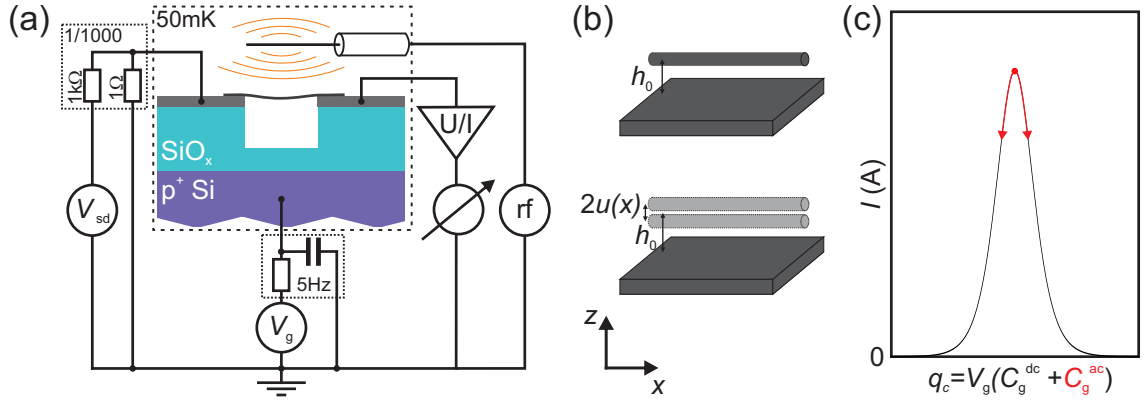


Figure 6.4: (a) Sketch of the motion detection setup where an rf-signal is irradiated from an antenna above the suspended CNT. An applied dc-bias voltage V_{sd} enables the detection of variations in the dc-current. (b) Simplified geometry of a wire placed above a conducting plate, as approximation for the gate capacitance of the CNT per unit length. (c) Underlying rectification effect in the Coulomb blockade regime. The motion of the CNT resonator leads to an alternating gate capacitance C_g^{ac} . Since the conductance of a quantum dot depends on $q_c = C_g V_g$, an ac-gate capacitance induces an averaged variation in the dc-current I at fixed bias voltage V_{sd} .

The conductance through the CNT QD is a function of the control charge $q_c = C_g V_g$, which is the product of gate capacitance C_g and gate voltage V_g . By driving the CNT resonator by an external ac-force, a finite amplitude $u(x)$ adds up an ac-component to the static gate capacitance $C_g = C_g^{dc} + C_g^{ac}$ [Hüttel et al., 2008]. In the case of resonance the CNT oscillation shows a large amplitude causing a large ac-gate capacitance C_g^{ac} . This modulates the current (conductance) through (of) the QD.

Since our setup, including the twisted pair wires in the cryostat, has large stray capacitances, the measurement has a very small low-pass cut-off frequency. The consequence is a time averaging over the ac-component of the current, which is some hundreds of MHz. Thus, only time-averaged currents are detected. Neglecting Taylor terms higher than second order one finds that in the case of resonance the change in the current ΔI depends on the curvature of $G(V_g)$ or $I(V_g)$, i.e. $\Delta I \propto \partial^2 I / \partial V_g^2$ [Hüttel et al., 2009b].

Fixing V_g at a peak of the Coulomb oscillation, as in Fig. 6.4(c), this averaging leads to a decrease of the dc-current, while fixing V_g at the flanks causes a peak in the frequency trace $I(f)$. Figure 6.5(a) shows such frequency traces for different driving powers P_{rf} . The symmetric peak of Lorentzian shape evolves into a highly non-linear peak at higher driving powers, which can be explained by a non-linear Duffing force term [Lifshitz and Cross, 2008], [Hüttel et al., 2009b]. The frequency trace at the lowest power $P_{\text{rf}} = -35$ dBm is fitted in Fig. 6.5(b) with a Lorentzian curve to extract the Q -factor to be $Q = 6800$. This is quite low for ultra-clean CNT resonators compared with [Steele et al., 2009], can however here be attributed to the relative high sample temperature $T = 300$ mK.

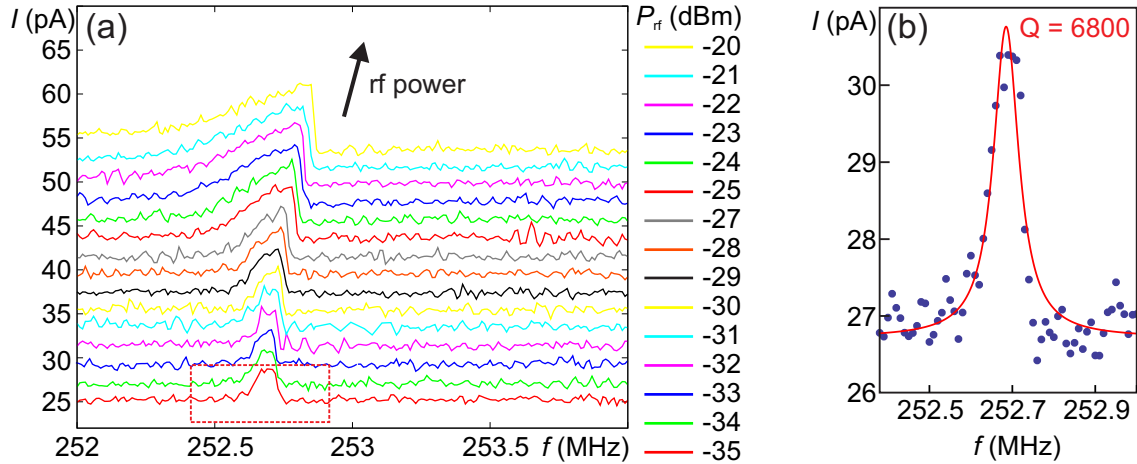


Figure 6.5: (a) Frequency dependence of the dc-current through the quantum dot on the suspended CNT at different driving powers P_{rf} . The symmetric resonance curve for low driving power evolves into a highly non-linear peak according to a Duffing resonator. The traces are shifted for clarity. (b) Single $I(f)$ curve at the lowest driving power ($P_{\text{rf}} = -35$ dBm) is fitted with a Lorentzian curve yielding a quality factor $Q = 6800$. *Cool down 1.*

6.1.4 Dependence of resonance frequency on quantum dot charging

In this section a constant mechanical tension T_{dc} and a small deflection u of the CNT is assumed, which is justified within a small gate voltage range.

Following electrostatics textbooks in a straightforward way, one can derive the change in the resonance frequency $\Delta\omega_0 = 2\pi\Delta f_0$ of the transversal vibration of a doubly clamped CNT resonator [Meerwaldt et al., 2012].

The electrostatic force F on the nanotube is approximated as the first derivative of the electrostatic energy W :

$$F(z, V_g) = \frac{\partial W}{\partial z} = \frac{1}{2} \frac{dC_g}{dz} (V_g - V_{CNT})^2.$$

For the electrostatic contribution of the spring constant one obtains:

$$k(z, V_g) = -\frac{dF(z, V_g)}{dz} = -\frac{\partial F(z, V_g)}{\partial z} - \frac{dC_g}{dz} \frac{dq_c}{dC_g} \frac{dV_g}{dq_c} \frac{\partial F(z, V_g)}{\partial V_g}. \quad (6.6)$$

Following [Meerwaldt et al., 2012], the first term on the right side of Eq. 6.6 can be neglected,¹ which induces a softening spring effect caused by the capacitive force between CNT and gate electrode. Hence, the change in the spring constant is given by

$$\Delta k(z, V_g) = -\frac{V_g(V_g - V_{CNT})}{C_g} \left(\frac{dC_g}{dz} \right)^2 \frac{\partial(V_g - V_{CNT})}{\partial V_g}. \quad (6.7)$$

If one assumes a harmonic oscillator (fulfilled in the linear response regime, i.e. for low driving power), it is valid to relate $\Delta\omega_0$ linearly to this change in the spring constant:

$$\Delta\omega_0 = \frac{\Delta k}{2m\omega_0}, \quad (6.8)$$

where m is the mass of the resonator and ω_0 is the resonance frequency. With the potential of the quantum dot, given by

$$V_{CNT} = q_c - e \langle N \rangle / C_\Sigma,$$

where $q_c = C_g V_g$ and $\langle N \rangle$ is the average charge occupation of the QD, one obtains

$$\Delta\omega_0 = \frac{V_g(V_g - V_{CNT})}{2m\omega_0 C_\Sigma} \left(\frac{dC_g}{dz} \right)^2 \left(1 - \frac{C_\Sigma}{C_g} - \frac{e}{C_g} \frac{\partial \langle N \rangle}{\partial V_g} \right). \quad (6.9)$$

¹Within a small range of the gate voltage the change of the CNT deflection is approximately zero.

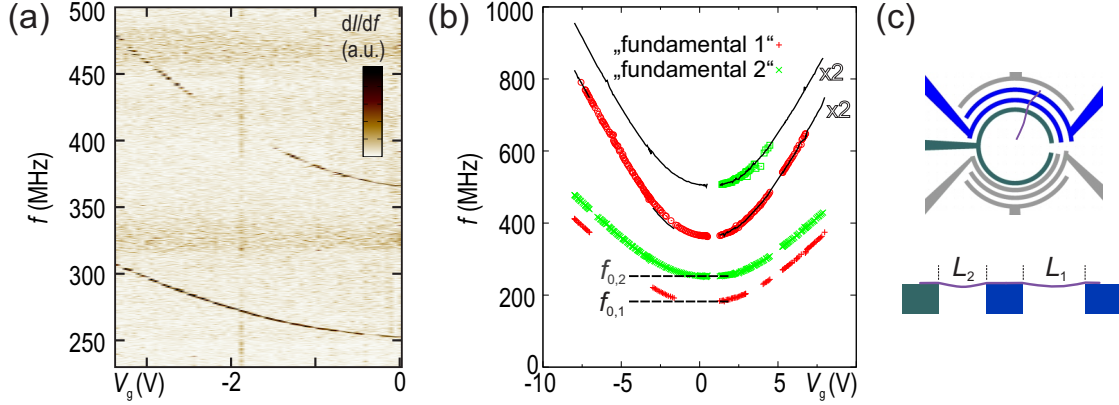


Figure 6.6: (a) Numerical derivative $dI/df(V_g, f)$ of the current depending on the gate voltage and the driving frequency. Sharp peaks or dips are observed at resonance frequencies of transversal bending modes. *Cool down 1.* (b) Extracted peak or dip positions from measurements as the exemplary one in (a) show strong and symmetric dependence of the resonance frequency on the gate voltage. The black solid lines correspond to exactly twice the resonance frequency of the two lower "fundamental" curves with a respective minimum of the resonance frequencies at $f_{0,1} \simeq 182$ MHz and $f_{0,2} \simeq 253$ MHz. (c) Sketch of the sample geometry with a CNT lying over two adjacent trenches with widths $L_1 = 700$ nm and $L_2 = 600$ nm.

Figure 6.6(a) shows an exemplary measurement of the gate dependence of the mechanical resonance frequency. Here the dc-current is measured versus gate voltage V_g and driving frequency f and numerically differentiated with respect to f to highlight the sharp peaks and dips. Note, that the step size in V_g is much larger than the Coulomb oscillation period.

In Fig. 6.6(b) the extracted resonance frequencies are plotted as function of the applied gate voltage. We identify two "fundamental" resonances with slightly different resonance frequencies $f_{0,1}$ and $f_{0,2}$, plus additional two resonances at exactly two times the fundamental ones. This is indicated by the black lines, which are the calculated values of $2 \cdot f_{0,1}$ and $2 \cdot f_{0,2}$ for both fundamental resonances. The origin of the upper resonance curves is either the excitation of a higher harmonic of the mechanical vibration or the excitation by a different driving mechanism. We assume that only the latter case is possible because a higher resonance mode is not expected at exactly twice the fundamental mode over the whole gate voltage range. Namely, the condition for a harmonic spectrum is a small static deflection $u(x)$ and a large residual tension of the CNT resonator, i.e. $T_{dc} \simeq T_0 \gg 1$ [Poot, 2009]. Since this behavior is only valid at small gate voltages, one would expect a deviation from $2 \cdot f_0$ at least over a large gate voltage range.

Rather we assume that also the ground mode is driven at its resonance frequency f_0 but here induced by parametric amplification at twice the resonance frequency $f = 2 \cdot f_0$ as has been seen also by [Eichler et al., 2011].

Further, the two fundamental resonances can be related to our sample geometry as shown in Fig. 6.6(c) where an overgrown CNT connects even three electrodes. The blue electrodes highlight the source and drain contact of the quantum dot and the suspended part examined in this thesis. The measurement to the green marked one has also shown electronical quantum dot and mechanical features but has not been investigated in more detail due to poor and irregular QD properties. The width of the trench measured in detail is $L_1 = 700$ nm while the neighboring one has a width of $L_2 = 600$ nm.

In the minimum of the curves in Fig. 6.6(b) at approximately zero tension in the limit of a beam resonator, a resonance frequency dependence of $f_0 \propto 1/L^2$ is expected (see Section 6.1.2 and [Poot, 2009]). Indeed, the fundamental resonances show a ratio of $f_{0,2}/f_{0,1} \simeq 253 \text{ MHz}/182 \text{ MHz} \simeq 1.39$ which is in good agreement with the inverse square of the ratios of the two adjacent trench widths $(L_1/L_2)^2 = (700 \text{ nm}/600 \text{ nm})^2 \simeq 1.36$, as sketched in Fig. 6.6(c). Taking into account small misalignments from the radial orientation of the CNT to the circular electrodes and a finite residual tension T_0 , these two fundamental resonance can be attributed to the two segments spanning adjacent trenches. So far, however, it is not fully understood how the non-contacted nanotube part can non-locally induce a resonance signal. One idea is that the capacitively coupled charges on this segment change in resonance their distance to the QD on the contacted part, likewise causing an alternating control charge q_c which leads to a finite signal. Other possibilities include rectifying effects in the quantum dots.

On the single electron charging scale the last term in Eq. 6.9 is dominant, which is proportional to the change in the mean charge on the QD with respect to the gate voltage $\partial \langle N \rangle / \partial V_g$, thus causing a dip in $\Delta f_0 = \Delta \omega_0 / 2\pi$. This behavior can be seen in the dc-current measurement of Fig. 6.7(a). There the driving frequency is tuned over a small range for gate voltages spanning only two charge transitions around $N_{\text{el}} = 19$, while the driving power and bias voltage are kept constant at $P = -25 \text{ dBm}$ and $V_{\text{sd}} = 0.2 \text{ mV}$. For better visibility of the resonances in each vertical line the mean current \bar{I} of each $I(f)$ trace is subtracted. The resonance frequencies are extracted and plotted in Fig. 6.7(b) versus the gate voltage V_g . The change of the resonance frequency around the point of charge transition is well understood with Eq. 6.9. However, between adjacent Coulomb blockade regions, where the approximately linear contribution stems from the charging of the back gate, an additional stepwise increase of the resonance frequency appears, see the red lines in Fig. 6.7(b). As reported in the Supplementary Material of [Steele et al.,

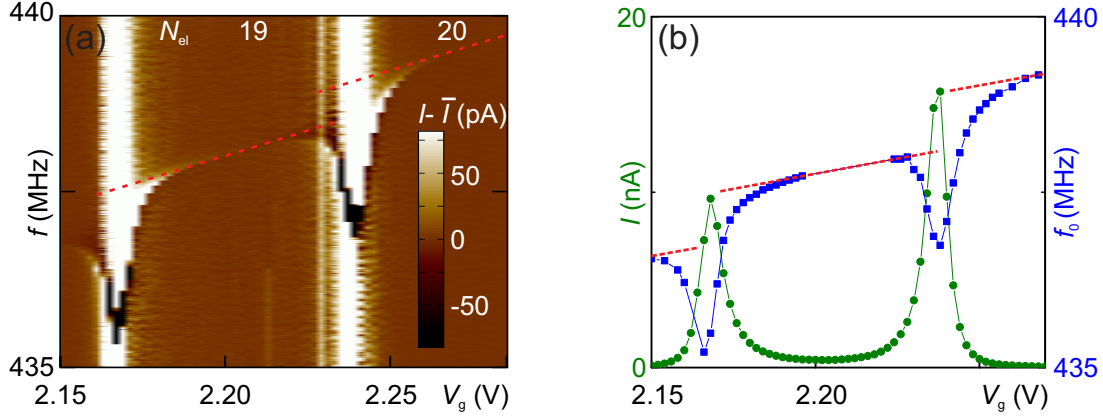


Figure 6.7: (a) Current deviation $I(f, V_g) - \bar{I}(V_g)$ as function of gate voltage V_g and driving frequency f . The linear behavior of $f_0(V_g)$ in the Coulomb blockade region is indicated by the red dashed lines. The nominal rf-power is $P_{\text{rf}} = -25$ dBm and the bias voltage is $V_{\text{sd}} = 0.2$ mV. (b) *Blue*: Extracted resonance frequency f_0 from (a). The indicated red lines highlight the steps in the resonance frequency for the transitions between different number of charges on the QD which takes place in discrete steps, see text. *Green*: Current trace $I(V_g)$ at $V_{\text{sd}} = 0.2$ mV. The Coulomb blockade oscillations coincide with charge transitions indicated by the dips in $f_0(V_g)$. *Cool down 2*.

2009], these stem from the discrete single electron charging of the QD at transitions $N \rightarrow N + 1$ leading to steps in f_0 . Focusing on the dips in $f_0(V_g)$ in Fig. 6.7(b) one observes a coincidence with the Coulomb peaks in the current trace (green curve) which indicate the resonance condition of a QD level with the Fermi level of the leads. This is in good agreement with the electrostatic theory in the Coulomb blockade dominated transport regime.

By increasing the bias voltage, the charge transition $\langle N \rangle(V_g)$ smears out leading to a broadening of the dip [Steele et al., 2009]. If the bias voltage exceeds the level broadening $\hbar\Gamma$ two dips evolve in $f_0(V_g)$. This can be understood by having a look at the charging state in Fig. 6.8 from [Meerwaldt et al., 2012], where a plateau is formed at one half additional charge if the bias voltage is sufficient high and the tunnel rates are low enough and equal for both barriers.

The ultra-clean sample allows us to trace the resonance down to the neutral state. In Fig. 6.9 the numerical derivative of the current with respect to the frequency dI/df is plotted in dependence on the gate voltage V_g . Although the current is very low approaching the detection limit of the mechanical resonance one can see the expected dips at the points of charge transitions and the overall decrease of the resonance frequency with decreasing gate voltage. Going to the hole conducting side

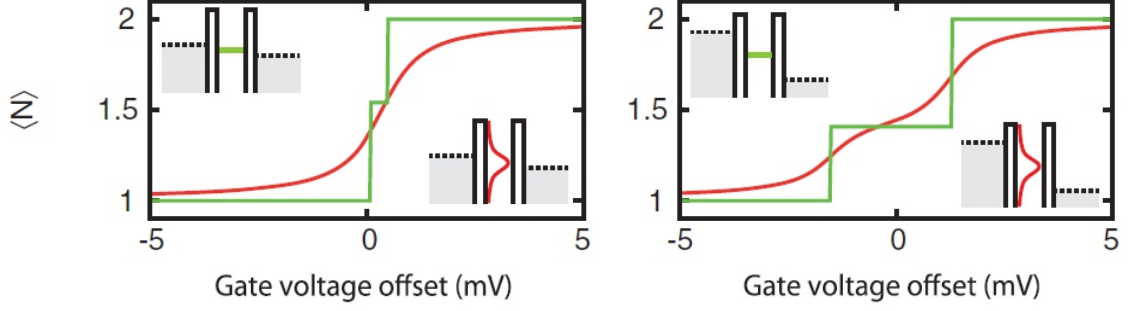


Figure 6.8: Behavior of $f_0(V_g)$ for both low (left) and high (right) bias voltages V_{sd} and low (green) and high (red) tunnel rates Γ . The inserts sketch the QD levels coupled to the Fermi sea of the leads. Taken from [Meerwaldt et al., 2012].

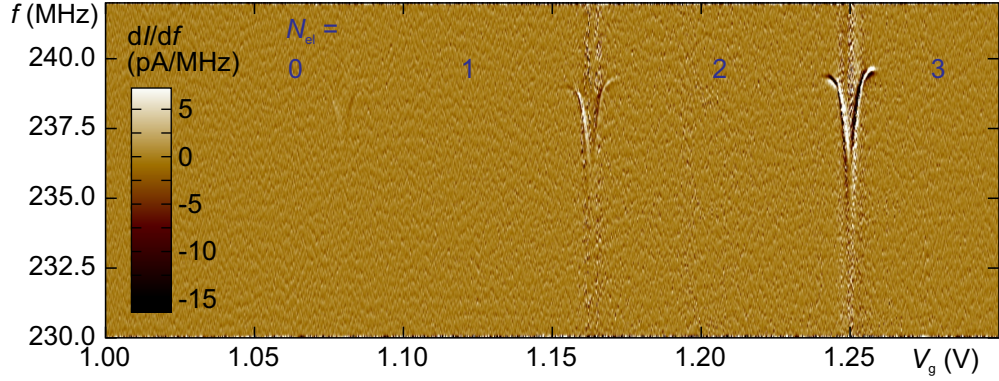


Figure 6.9: Gate dependence of resonance frequency in the few electron regime $0 \leq N_{el} \leq 3$ at fixed $V_{sd} = 1$ mV and $P_{rf} = -15$ dBm. *Cool down 1.*

there is a quite different picture, since the conductance of the QD is much higher (see Sec. 3.3). The system first shows Coulomb oscillations resulting from the discrete charging. These evolve into a Fabry-Pérot pattern² indicating an open system with no charge quantization on the dot, as displayed by the overlying gate trace in Fig. 6.10(a). The gate dependence of the resonance frequency f_0 now exactly reflects this transition, namely from a closed to an open system. For better visibility in Fig. 6.10(b) the same measurement is plotted with a highlighted resonance curve and a parabola (green dashed line) representing the gate charging effect on f_0 .³ Clearly visible are broad dips at the charge transitions of the first holes broadening

²The Fabry-Pérot pattern is better visible on the larger gate voltage scale, e.g. in Fig. 3.11.

³This is only valid if a constant mechanical tension T_{dc} is assumed on this gate voltage range.

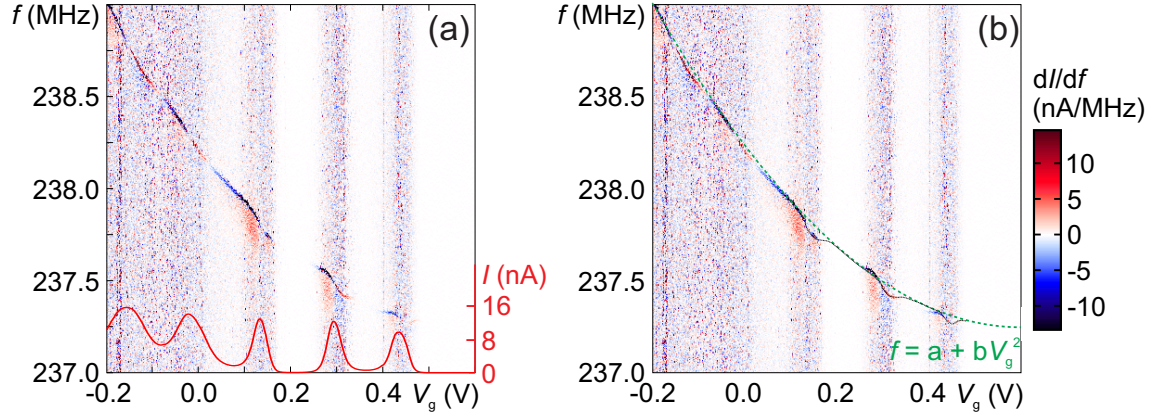


Figure 6.10: (a) Gate dependence of the resonance frequency in few holes regime at rf-power $P_{\text{rf}} = -29$ dBm including numerical derivative with respect to the y-axis for better visibility of the resonance frequency. The overlying gate trace $I(V_g)$ shows Coulomb blockade oscillations evolving into a Fabry-Pérot pattern. The bias voltage is fixed to $V_{\text{sd}} = 0.2$ mV and $T = 30$ mK. (b) Same plot as in (a) with indicated parabola (green dashed line) and highlighted resonance curve (black dotted line). *Cool down 2.*

for higher hole numbers until they finally nearly vanish due to the lack of charge quantization of the quantum dot. In Eq. 6.9 this can be explained by an increase of the coupling Γ leading to a smooth $\langle N \rangle(V_g)$ curve.

In this section it has been shown that beyond an electronic model system ultra-clean CNTs also provide a well controllable mechanical system, where one can trace the mechanical resonance over a wide range from the band gap and the first charges on a very decoupled QD via Kondo-enhanced transport to a Fabry-Pérot conductance regime. In the following, the effect of magnetic fields on the Q -factor of the mechanical resonator is shown. Further it is demonstrated how the Kondo effect relates to the charging of the nanotube quantum dot, which is detected via the mechanical resonance. In Sec. 6.4 it is shown how current discontinuities, induced by a dc-current driven self-oscillation of the CNT, is used to estimate its motion amplitude.

6.2 Magnetic damping of a driven CNT resonator

This section demonstrates the quantitative analysis of the damping of the transversal CNT vibration in an external magnetic field. The examination of this effect is based on the observation that mechanical instabilities, caused by strong feedback of the tunnel current on the oscillator, can be reduced by magnetic fields. The main results of this work have been published in *New Journal of Physics* [Schmid et al., 2012].

A dilution refrigerator system is used to cool the sample to $T = 30$ mK. Measuring the conductance depending on the gate and bias voltage $dI/dV_{sd}(V_g, V_{sd})$ in Fig. 6.11 shows Coulomb diamonds, where the number of charges on the quantum dot is fixed. Since we are in the higher electron number regime ($N_{el} \simeq 40$), where the overall conductance is already increased by higher-order tunneling processes, the Coulomb diamonds are smeared out. Due to the strong coupling to the leads the Kondo effect arises at sufficiently low temperatures, as discussed in Chapter 4. Indeed, clearly visible in the transport spectroscopy measurement is the Kondo enhanced zero-bias conductance peak for odd electron numbers (see black squares in Fig. 6.11). Additionally, a narrow line of low conductance around $V_{sd} = 0$ appears (black arrows), indicating the energy gap in the density of states of the superconducting rhenium electrodes.

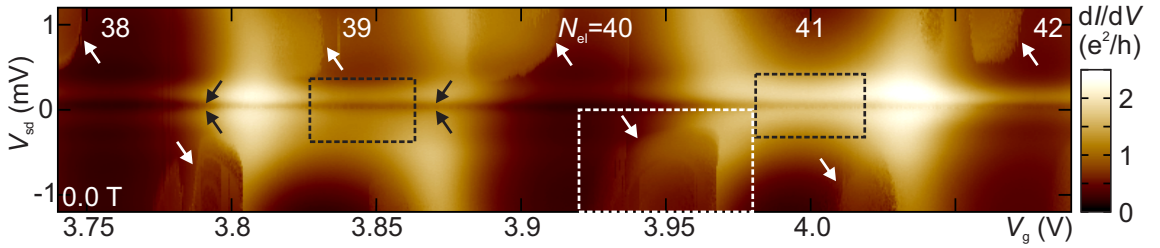


Figure 6.11: Conductance as function of gate and bias voltage $dI/dV_{sd}(V_g, V_{sd})$ for electron numbers around $N_{el} = 40$. The narrow line around $V_{sd} = 0$ (black arrows) is due to superconductivity in the leads; the Kondo effect causes zero-bias enhanced conductance for odd electron numbers on the QD (black dashed squares). The discontinuities in the conductance, marked with white arrows, are explained by a dc-current induced self-excitation of the transversal vibration, see text. *Cool down 2.*

However, most striking are the regions where the conductance exhibits sharp steps, marked with white arrows in Fig. 6.11. Excited electronical states can be excluded as origin of this phenomenon since the observed shape completely differs from the theoretical predictions (see Chapter 3.3). We recall the sample structure, where the

CNT is suspended between two electrodes enabling mechanical vibration in the vacuum environment, and compare the features with published results from a nearly identical setup of [Steele et al., 2009]. They have seen similar features and assumed mechanical effects as origin for the sharp features in the stability diagram. To confirm this assumption we can compare our measurement in Fig. 6.11, done in a dilution cryostat with evacuated sample stage, with another measurement (*cool down 3*) where the suspended CNT is immersed into liquid $^3\text{He}/^4\text{He}$ -mixture. The immersion induces a strong damping of the transversal bending mode and quenches the mechanical effects in the transport measurements. Indeed, in Fig. 6.12 the dominant sharp steps in the stability diagram vanish and only the electronic features remain nearly unchanged.

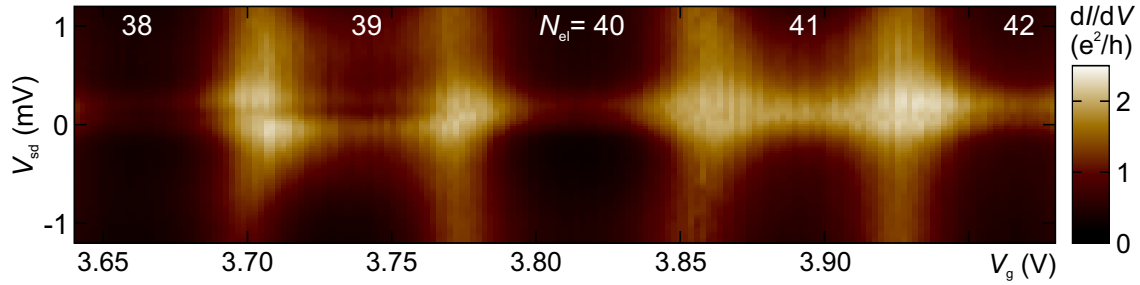


Figure 6.12: Conductance as function of gate and bias voltage $dI/dV_{sd}(V_g, V_{sd})$ in the same parameter region as in the measurement shown in Fig. 6.11, but now with the suspended CNT sample immersed into liquid $^3\text{He}/^4\text{He}$ -mixture. *Cool down 3*.

In their theoretical work, [Usmani et al., 2007] have investigated a single electron tunneling device weakly coupled to an under-damped oscillator. They have shown that strong feedback of the electron tunnel events on the mechanical system can generate mechanical oscillations, which in turn strongly modify the current through the quantum dot. They model the system by an oscillating conducting island coupled to two leads enabling sequential tunneling through the island. This corresponds to our sample structure, where the suspended CNT in vacuum provides the mechanical oscillatory degree of freedom with low damp-

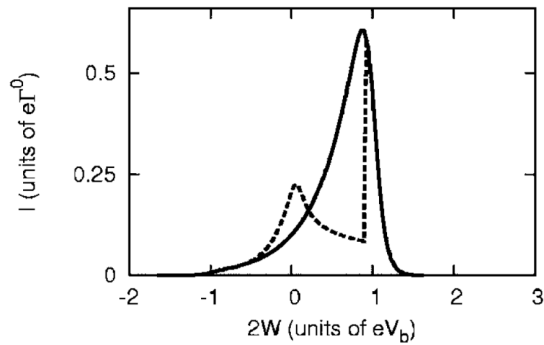


Figure 6.13: Current modification in the strong feedback regime. The x -axis is in units of the bias voltage $W = eV_{sd}$. Adapted from [Usmani et al., 2007].

ing. The requirement for strong feedback is high conductance and a high quality factor of the resonator. An example of the calculated bias voltage dependence of the current for strong feedback of the mechanical oscillation on the single electron tunneling is shown in Fig. 6.13. It also shows a sharp discontinuity as seen in our experiment.

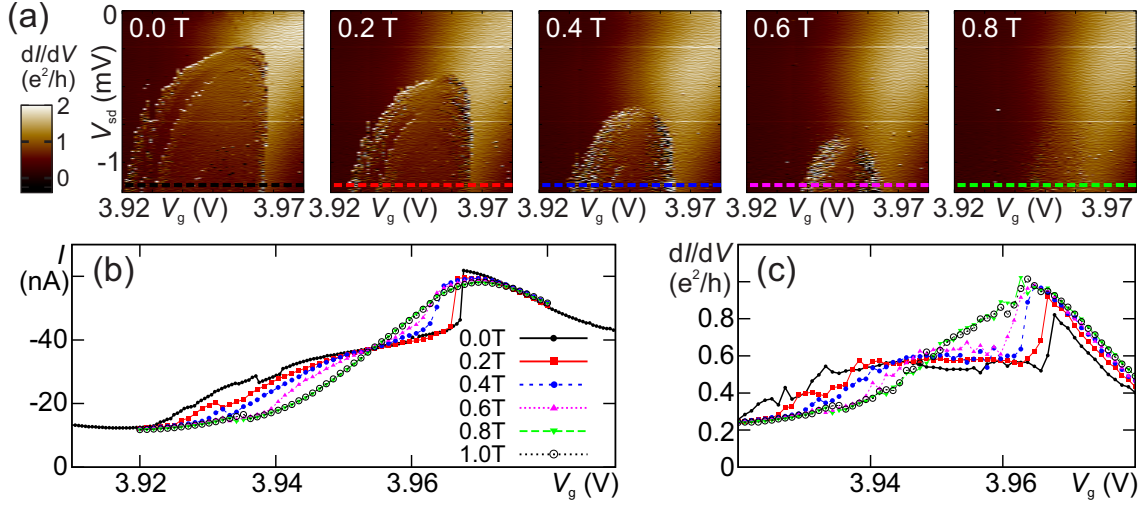


Figure 6.14: (a) The numerical derivative of $I(V_g, V_{sd})$ in the self-excitation area marked in Fig. 6.11, in dependence on an external magnetic field perpendicular to the sample substrate. A shrinking of the areas with instabilities in the conductance is observed. Current (b) and conductances (c) traces at fixed V_{sd} , see colored dashed line in (a). While at low field sharp steps appear in $I(V_g)$ and $dI/dV_{sd}(V_g)$, a smooth curve is observed at higher fields. *Cool down 2.*

In Figure 6.14 we focus on one region where self-excitation occurs (white dashed square in Fig. 6.11) and apply a magnetic field which is perpendicular to the CNT axis and thus perpendicular to the vibration plane of the transversal mode. Note that in order to increase the contrast the numerical derivative of the current through the QD with respect to the bias voltage is plotted. Increasing the magnetic field strength leads to a shrinking of the instability region. Already at 0.8 T, the plotted parameter region does not display any instability anymore. We take a closer look on the current or conductance traces in the Figs. 6.14(b),(c) at fixed bias voltage $V_{sd} = -1.15$ mV, as marked in Fig. 6.14(a) by the colored dashed lines. According to Usmani et al. the self-excitation can be suppressed either by a lowering of the tunneling rate, i.e. the quantum dot conductance, or by a decrease of the effective quality factor of the resonator. Both current and conductance show a weak dependence on the magnetic field outside the instability region. This leads us to conclude that an external magnetic field B induces damping of the oscillation, i.e. a decrease of the

quality factor Q of the resonator.

In order to investigate the Q -factor one has to drive the resonator and measure the frequency dependence of the dc-current. The Q -factor can be extracted from the FWHM (Full Width at Half Maximum) of the Lorentzian resonance curve at different magnetic fields B . To suppress noise-induced fluctuations in the observed linewidth this measurement has been done for many driving powers P_{rf} at each magnetic field value. The Q -factor was extracted by taking the mean value of the linewidth at sufficiently low P_{rf} to guarantee a linear response of the mechanical system on the external driving force. Indeed, as the example of Fig. 6.16(a) shows, the resonance curve broadens accompanied by a decrease of the Q -factor for higher fields. Plotting the quality factor versus the external magnetic field (data points in Fig. 6.16(b)) again shows this decrease of the Q -factor with increasing field.

To model this behavior a simple electronic equivalent circuit is used, depicted in Fig. 6.15(b), where the vibrating CNT acts as a wire, which modulates the magnetic flux when oscillating leading to an induced voltage between both contacts $U_{\text{ind}} \propto B$. The source and drain electrode are assumed to be capacitively short circuited at frequencies of hundreds of MHz, since there is a large capacitances $C \simeq 1$ pF of the bond pads to the silicon substrate due to the relatively large areas $(150 \times 100) \mu\text{m}^2$ and small distances (300 nm). As a result, eddy currents are induced. We assume an Ohmic serial resistance which leads to a power dissipation $P \propto B^2$.

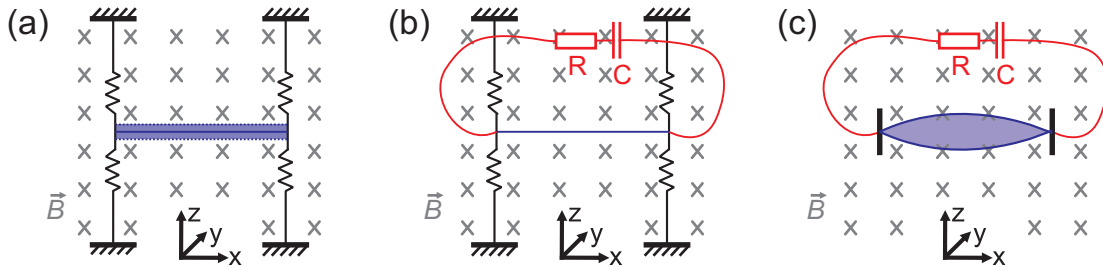


Figure 6.15: (a) The vibrating CNT is modeled as an oscillating conducting rod in an external B -field perpendicular to the vibration plane. (b) The electrical environment can be approximated by an Ohmic resistance and a large capacitance in series. (c) In a more realistic scheme the CNT deflection follows a sinusoidal envelope.

In a simplified picture (see Figs. 6.15(a),(b)) our CNT is represented by a conducting rod of length L attached to springs on both ends, which are connected via an Ohmic resistance R . The magnetic field B is aligned to the y -axis and the vibration $z(t)$ is in z -direction. Then the induced voltage between both ends of the rod is

$$U_{\text{ind}} = \frac{d\Phi(t)}{dt} = B \frac{dA(t)}{dt} = BL \frac{dz(t)}{dt} = BL\dot{z}, \quad (6.10)$$

where \dot{z} is the time derivative of the deflection.

Thus, if the vibrating CNT is short-circuited over an Ohmic resistance R (see Fig. 6.15(b)), there is an average energy dissipation per oscillation given by

$$\langle P \rangle = \left\langle \frac{dE}{dt} \right\rangle = \frac{\langle U^2 \rangle}{R} = \frac{L^2}{R} \cdot \langle \dot{z}^2 \rangle \cdot B^2. \quad (6.11)$$

The total energy of the system is given by the kinetic energy of the rod, for $\dot{z}(z = 0) \equiv \dot{z}_0$ maximal,

$$E(t) = \frac{1}{2} m \cdot \dot{z}_0^2. \quad (6.12)$$

With the mean value $\langle \dot{z}^2 \rangle = \frac{\dot{z}_0^2}{\sqrt{2}}$ for harmonic oscillations the total energy is given by

$$E(t) = \frac{1}{\sqrt{2}} m \cdot \langle \dot{z}^2 \rangle. \quad (6.13)$$

Solving Eq. 6.13 for $\langle \dot{z}^2 \rangle$ to replace it in Eq. 6.11 yields a differential equation for the total energy in the system:

$$\dot{E}(t) = -\frac{\sqrt{2} \cdot L^2}{R \cdot m} \cdot B^2 \cdot E, \quad (6.14)$$

which is solved by

$$E(t) = C \cdot e^{-\frac{\sqrt{2} \cdot L^2}{R \cdot m} B^2 \cdot t} = C \cdot e^{-\frac{1}{\tau} \cdot t} \quad (6.15)$$

with an integration constant C and the time constant

$$\tau = \frac{R \cdot m}{\sqrt{2} \cdot L^2} \cdot \frac{1}{B^2}. \quad (6.16)$$

The time constant τ is connected with the quality factor by $Q = \sqrt{\frac{k}{m}} \cdot \frac{\tau}{2}$, and thus

$$Q_B = \frac{\sqrt{k \cdot m} \cdot R}{2\sqrt{2} \cdot L^2} \cdot \frac{1}{B^2} = \frac{\omega_0 \cdot m \cdot R}{2\sqrt{2} \cdot L^2} \cdot \frac{1}{B^2}. \quad (6.17)$$

The total damping is the combination of the intrinsic damping of the system, expressed by Q_i , and the damping resulting from the motion in a magnetic field (Eq. 6.17). Since parallel and independent relaxation mechanisms are assumed one can apply Matthiessen's rule, whereupon the total Q -factor is given by

$$\frac{1}{Q} = \frac{1}{Q_i} + \frac{1}{Q_B}. \quad (6.18)$$

With $P_1 = \frac{\sqrt{k \cdot m} \cdot R}{2\sqrt{2} \cdot L^2}$ one obtains

$$\frac{1}{Q} = \frac{1}{Q_i} + \frac{B^2}{P_1} = \frac{P_1 + Q_i \cdot B^2}{P_1 \cdot Q_i}$$

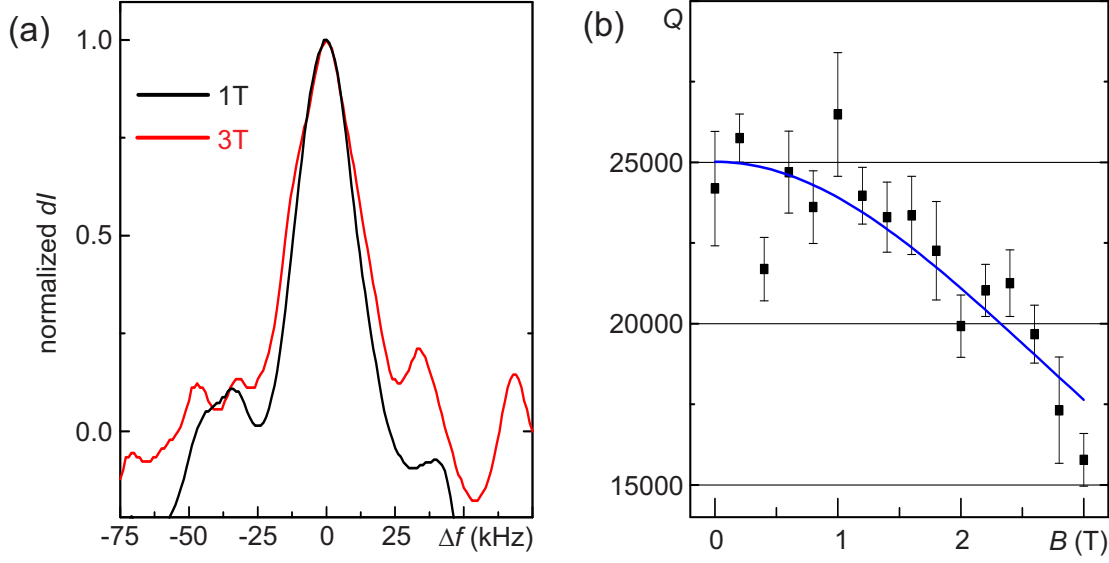


Figure 6.16: (a) Exemplary resonance curves with normalized change of the current dI for finite amplitude plotted versus frequency difference from the resonance frequency f_0 . (b) Quality factors Q extracted from the full width at half maximum (FWHM) of the frequency traces like in (a) for several rf-power values versus perpendicular magnetic field B . *Cool down 2*.

$$\Rightarrow Q = \frac{P_1 \cdot Q_i}{P_1 + Q_i \cdot B^2}. \quad (6.19)$$

Using Eq. 6.19 one can extract from fit of the experimental data (Fig. 6.16(b)) an intrinsic quality factor

$$Q_i = (2.5 \pm 0.061) \cdot 10^4$$

and a prefactor

$$P_1 = \frac{\omega_0 \cdot m \cdot R}{2\sqrt{2} \cdot L^2} = (5 \pm 0.9) \cdot 10^5 \text{ T}^{-2}$$

of Q_B (see Eq. 6.17) with good agreement despite several simplifications.

With an estimated resonator length $L = 700 \text{ nm}$, angular frequency $\omega_0 = 2\pi \cdot 490 \text{ MHz}$, and an estimated mass of the suspended CNT segment $m = 1.3 \cdot 10^{-21} \text{ kg}$, a rough value for the Ohmic resistance R can be given:

$$R = \frac{2\sqrt{2} \cdot L^2 \cdot P_1}{\omega_0 \cdot m} = \frac{2\sqrt{2} \cdot (7 \cdot 10^{-7})^2 \cdot 5 \cdot 10^5}{3.077 \cdot 10^9 \cdot 1.3 \cdot 10^{-21}} \Omega = 187 \text{ k}\Omega.$$

Additionally, in order to have an active power dissipation in the Ohmic resistor, the voltage drop at the Ohmic resistance R has to be much larger than the voltage drop

at the capacitive impedance $1/i\omega C$, i.e.

$$\frac{R}{\frac{1}{i\omega C}} = i\omega RC \gg 1.$$

The estimation of the lower limit of the capacitance responsible for the short circuit

$$C \gg \frac{1}{\omega_0 R} = \frac{1}{3.077 \cdot 10^9 \text{ s}^{-1} \cdot 1.87 \cdot 10^5 \Omega} = 1.7 \text{ fF}$$

is in fair agreement with the geometrically estimated capacitances between bond pads and substrate, which are in the order of $\approx 10^3$ fF.

The results from the mechanical damping of a nanomechanical resonator have been confirmed shortly afterwards in a strict quantum mechanical approach by Nocera et al., reproducing our data quantitatively very well (see Fig. 6.17). The system is modeled by a single electronic level coupled to the leads via tunnel rates Γ , while the mechanical degrees of freedom are approximated as quantum harmonic oscillator with resonance frequency ω_0 . The problem is solved in the adiabatic limit, i.e. $\omega_0/\Gamma \ll 1$.⁴ Nocera et al. find that a perpendicular magnetic field introduces an electronic tunneling phase depending on the resonator deflection. The resulting effective force is proportional to the magnetic field and to the electronic current. The damping is modified by quantum electronic current-current fluctuations corrections whose strength is quadratic in magnetic field. The slight increase of the theoretically obtained Q -factor for small fields (at 0.8 T, red curve in Fig. 6.17) is due to asymmetry introduced by an applied gate voltage [Nocera et al., 2013].

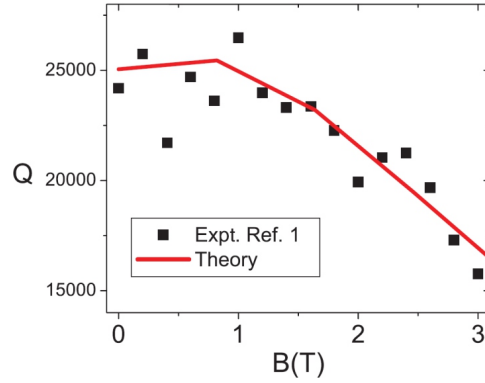


Figure 6.17: Theoretically proved magnetic field dependence of the Q -factor. Adapted from [Nocera et al., 2013].

⁴The adiabatic limit is justified in the intermediate coupling regime around $N_{\text{el}} = 40$. Here, a typical current of $I \simeq 10$ nA is measured, which corresponds to a lower limit of the tunnel rates of $\Gamma = 10 \text{ nA} / 1.6 \cdot 10^{-19} \text{ As} \simeq 60 \text{ GHz}$ in single electron tunneling.

6.3 Charge detection in the Kondo regime

As in Chapter 6.2, in the following we focus on high electron numbers around $N_{\text{el}} = 40$, where a strong Kondo effect is present for odd N_{el} . The data have been recorded in the same cool-down as these presented in Chapter 6.2. The gate dependence of the differential conductance from the neutral state in the band gap up to high electron numbers on the QD is plotted in Fig. 6.18. This allows us to identify the absolute number of electrons at a certain gate voltage.

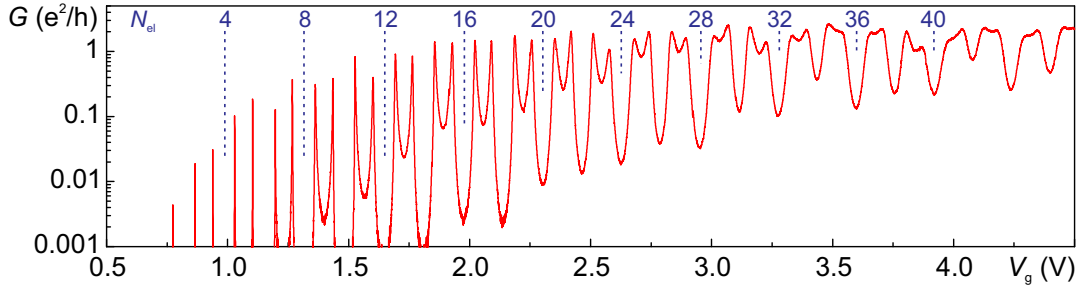


Figure 6.18: Logarithmic plot of the gate dependence of the differential conductance $G(V_g)$ at zero bias voltage over a large range of electron occupation numbers N_{el} . The temperature is $T = 50$ mK. *Cool down 2*.

As explained in Chapter 6.1.4 the resonance frequency ω_0 of the transversal bending mode depends on the gate voltage, especially around the charge transitions where $\partial \langle N \rangle / \partial V_g \neq 0$. This allows us to deduce the exact number of charges on the quantum dot $\langle N \rangle$ by modeling $f_0(V_g)$. Figure 6.19 shows the current in dependence on the rf-signal frequency f at fixed rf-power $P_{\text{rf}} = -25$ dBm and fixed gate voltage V_g . The mean value of each frequency trace $\bar{I}(V_g)$ is subtracted to highlight the small changes in the current $I(f, V_g)$ for the resonance case compared to the quite large modulation of the current by the gate voltage $I(V_g)$. The panel on the right side shows one exemplary frequency trace at fixed $V_g = 4.1$ V where a striking peak in the current at roughly $f \simeq 495$ MHz indicates the mechanical resonance frequency. The upper panel gives the gate dependence of the dc-current in the off-resonance case at an applied bias voltage $V_{\text{sd}} = 0.1$ mV showing the characteristic even-odd behavior in the Kondo dominated transport regime.

In Chapter 6.1.4 we have deduced the dependence of the resonance frequency f_0 on the gate voltage. Here we focus on the dependence on the change of the average number of charges on the quantum dot with respect to the gate voltage $\partial \langle N \rangle / \partial V_g$ and subtract the in first order linear contribution from the charging of the gate electrode. Plotting $[f_0 - \alpha V_g](V_g)$, in Fig. 6.20(a) two dips are clearly visible. By comparison with the measurement of the gate dependence of the differential conduc-

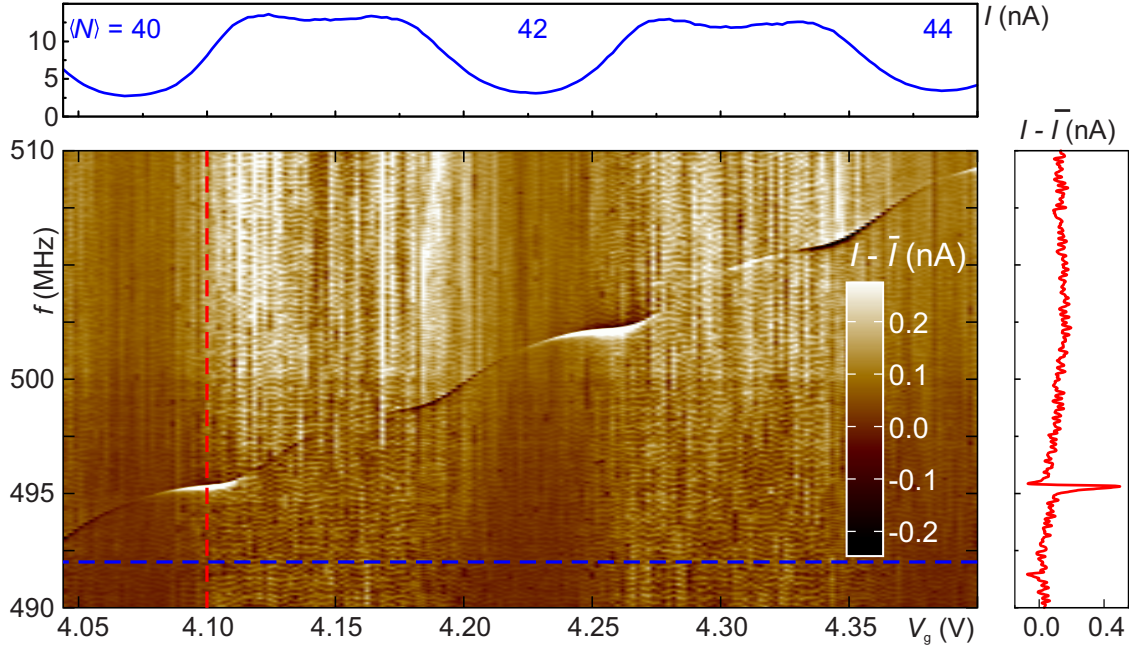


Figure 6.19: Main plot: Time-averaged current through the nanotube as function of the ac driving frequency f and the gate voltage V_g . The mean values of each frequency trace are subtracted to improve the contrast. The applied dc-bias voltage is $V_{sd} = 0.1$ mV and the rf-power is nominal $P_{rf} = -25$ dBm. Parameters are chosen such that $40 \leq N_{el} \leq 44$ in the regime of strong Kondo correlations. Upper panel: Gate dependence of the uncorrected off-resonance dc-current $I(V_g)$ (blue dashed line in the main plot) exhibiting high conductance at odd electron numbers as indication for the Kondo effect. Right panel: Frequency dependence of the corrected dc-current (where the mean current \bar{I} is subtracted as in the main plot); the resonance frequency f_0 is clearly visible as peak. *Cool down 2.*

tance in Fig. 6.18 one can identify the two charge transitions $N_{el} = 40 \rightarrow 41 \rightarrow 42$ at this gate voltage range. If we only restrict ourselves to these two charge transitions, following the work of [Meerwaldt et al., 2012], the quantum dot can be modeled as a two level system. Here the density of states (DoS) on the quantum dot is represented by two Lorentzian curves with finite line width taking into account the finite lifetime $\tau = 1/\Gamma$ caused by the tunnel rates Γ to source and drain contact. One level is represented by

$$DoS(\mu) = \frac{1}{2\pi} \frac{\hbar\Gamma}{(\mu - \mu_{CNT})^2 + (\hbar\Gamma/2)^2},$$

while the distance to the second one is given by the addition energy ΔE . Since in the co-tunneling regime at $N_{el} \simeq 40$ the lifetime broadening of the states strongly exceeds the temperature induced broadening at $T = 30$ mK in the dilution cryostat,

we can assume $T = 0$ and now the tunnel rate on and off the quantum dot to left and right electrode can be calculated by

$$\begin{aligned}\Gamma_L^+ &= \int_{-\infty}^{\mu_L} D o S(\mu) d\mu \quad , \quad \Gamma_R^+ = \int_{-\infty}^{\mu_R} D o S(\mu) d\mu , \\ \Gamma_L^- &= \int_{\mu_L}^{\infty} D o S(\mu) d\mu \quad , \quad \Gamma_R^- = \int_{\mu_R}^{\infty} D o S(\mu) d\mu .\end{aligned}\tag{6.20}$$

Approximating the average charge occupation by the tunnel rates via

$$\langle N \rangle = N_0 + \frac{\Gamma^+}{\Gamma^+ + \Gamma^-}\tag{6.21}$$

with $\Gamma^\pm = \Gamma_L^\pm + \Gamma_R^\pm$ one can reproduce the change in the resonance frequency spanning several charging states, as deduced in Sec. 6.1.4, by

$$\Delta\omega_0 = \frac{V_g(V_g - V_{\text{CNT}})}{2m\omega_0 C_\Sigma} \left(\frac{dC_g}{dx} \right)^2 \left(1 - \frac{C_\Sigma}{C_g} - \frac{e}{C_g} \frac{\partial \langle N \rangle}{\partial V_g} \right).\tag{6.22}$$

Figure 6.20(a) shows a very good fit (red curve) of the measured resonance frequency dependence on V_g using Eq. 6.22. The free parameters are the spacing of the two density of states maxima ΔE and the lifetime broadening $\hbar\Gamma$. The mass m of the resonator is estimated by a CNT with length $L = 700$ nm according to the sample geometry and diameter. The gate capacitance C_g and its derivative are approximated by the capacitor model of a wire above a conducting plate. The total QD capacitance C_{tot} can be determined from the measurements via the charging energy of the QD (see Fig. 3.12(b)).

Despite some simplifications done in the modeling of the system, we get an impressive agreement with the experimental data (Fig. 6.20(a)), which can be used now to recover the average number of charges $\langle N \rangle(V_g)$, plotted in Fig. 6.20(b).

If we assume pure single electron tunneling (SET) without any co-tunneling processes the current through the QD embedded on the resonator can be deduced from the master equation and is given by

$$I = \frac{\Gamma_L^+ \cdot \Gamma_R^- - \Gamma_R^+ \cdot \Gamma_L^-}{\Gamma^+ + \Gamma^-}.\tag{6.23}$$

Using the fit parameters $\Delta E, \Gamma$ from the fit in Fig. 6.20(a) and the Eqs. 6.20, 6.23 the resulting SET current can be calculated and is plotted in Fig. 6.20(c) as red curve together with the measured gate trace $I(V_g)$ (data points).

The SET current maxima exactly coincide with the dips of the resonance frequency pointing out the positions of the charge transitions $\langle N \rangle = 40 \rightarrow 41 \rightarrow 42$. The measured curve (blue data points in Fig. 6.20(c)) however has a systematic shift

(green arrows in Fig. 6.20(c)) in the maxima with respect to the points of the charge transition toward the odd electron number valley with Kondo enhanced conductance. This is consistent with theoretical predictions for the conductance peaks in the Kondo regime: using the Anderson model with a non-crossing approach Wingreen et al. have shown that the transport through a quantum dot shows for decreasing temperature below the Kondo temperature a shift of the conductance peak position of spin-degenerate pairs towards each other [Wingreen and Meir, 1994]. Gerland et al. have shown that the peak position shifts with respect to the steepest point of the transmission phase $\Phi(V_g)$ (see Fig. 4 in [Gerland et al., 2000]). Since Friedel's sum rule provides a direct connection between Φ and $\langle N \rangle$ [Friedel, 1956], [Langreth, 1966], this also demonstrates a shift between charging and maximum current.

Experimentally, this shift has been first observed by Goldhaber-Gordon et al. in GaAs 2DEG (two dimensional electron gas) structures [Goldhaber-Gordon et al., 1998]. A combined measurement of the conductance and charging state of a QD have been performed by Sprinzak et al. where a quantum dot and an adjoined quantum point contact are electrostatically defined in a 2DEG system [Sprinzak et al., 2002]. The clear advantage of our system is that the CNT is both the basis for the quantum dot formed via tunnel barriers at sufficiently low temperatures with spin-induced Kondo co-tunneling, and it acts as charge detector via its mechanical activity. The benefit is a well controllable and clean system with less fabrication steps than would be necessary for systems based, e.g., on 2DEG structures.

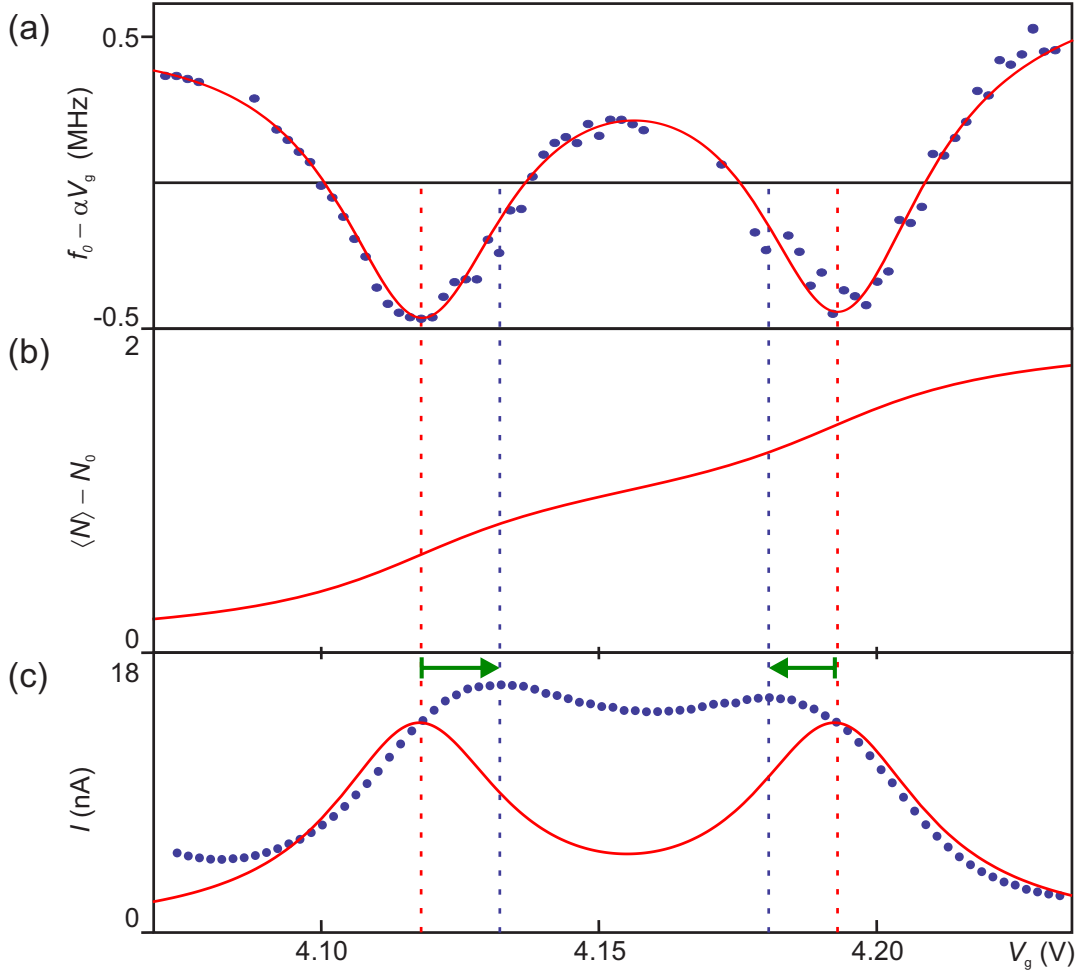


Figure 6.20: (a) The blue points show the extracted position of the resonance frequency f_0 with a linear gate dependence subtracted. It is fitted with Eq. 6.22 (red line) using the model as described in the text. (b) Time-average charge $\langle N \rangle$ (V_g) calculated with Eq. 6.21 using the parameters from the fit in (a). (c) Measured current $I(V_g)$ (blue points) and calculated SET current using again the parameters from (a) and Eq. 6.23.

6.4 Estimation of the amplitude of the CNT oscillation

As shown in Sec. 6.2 the stability diagram plotted in Fig. 6.21(a) shows discontinuities in the dc-current (highlighted with white arrows) which are attributed to self-oscillations of the mechanical vibration of the CNT [Usmani et al., 2007]. Furthermore, applying a perpendicular field allows us to induce additional damping of the mechanical resonator and therefore to suppress these mechanical features. This is depicted in Fig. 6.21(b) where the conductance is plotted as function of gate and bias voltage at finite magnetic field $B = 2$ T with restored bare electronic features. If one assumes that a finite amplitude of the CNT bending mode emerges in the dc-current solely via an averaging effect (see Sec. 6.1.3), it is possible to give a rough estimation of the CNT vibration amplitude in the case of feedback induced self-oscillations.

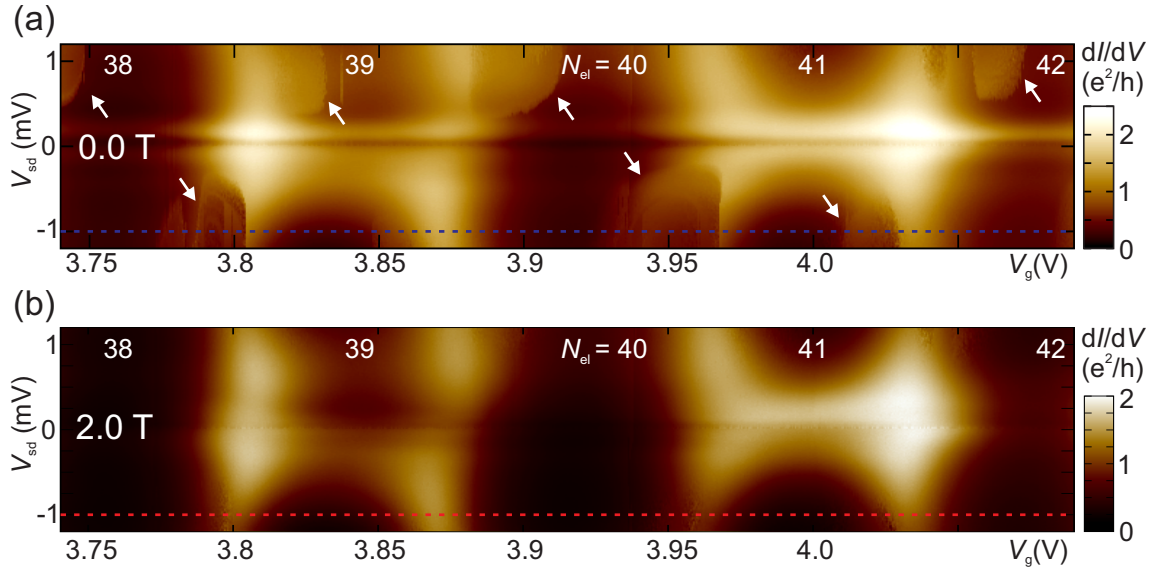


Figure 6.21: (a) Stability diagram $dI/dV_{sd}(V_g, V_{sd})$ for high electron numbers $38 \leq N_{el} \leq 42$, where mechanical instabilities are marked with white arrows. (b) Applying an external magnetic field $B = 2$ T damps the mechanical resonator and the self-oscillations vanish. *Cool down 2.*

Therefore, two cases of the gate dependence of the dc-current are compared: one without external magnetic field leading to strong feedback induced self-excitation of the bending mode (blue dashed line in Fig. 6.21(a)), and one with additional damping by a perpendicular magnetic field (red dashed line in Fig. 6.21(b)). The other parameters as gate range and temperature are kept constant. In Fig. 6.22 the

current is plotted at fixed bias voltage $V_{sd} = -1$ mV as function of the gate voltage V_g for zero magnetic field (blue data points) and for $B = 2$ T (red line in Fig. 6.22). Clearly visible are discontinuities in the data without magnetic field (blue curve), e.g. at $V_g \simeq 3.8$ V and $V_g \simeq 3.97$ V, while for the red curve the smooth undisturbed gate dependence of the current through the QD in the intermediate coupling regime is restored.

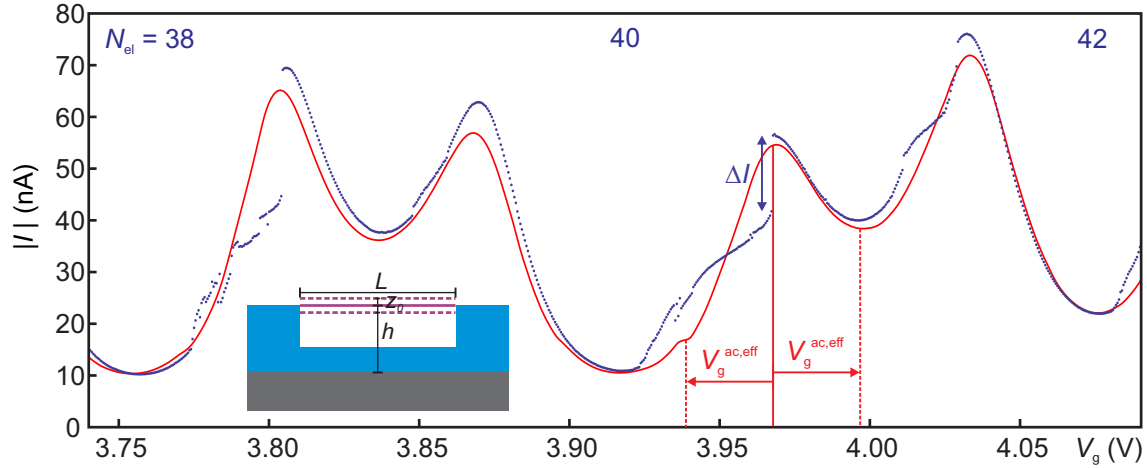


Figure 6.22: Blue data points show the absolute value of the current at fixed $V_{sd} = -1$ mV as indicated by the blue dashed line in Fig. 6.21(a) where discontinuities indicate the self-oscillation of the CNT resonator at zero field. The red curve represents the gate trace $|I|(V_g)$ for the same parameters as the blue points but with a finite field $B = 2$ T damping the resonator (red dashed line in Fig. 6.21(b)).

The latter curve is now used to reproduce the discontinuity in the current $\Delta I \simeq 14$ nA at $V_g = 3.97$ V (see Fig. 6.22) by numerical averaging as follows:

In the case of a finite vibration amplitude the resulting ac-gate capacitance C_g^{ac} can be interpreted as an effective gate voltage

$$V_g^{ac,eff} = V_g \cdot \frac{C_g^{ac}}{C_g}, \quad (6.24)$$

since the conductance depends on the so-called control charge $q_c = C_g V_g$.

Using the simplified picture of a wire with length L and radius r , representing our CNT, placed above an infinite conducting plate in the distance h (see insert in Fig. 6.22), the capacitance is given by

$$C_g = \frac{2\pi\epsilon_0 L}{\ln\left[\frac{2h}{r}\right]}.$$

Numerically averaging over the undisturbed current $|I|(V_g)$ (red curve) around the gate value of the discontinuity in the blue curve is given by

$$\bar{I} = \frac{1}{2 \cdot V_g^{\text{ac,eff}}} \cdot \int_{V_g - V_g^{\text{ac,eff}}}^{V_g + V_g^{\text{ac,eff}}} I(V_g) \cdot dV_g.$$

The difference $\Delta I_{\text{calc}} = |\bar{I} - I|$ is monotonously increasing with bigger integration width $V_g^{\text{ac,eff}}$, and it coincides with $\Delta I = 13.9 \text{ nA}$, which is the "step size" extracted from the self-oscillation region, for $V_g^{\text{ac,eff}} \simeq 29 \text{ mV}$. This calculated effective gate voltage is indicated by the red arrow in Fig. 6.22.

Via the definition of the effective gate voltage in Eq. 6.24 an alternating gate capacitance

$$C_g^{\text{ac}} \simeq 4 \cdot 10^{-20} \text{ F} = 40 \text{ zF}$$

is obtained. In the simplified model the amplitude of the alternating gate capacitance is

$$C_g^{\text{ac}} = \frac{2\pi\epsilon_0 L}{\ln \left[\frac{2(h-z_0)}{r} \right]} - \frac{2\pi\epsilon_0 L}{\ln \left[\frac{2(h+z_0)}{r} \right]}.$$

Taking the sample geometry parameters $L = 700 \text{ nm}$, $h = 350 \text{ nm}$, and $r = 1 \text{ nm}$ the amplitude of the CNT vibration in the case of a dc-current induced self-oscillation can be finally estimated to be

$$z_0 \simeq 8 \text{ nm},$$

i.e. about 1% of the resonator length.⁵ In the approximation of a harmonic oscillator with mass $m = 1.3 \cdot 10^{-21} \text{ kg}$ and resonance frequency $f_0 = 490 \text{ MHz}$ one obtains

$$n \simeq \frac{m\omega z_0^2}{2\hbar} \simeq 5 \cdot 10^4$$

as rough number of excited vibrational quanta, which would correspond to an effective temperature

$$T_{\text{eff}} \simeq 18\,000 \text{ K}$$

of a resonator in thermal equilibrium.

⁵Note, that the exact shape of the vibration envelope is not taken into account. Furthermore, any deflection of the CNT caused by the dc-gate voltage induced dc-force between CNT and substrate, is neglected, as are tension effects.

Chapter 7

Superconducting microwave resonators

7.1 Motivation

Superconducting coplanar waveguide (sc-cpw) resonators are electro-magnetic harmonic oscillators with resonance frequencies f_0 from some MHz to several GHz. Due to the low dissipation in the superconducting materials, very high quality factors in the range of $Q \sim 10^5$ are possible resulting in a very sharp resonance behavior. Using crystalline sapphire substrate further reduces damping in the substrate providing long photon decay rates $\kappa = \omega_0/Q$ [Sage et al., 2011], [O’Connell et al., 2008]. Additionally, in quasi one-dimensional transmission line resonators the mode volume V is very small resulting in exceptionally high vacuum field strengths [Wallraff et al., 2004]. Hence, the coupling strength, which is proportional to the electric field per photon $g \propto \mathcal{E} = \sqrt{\hbar\omega/2\varepsilon_0 V}$, can be increased dramatically by a reduced mode volume V , and even coupling to the vacuum mode is feasible [Abdumalikov et al., 2008]. A strong coupling to micro- or nano-objects is also possible [Csaba et al., 2007], which makes them to the predestined components in the research area of circuit quantum electro dynamic (cQED) [Wallraff et al., 2004]. Circuit QED applies the concept of cavity QED to on-chip structures, where the superconducting resonator represents the solid state physics analogon of an optical cavity. In one possible setup, the coherent coupling of a two-level system to a harmonic electro-magnetic resonator is examined to reveal the basic matter–light interaction in the scope of the Jaynes-Cumming model [Jaynes and Cummings, 1963] and even beyond [Bourassa et al., 2009], [Niemczyk et al., 2010]. Energy is coherently exchanged between a superconducting microwave resonator and a two-level system, an ”artificial atom”. Such lithographically designed on-chip structures show much

larger dipole moments than natural atoms and are tunable by external magnetic or electric fields [Abdumalikov et al., 2008]. This eases the path to the so-called strong coupling regime, where the coupling rate g between resonator and two-level system exceeds the decay rates of the cavity κ and of the two-level system γ .

The scope of this work was establishing the fabrication and characterization of cpw-resonators including the required measurement environment for characterization measurements. As a long-term objective, it targets the combination of this harmonic electro-magnetic oscillator with an ultra-clean carbon nanotube sample in order to couple its electronical and mechanical degrees of freedom to the harmonic spectrum. Therefore, first the fundamental electrical properties are presented, followed by a suitable fabrication process, and finally first resonance measurements on superconducting coplanar waveguide resonators are shown.

7.2 Microwave engineering

The derivation of the electronical properties of cpw-resonators starts with the calculation of the capacitance and inductance of the cpw transmission line, based on conformal mapping methods according to [Wang and Okoro, 1990], [Watanabe et al., 1994].

First, the complete elliptic integral of first kind is introduced by

$$K(k) = \int_0^1 \frac{dt}{\sqrt{(1-t^2)(1-k^2t^2)}},$$

where k is a function of the width w of the center electrode and the gap size s between center conductor and ground plane (see Figs. 7.1, 7.2), given by

$$k = \frac{w}{w + 2s}.$$

A geometric factor

$$g(w, s, d) = \frac{1}{2k^2K(k)^2} \left\{ -\ln \frac{d}{4w} - \frac{w}{w + 2s} \ln \frac{d}{4(w + 2s)} + \frac{2(w + s)}{w + 2s} \ln \frac{s}{w + s} \right\}$$

results from the shape of the transmission line cross section, where d is the thickness of the metal layer.

The inductance per unit length is composed of two components, the geometric inductance L_m and the kinetic inductance L_k , which stems from the inertia of Cooper pairs in the superconducting material. It strongly depends on T in vicinity to the critical temperature T_C due to the strong temperature dependence of the London

penetration depth λ close to T_C :

$$L = L_m + L_k = \frac{\mu_0 K(k')}{4K(k)} + \frac{\mu_0 \lambda^2}{dw} g(w, s, d). \quad (7.1)$$

Here μ_0 is the vacuum permeability and $k' = \sqrt{1 - k^2}$.

The capacitance per unit length stems from both substrate region C_{sub} and vacuum part C_{vac} :

$$C = C_{\text{sub}} + C_{\text{vac}} = 2\epsilon_0(\epsilon + 1) \frac{K(k)}{K(k')}, \quad (7.2)$$

where ϵ_0 is the vacuum permittivity and ϵ is the relative dielectric constant of the substrate material.

The effective dielectric constant ϵ_{eff} is then defined by the inductance and the capacitance from the Eqs. 7.1 and 7.2:

$$\epsilon_{\text{eff}} = L \cdot C \cdot c^2, \quad (7.3)$$

where c is the speed of light in vacuum. The impedance of the transmission line is the square root of the ratio inductance over capacitance, per unit length respectively:

$$Z = \sqrt{\frac{L}{C}}. \quad (7.4)$$

The calculated current density and the electric field distribution over the cross section of a cpw transmission line structure are shown in Fig. 7.1. The effective conductor backed structure, originating from placing the chip in a metallic sample holder, can be disregarded for the case of a small gap size s and center line width w compared to the sapphire substrate thickness h . This limit is fulfilled in our sample geometry, keeping the calculated impedance and the effective dielectric constant unaffected.

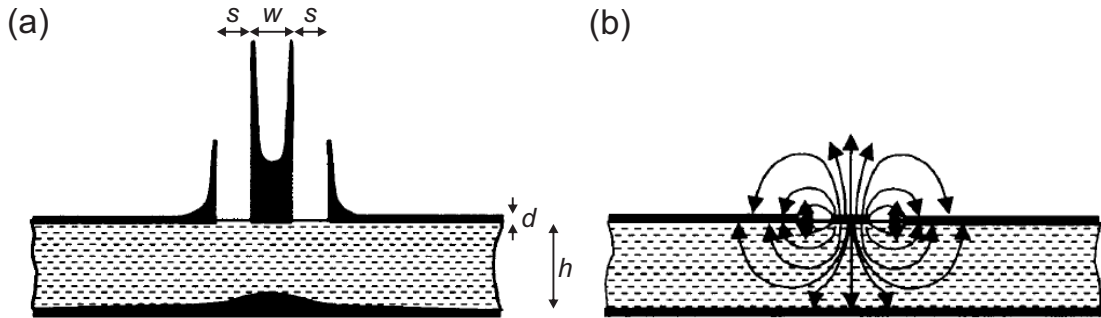


Figure 7.1: (a,b) Calculated current density (a) and electric field (b) distribution over the cross section of a coplanar waveguide geometry in the limit $h \gg s, w$. The metal layer thickness is labeled by d . Taken from [Wolff, 2006].

There are two basic types of cpw-resonators: the half- ($\lambda/2$) and quarter- ($\lambda/4$) wavelength resonator, each having different boundary conditions for the current and voltage. In Fig. 7.2 these two possible layouts of a cpw resonator are sketched. Figure 7.2(a) shows the geometry of a half-wavelength resonator. The signal couples capacitively via input and output capacitances, realized by small gaps in the center conductor, into the resonator. The distance of these gaps defines the resonator length l while the gap size itself corresponds to a capacitance which determines the input and output coupling.

In a quarter-wavelength resonator, sketched in Fig. 7.2(b), a cpw line of length $l = \lambda/4$ is coupled to a feeding line on one end, while the other end is grounded. The signal is guided in the feeding line and couples to the resonator if the resonance condition is met.

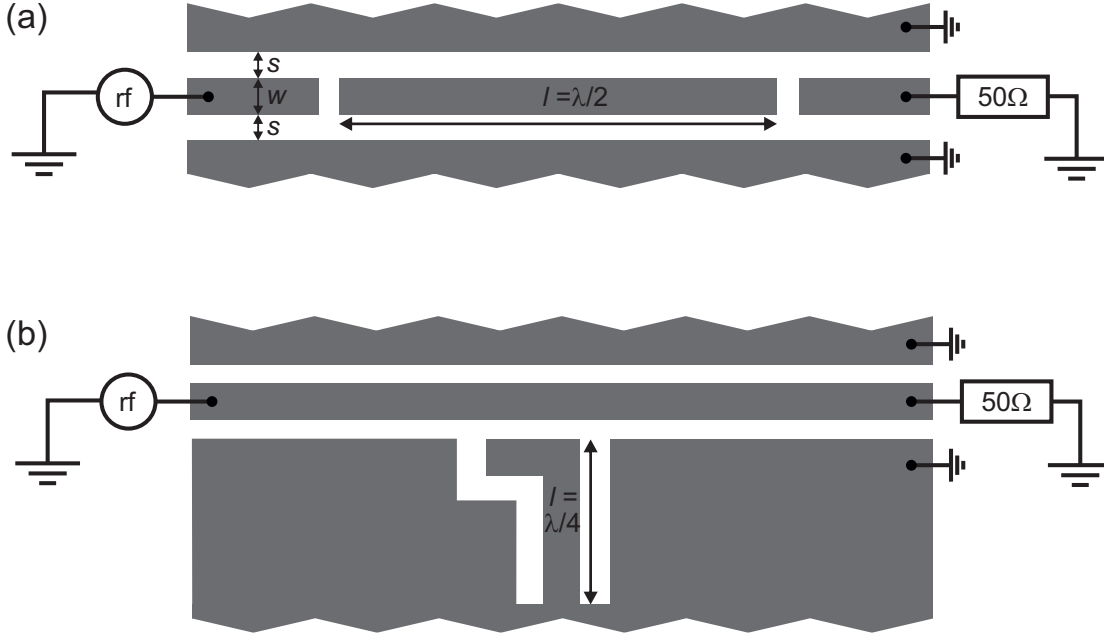


Figure 7.2: (a) Sketch of half-wavelength resonator where signal couples via coupling capacitances to input and output. (b) Sketch of quarter-wavelength resonator where resonator is coupled to a feeding line and is grounded at the other end.

The resonance wavelength is determined by the length l of the resonator and the boundary conditions, while the resonance frequency follows from the effective dielectric constant ϵ_{eff} , depending on the capacitance and inductance per unit length of the resonator (see Eq. 7.3).

Thus the fundamental resonance frequency of a transmission line $\lambda/2$ - resonator can

be written as

$$f_0 = \frac{1}{2l\sqrt{C \cdot L}} = \frac{c}{2 \cdot l \cdot \sqrt{\epsilon_{\text{eff}}}}, \quad (7.5)$$

while the fundamental resonance frequency of a $\lambda/4$ - resonator is given by

$$f_0 = \frac{c}{4 \cdot l \cdot \sqrt{\epsilon_{\text{eff}}}}. \quad (7.6)$$

7.3 Micro-fabrication of superconducting coplanar-waveguide resonators

For the fabrication of a microwave resonator in the GHz regime a cpw design is chosen, which has the lowest stray fields and losses. The conductor is realized by the superconductor rhenium or by the alloy $\text{Re}_{70}\text{Mo}_{30}$ to minimize the ohmic losses and thus to increase the quality factor Q of the resonator.

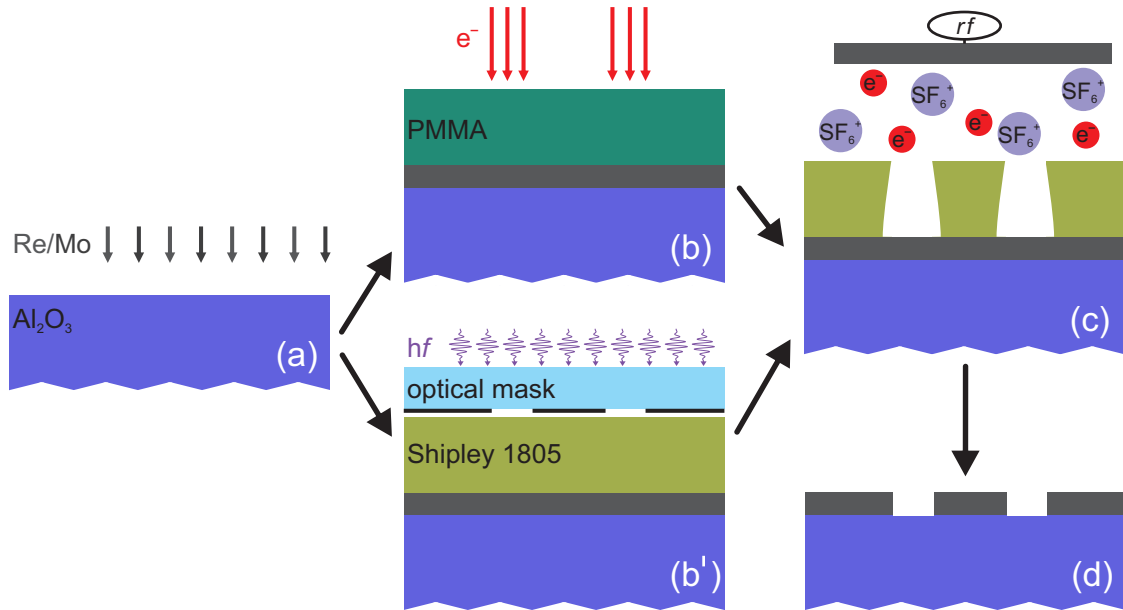


Figure 7.3: (a) Metallization of sapphire (Al_2O_3 [0001]) substrate with rhenium by sputtering in a UHV chamber. Defining centerline and ground plane is either done by electron beam lithography (b) with a focused electron beam or by optical lithography (b') using UV light and a mask to expose the photosensitive resist. (c) The exposed resist is developed and the metal is etched by reactive ion etching using SF_6 etching gas to define the gap between center conductor and ground planes. (d) After removing the resist with hot acetone the structures can be contacted with rf-electronics.

For ideal homogeneity, the whole chip is covered with a uniform metal layer by co-sputtering 60 nm $\text{Re}_{70}\text{Mo}_{30}$ as illustrated in Fig. 7.3(a). Starting with a completely metallized sapphire chip, center line and ground planes are defined with either optical lithography, or by electron beam lithography (EBL) in a scanning electron microscope (SEM) as shown in the Figs. 7.3(b') and (b), respectively. After developing the positive resist a reactive ion etching process using SF_6 as etching gas removes the surplus metal (see Fig. 7.3(d)). For the fabrication details see Appendix C. In order to avoid overheating of the resist by the hot plasma the process is split into steps of 10 seconds etching time with 30 seconds pause in between for cooling.

After removing the left-over resist with hot acetone the dc properties of the structure can be electronically checked using a probe station. In the case of λ -half resonators the coupling capacitance is defined via a gap in the center line. Here different possibilities have been examined. The most convenient way is to expose the center line gap in the same lithography step, but with the disadvantage that the structure can not be tested via its dc-resistance. The more extensive way is either an additional EBL and RIE etching step, or using a focused ion beam (FIB) machine to mill a thin stripe through the center conductor. A further advantage of the last FIB method is that the coupling capacitance can be adapted several times to trace the characteristics of the resonator, since the overall transmission and the loaded Q -factor strongly depend on the input and output coupling and can be adapted to the weak or strong coupling regime [Göppl et al., 2008].

The cpw resonator sample parameters used in this thesis, namely the metal layer thickness d , the center line width w , and the gap size s , are listed in Table 7.1, together with the calculated impedance Z using Eq. 7.4. The effective dielectric constant is obtained from Eq. 7.3 taking the literature value of the relative dielectric constant ϵ of the crystalline Al_2O_3 [0001] substrate.

metal	d	w	s	Z	ϵ	ϵ_{eff}
$\text{Re}_{70}\text{Mo}_{30}$	60 nm	$11.45 \mu\text{m}$	$5 \mu\text{m}$	50Ω	11.5	6.1

Table 7.1: Sample parameters of the cpw resonators used in the scope of this thesis.

In addition, $\lambda/4$ - resonators (as shown in Fig. 7.4) have been fabricated where resonators are on one end coupled to a feeding line and grounded on the other one. In this case, one has the possibility to analyze both rf-transmission and dc-conductance of the superconducting feeding line. That means one can check the contact to the sample holder, test the superconducting properties of the metal alloy and finally the loss of superconductivity at high input powers. Especially the last point is helpful to identify a suitable input power such that the resonance is not destroyed by the

measurement signal itself: one expects the loss of superconductivity in the resonator at much lower input powers compared to the feeding line since the corresponding ac-currents are strongly enhanced at resonance by the Q -factor.

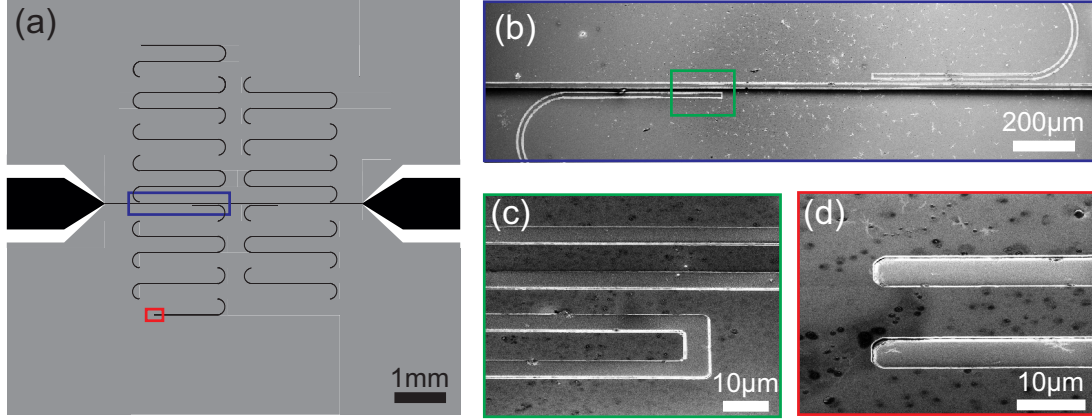


Figure 7.4: (a) CAD drawing of a quarter-wavelength cpw resonator. (b) SEM image of the coupling region near the feeding line (blue box in (a)). (c) SEM image with tilted stage of the coupled end of a quarter-wavelength resonator. (d) Grounded end of the resonator recorded by SEM imaging with tilted stage. The origin of the dirt on the surface and its effects on the resonator properties are so far unclear.

7.4 Measurement setup

The radio-frequency electrical properties of the measurement setup have to be well defined, e.g., every connection has to be tailored to $50\ \Omega$ impedance and the setup has to be shielded by using a copper box as sample holder. For first tests a ^4He dipstick was constructed with high frequency semi-rigid coaxial cables for input and output signal to measure the transmission of superconducting cpw-resonators (see Appendix D). Additionally, a sample holder was designed and fabricated by the mechanical workshop (see Fig. 7.5). The box volume has to be kept small to avoid cavity modes in the low GHz range which is accessed in our measurements.

Springs, made of a CuBe alloy wire are used, to guarantee elasticity even at liquid helium temperatures, in order to provide contact pressure of the resonator to SMA panel jacks (Rosenberger, 32K724-600S5). This box is mounted in the ^4He dipstick connected on input and output port to tin-plated aluminum semi-rigid cables. This way the signal from a signal generator (Rohde+Schwarz SMB100A) is conducted to the sample and further to a spectrum analyzer (R+S FSV Signal Analyzer) which is synchronized with the generator and detects the out-coming signal. A schematics

of the measurement setup is shown in Fig. 7.6, additional information is given in Appendix D.

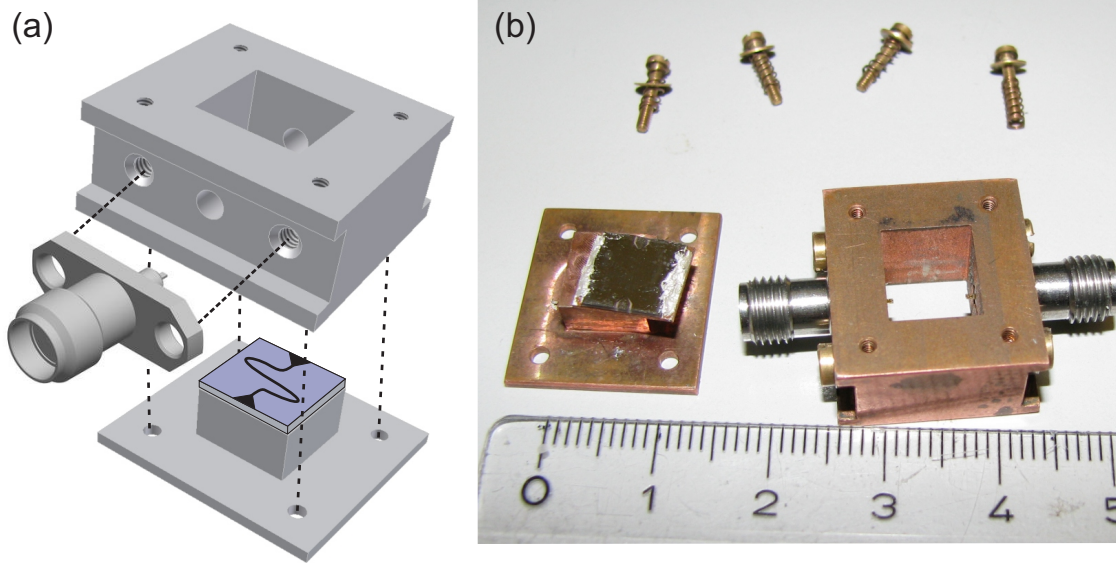


Figure 7.5: (a) CAD drawing of the sample holder with a sketch of a sample chip. (b) Picture of the finished sample holder.

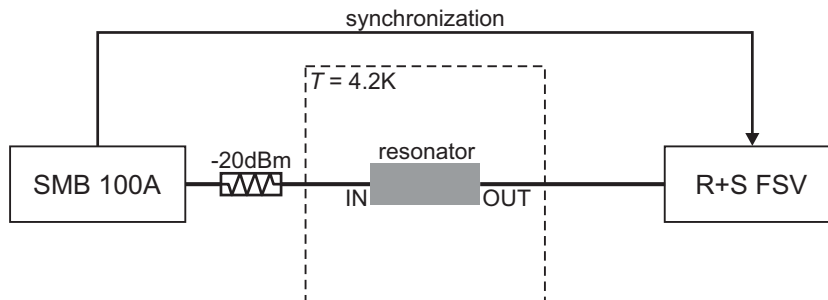


Figure 7.6: Sketch of the HF setup to measure the transmission of the micro-fabricated cpw resonators. The spectrum analyzer (R+S FSV) is locked to the 10 MHz reference frequency of the signal generator (SMB 100A). The signal is damped via an attenuator before entering the cryostat with $T = 4.2 K$.

7.5 Measurements and results

7.5.1 Superconducting films

For first characterization of the superconducting cpw resonator devices the ^4He dipstick from Section 7.4 is employed. This requires critical superconducting temperatures T_C of the resonator metal well above 4.2 K. Therefore co-sputtering is used to produce rhenium-molybdenum alloys with values of T_C exceeding that of pure rhenium [Hulm and Blaugher, 1961]. Four-point test measurements have shown an enhanced critical temperature T_C for the ReMo alloy compared with pure Re, both before and after the chemical vapor deposition (CVD) growth process. As depicted in Fig. 7.7, T_C can reach values around 8 K for untreated samples. In order to ease the comparison of the

metal film before and after the CVD process, a 4×4 mm chip is structured with several identical Hallbar geometries and cleaved into two parts; only one undergoes the CVD process. Combining the two halves in one chip carrier allows the measurement of T_C for different treatment in the same cool-down and for exactly the same metal composition and thickness. Lock-in measurements trace the resistance while ramping the temperature.

The general reduction of T_C by the CVD process can likely be attributed to the inclusion of hydrogen gas into the metal lattice [Ducros et al., 1976], though no detailed data on the effect of the exact gas composition used in CVD exists in literature.

7.5.2 RF measurements on sc-cpw resonators

The measurements presented in this section were done in cooperation with the diploma and master students H. Kraus and B. Hartmann [Kraus, 2013], [Hartmann, 2014].

Using a signal generator and a spectrum analyzer the transmission spectrum through the resonator can be measured. Within this thesis the focus is on the quarter-

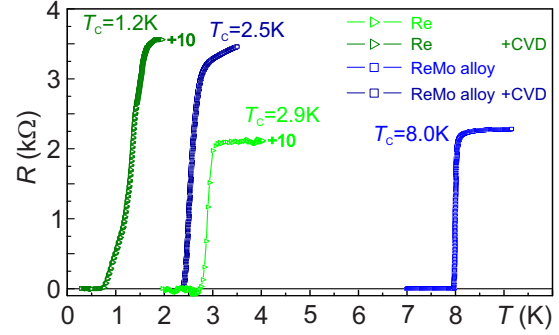


Figure 7.7: Temperature dependence of the resistance of pure rhenium and rhenium molybdenum alloys before and after the CVD process. Different values of the critical temperature T_C are observed.

wavelength resonators, since the feeding line allows a dc-resistance measurement to check contact of the spring-contact connections and the superconducting behavior of the metal film. The metal layer is co-sputtered with a defined volume ratio ReMo (70:30) and total thickness of $d = 60$ nm as explained in detail in Sec. 7.3. The measurements have been performed by Hermann Kraus within the framework of his master thesis.

Since a resonance condition leads to a decreased transmission sharp dips in the frequency trace are expected to occur close to the designed resonance frequencies which are related to the resonator lengths. This is exactly observed in a first measurement with four quarter-wavelength resonators in parallel to each other as depicted in Fig. 7.4(a). Figure 7.8 shows the frequency dependence of the attenuation $\alpha \equiv -(P_{\text{OUT}} - P_{\text{IN}})$ for a fixed nominal input power $P_{\text{IN}} = -32$ dBm at $T = 4.2$ K. Besides a nearly periodic modulation of the attenuation caused by the intrinsic cable resonances sharp dips (marked with arrows) are observed, where the transmission signal drops by several orders of magnitude.

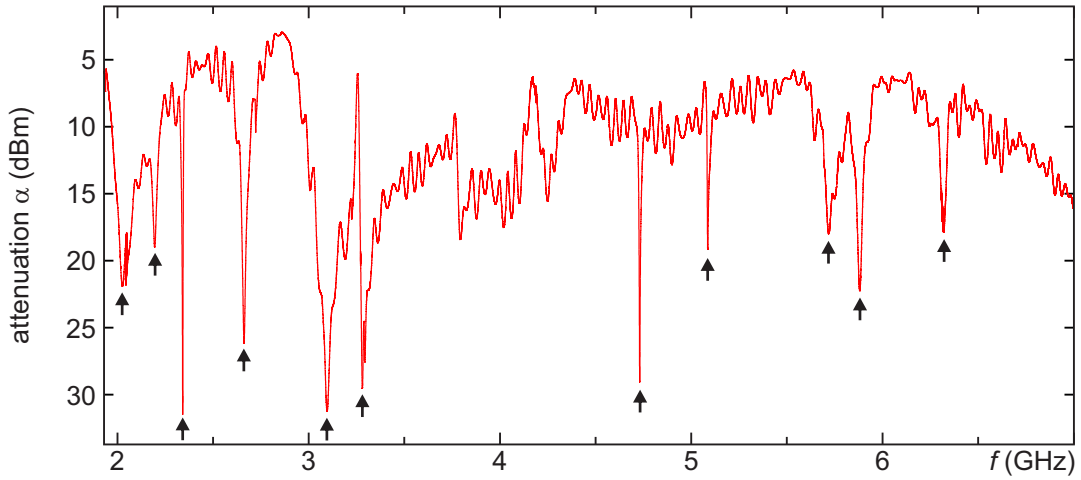


Figure 7.8: Frequency dependence of the attenuation at fixed input power $P_{\text{IN}} = -32$ dBm for four quarter-wavelength resonators coupled to one feeding line as depicted in Fig. 7.4(a). Sharp dips (marked with arrows) indicate a resonance condition of one quarter-wavelength resonator where the output signal P_{OUT} drops by several orders of magnitude. The sample is immersed into liquid helium keeping the temperature constant at $T = 4.2$ K.

In order to prove that the appearing resonances stem from the superconducting resonator, the input power is stepwise increased to destroy the superconductivity of the metal in the resonators due to the high current densities. Resonances are expected to disappear above a certain sample specific input power due to the strongly

increased damping by the finite resistance. As can be seen in Fig. 7.9(a) this is indeed the case for, e.g., the resonance dip at $f_0 \simeq 2.341$ GHz, which disappears abruptly at $P_{\text{IN}} \simeq -17$ dBm. The frequency dependence of the signal attenuation for an exemplary input power $P_{\text{IN}} = -35$ dBm (dashed line in Fig. 7.9(a)) is plotted in Fig. 7.9(b). It shows a pronounced dip in the transmission power, i.e. a peak in the attenuation. The Q -factor can be determined from the full width δf at half maximum. It follows, that $Q = f_0/\delta f = 2.341 \text{ GHz}/1.31 \text{ MHz} \simeq 1800$. The low value is either caused by the high coupling of the resonator to the feeding line, or by damping mechanisms which are so far not understood. One possibility is the rough metal surface (see SEM images in the Figs. 7.4(b)–(d)), observed after several cool-downs. For a more detailed analysis of the Q -factors, several resonators with different coupling strengths have to be compared.

An identification of the observed resonance frequencies in Fig. 7.8 as ground mode and higher harmonics of the designed resonators with Eq. 7.6 was not possible, likely hampered by flaws in the fabrication process [Kraus, 2013].

In the case of half-wavelength resonators a peak in the transmission is expected, where a standing wave is formed in the resonator increasing the transmission. As in the case of the quarter-wavelength resonator the resonance will vanish at sufficiently high input powers, where the superconductivity of the center line is destroyed, increasing the resonator's damping. First test have been performed with half-wavelength resonators, however so far no regular behavior has been observed, and test measurements are still ongoing.

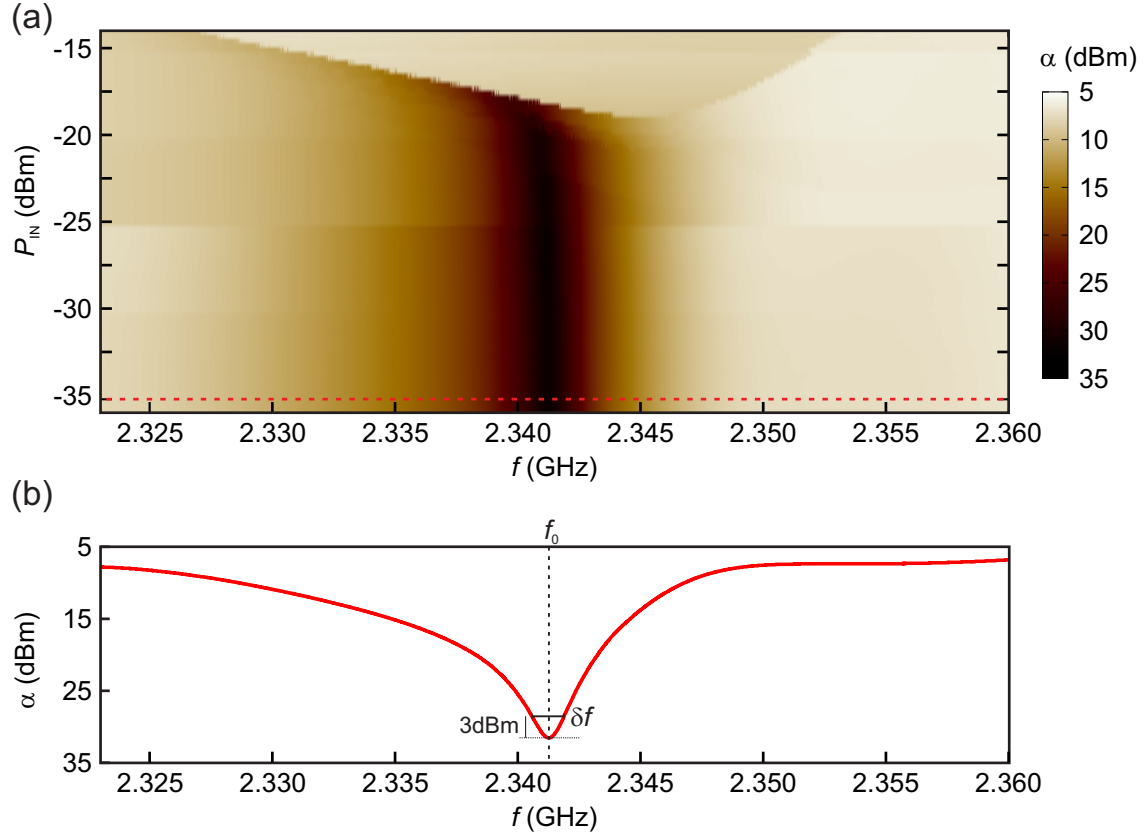


Figure 7.9: (a) Attenuation of a quarter-wavelength resonator around one resonance frequency of the line trace in Fig. 7.8 for increasing input power P_{IN} . (b) Exemplary frequency dependence of the damping $\alpha(f)$ at $P_{\text{IN}} = -35$ dBm, as indicated by the dashed line in (a), shows a sharp dip at the resonance frequency $f_0 \simeq 2.341$ GHz with $\delta f \simeq 1.31$ MHz. This allows to extract a quality factor of $Q \simeq 1800$.

Chapter 8

Conclusion and Outlook

In the scope of this thesis we have investigated the electro-mechanical properties of suspended carbon nanotubes (CNTs) based on experiments performed, e.g., at Cornell University [Sazonova et al., 2004], Delft University of Technology [Hüttel et al., 2008], [Hüttel et al., 2009b], [Steele et al., 2009], [Meerwaldt et al., 2012], or at Universitat Autònoma de Barcelona [Lassagne et al., 2009], [Chaste et al., 2011]. Following [Cao et al., 2005] we have established the fabrication of ultra-clean, defect-free and freely suspended CNTs by shifting the CNT growth process to the very last step of the chip preparation, which reduces contamination and damaging mechanisms. Based on this technique it was possible to fabricate single quantum dots (QDs) embedded in freely suspended CNTs. Numerous low temperature transport measurements have been performed at temperatures down to $T = 30$ mK on a single CNT sample, starting with detailed measurements on electronic properties of the CNT QDs, up to more elaborated experiments on the interplay between single electron tunneling and mechanical degrees of freedom.

Electronic transport spectroscopy has been performed in various coupling regimes ranging from the Fabry-Pérot via the intermediate coupling regime with Kondo enhanced transport, to the Coulomb blockade dominated few electron charging states. In particular, we have investigated the level spectrum of the first electrons by, e.g., tracing the magnetic field dependence of the single-electron ground state and excited states in different field orientations. The absence of any electron-electron interaction in the one electron case provides us with a very accurate determination of the internal parameters of the first longitudinal modes of the CNT QD, such as the spin-orbit coupling and the KK' -mixing energy. We also present preliminary results on spectroscopy measurements of the two-electron state, which exhibits much richer physics than the single-particle state. Furthermore, we explored the effect of an external magnetic field on the zero-bias conductance for the first holes. These promising re-

sults are encouraging for further, more detailed analysis with the support from the theory in order to reveal the spectrum of the carbon nanotube quantum states.

At higher electron numbers, where increasing tunnel rates give rise to the Kondo effect, we have observed unconventional Kondo features in the non-equilibrium transport measurements. In cooperation with the theory group of M. Grifoni, a many-body field theory has been developed providing a so far unconsidered many-body selection rule, which reproduces our experimental results with very good agreement [Schmid et al., 2014].

In addition to the regular and controllable electronic states in CNT QDs, suspended nanotubes also provide extraordinary mechanical properties with different vibration modes, which couple in a very distinct way to the charge transport. Besides the quantized longitudinal stretching mode, which becomes visible via phonon-assisted tunneling features, the main focus of this work is on the transversal bending mode. The properties of this mode have been analyzed over a wide range of gate voltages and coupling regimes in terms of interaction between single electron charging and the mechanical resonance frequency.

For instance, an external magnetic field perpendicular to the plane of vibration has been shown to reduce the resonator's effective Q -factor. The system could be modeled with an electronic equivalent circuit, where an additional damping mechanism occurs via Ohmic dissipation of eddy currents, which are generated by the CNT vibration. The dependence on the external magnetic field strength can be reproduced [Schmid et al., 2012]. Our results have been confirmed by [Nocera et al., 2013] in strict quantum mechanical calculations. Additionally, we have exploited the high sensitivity of the resonance frequency on the QD charging state, which provides an excellent charge detector. This allows us to sense the charging of the nanotube in the deep Kondo regime, while no additional nano-fabricated sensor circuits are required. We were able to show a systematic shift of the conductance maxima relative to the charging of the quantum dot in a strongly Kondo correlated QD. This result reproduces theoretical predictions based on different models, and extends its experimental confirmation to CNT systems.

Finally we present first steps toward coplanar waveguide (cpw) resonators for the GHz regime by working out the fabrication of superconducting thin films and the micro-structuring of those. An accurately defined electronical environment has been reached by the construction of a high frequency sample holder for measurements at liquid helium temperatures. Besides dc-characterization of the superconducting properties of the adapted metal alloys first rf-signal transmission measurements have been performed as starting point for further improvements of the reproducibility and quality of the resonators.

The results obtained within this thesis pave the way towards very recent topics in fundamental research. The coupling of a mechanical resonator to a microwave photon field in cpw-resonators enables mechanical ground state cooling in the so-called good-cavity limit, where the linewidth of the microwave resonator is much smaller than the mechanical resonance frequency, i.e. in the case of resolved phonon sidebands [Marquardt et al., 2007]. In published experiments, top-down fabricated nano-mechanical beam resonator has been coupled to a quarter-wavelength resonator to induce damping and active cooling below the surrounding thermal bath temperature [Teufel et al., 2008], [Regal et al., 2008]. Compared with these experiments, the high resonance frequency of the bending mode, originating from the low mass density and the high stiffness of CNTs, causes a very low number of thermally excited vibration quanta already at common temperatures $T \simeq 50$ mK in a dilution cryostat. This provides an ideal starting point for quantum-limited measurements in the mechanical ground state with the prospect to prepare and measure non-classical mechanical states in a mesoscopic system [O’Connell et al., 2010].

Further the cpw resonator can be used to readout the charging state of an embedded CNT quantum dot due to a strong electron-photon coupling strength [Delbecq et al., 2011]. Such strong coupling has also been demonstrated in more advanced hybrid solid-state devices. For instance, Frey et al. have dipole coupled a double quantum dot (electrostatically defined in a 2DEG) to the microwave field of a superconducting cpw resonator via a gate finger [Frey et al., 2012]. The Regensburg research group is also member of the SFB 631 ”Solid-State Quantum Information Processing”. An objective there is the implementation of a CNT double quantum dot coupled to a sc-cpw resonator to study charge- or spin-qubit features of the double quantum dot. Here, CNTs provide a potentially long decoherence time thanks to the absence of hyperfine interaction, which is essential for the control, manipulation, and read-out of these qubits.

Many more promising ideas for transport measurements on overgrown CNTs exist. Focusing on the ultra-clean fabrication the process can be adapted to more sophisticated structures like double QDs, or to the coupling to other contact materials as, e.g., ferromagnetic alloys. This enables the observation of tunnel magneto resistance effects and a controllable spin valve behavior [Sahoo et al., 2005]. Clean QD systems in different coupling regimes to superconductors make either Andreev bound state spectroscopy [Pillet et al., 2010], [Kumar et al., 2014] on, or Josephson coupling [Grove-Rasmussen et al., 2007] via a very controllable quantum system possible. Especially in a dc-SQUID setup a system is provided which is very sensitive to the CNT deflection [Schneider et al., 2012]. The interplay of the Josephson effect and the mechanical motion will provide additional rich fundamental physics. The work in this thesis has laid foundations to many such future projects in Regensburg.

Appendix A

CNT fabrication

A.1 Optical lithography

A 4" highly positive (boron) doped Si $\langle 110 \rangle$ wafer with 300 nm thermally grown and polished SiO_x on the top side is cut into 8×8 mm pieces and exposed to an oxygen plasma at 1.8 mbar for 3 minutes. An ultrasonic bath in hot acetone followed by rinsing with iso-propanol cleans the surface from organic residues. For optical lithography the positive photoresist *Shipley 1805* is used, which is spin-coated on the substrate at 4500 rpm for 30 seconds and baked out on the hotplate at 90°C for 2 minutes. Then the resist is exposed with ultra-violet light in a mask aligner (type: *Karl Suss MJB3*). The exposure time strongly depends on the total chrome-plated area and was found to work best for 33 seconds. The developer is a mixture of $\text{NaOH}/\text{H}_2\text{O}$ at a mixing ratio of 1 : 3, where the developed chip is immersed for 40 seconds followed by rinsing in high-purity water.

A.2 Electron beam lithography

After cleaning the sample of organic chemicals using acetone and iso-propanol, polymethyl-methacrylate (PMMA) 200k 3.5% dissolved in chlorobenzene is used as resist by spin-coating the sample at 3000 rpm (5 s)/ 8000 rpm (30 s) and baking on the hotplate at 150°C for 6 minutes.

The electron beam lithography (EBL) is performed in a *Zeiss LEO* electron microscope. The acceleration voltage is fixed to 25 kV. The best result has been achieved with an area dose of $195 \mu\text{C}/\text{cm}^2$ using the $30 \mu\text{m}$ aperture. This results in a beam current of about 300 pA. A mixture of one part methyl-isobutylketone (MIBK) plus three parts iso-propanol is used to develop the exposed resist for two minutes followed by 30 seconds rinsing in iso-propanol.

A.3 Metallization and reactive ion etching

In a high-vacuum chamber with base pressure $p \simeq 10^{-8}$ 40 nm rhenium (Re) metal is dc-sputtered with an argon plasma (Ar 6.0) at a pressure of $p_{\text{Ar}} = 5 \cdot 10^{-3}$ mbar. The power is set to 100 W to obtain a deposition rate of 1.6 \AA/s .

Afterwards, reactive ion etching (RIE) in an Oxford Instruments *Plasmalab80Plus* machine is used to etch the silicon oxide selectively and anisotropically where the metal structure forms the etch mask. In Table A.1, the explicit recipe used in this thesis is given. The etching is used to define the trenches over which the carbon nanotubes are grown.

etching gas	gas flow	pressure	RF power	rate	time
CHF ₃	50 sccm	55 mTorr	150 W	17 nm/min	360 s
Ar	40 sccm	30 mTorr	150 W	8 nm/min	30 s

Table A.1: Recipe for the reactive ion etching of SiO_x, used to define the trenches between the electrodes in order to guarantee freely suspended CNTs.

The etching step deepens the trenches between the rhenium contacts from 40 nm to about 200 nm in total to ensure freely suspended CNTs.

A.4 Catalyst for the carbon nanotube growth

A disc-shaped region of $2 \mu\text{m}$ in diameter is exposed in the middle of the circular electrode structures. The exposure dose for the PMMA 200k 3.5% is set to $300 \mu\text{C/cm}^2$ at fixed acceleration voltage of 25 kV.

The catalyst for the CNT growth is suspended in 30 ml methanol with weighed constituents as given in Table A.2.

40.0 mg	Fe(NO ₃) ₃ · 9H ₂ O
30.0 mg	Al ₂ O ₃ nanoparticles (diameter 14 nm)
10 mg	[CH ₃ COCH=COCH ₃] ₂ MoO ₂

Table A.2: Catalyst composition for the CVD growth process of carbon nanotubes.

The catalyst suspension is mixed in the ultrasonic bath for 45 minutes, and a few drops of the suspension are deposited on the sample. After 2 – 3 seconds the sample is blown dry with nitrogen and the chip is placed on the hot plate for 6 minutes

at 150°C. In a final lift-off process the resist with the surplus catalyst is removed in 60°C hot acetone leaving catalyst only at the defined areas in the center of the circular electrode.

A.5 Chemical vapor deposition growth process

The standard recipe in Regensburg for the chemical vapor deposition (CVD) carbon nanotube growth process contains the following steps:

- open gas bottle and valves for methane, hydrogen and argon gas
- place 2" quartz tube in oven and place sample in the middle
- connect quartz tube with gas lines by caps
- open all three gas flow meters to maximum scale to rinse the lines and the quartz tube for 2 min (remove other gases, as e.g. oxygen)
- close methane and hydrogen and rinse with 1500 sccm argon for 2 min
- switch on oven heating up to 900°C
- when target temperature is reached, open hydrogen valves and adjust a flow of 700 sccm; close argon
- open gas flow meter of methane to 800 sccm for 10 min growth time
- to stop CNT growth, close methane and flood with argon at 1500 sccm
- switch off oven and cool down in argon/ hydrogen atmosphere to 150°C before taking out the sample

Appendix B

Assignment of the cool-downs to the different measurement setups

Both the electronic spectroscopy of the CNT QD and the measurements on the nano-electro-mechanical properties of the suspended CNT have been performed on one single nanotube sample. This provides a high degree of comparison between the electronical and mechanical properties and their dependence on external parameters like temperature T or magnetic fields B , in addition with a wide range of transport regimes. To collect a comprehensive and complete set of data the sample has been cooled down in several systems providing different minimum temperatures T_{base} , maximum magnetic fields B_{max} , and different measurement environments. Explicitly, the data presented in this thesis were obtained from three cool-downs, which are listed in the Table B.1 including the specifications.

Cool down	cryostat type	T_{base}	B_{max}	sample environment
<i>Cool down 1</i>	^3He evaporation	300 mK	12 T	vacuum
<i>Cool down 2</i>	$^3\text{He}/^4\text{He}$ dilution	30 mK	8 T	vacuum
<i>Cool down 3</i>	$^3\text{He}/^4\text{He}$ dilution	30 mK	17 T	$^3\text{He}/^4\text{He}$ -mixture

Table B.1: Assignment of the different cool-downs to the respective cryostat specifications.

While the magnetic field orientation in *cool down 1* and *2* was perpendicular to the CNT axis, in *cool down 3* the field orientation was adjustable thanks to a rotatable sample holder. This allowed especially the continuous in situ rotation from perpendicular to parallel orientation of the magnetic field with respect to the CNT axis.

Appendix C

Fabrication of sc-cpw resonators

C.1 Co-sputtering ReMo-alloys

Addressing two sputter sources with adjusted powers P_{rf} allows to produce thin films with arbitrary alloy compositions of rhenium (Re) and molybdenum (Mo) on top of mono-crystalline sapphire (Al_2O_3 [0001]) substrate with dimensions $8 \times 8 \times 0.5 \text{ mm}^3$. For the sputtering process, the sample holder is horizontally adjusted to obtain identical incident angles for both sources. In order to calibrate the individual sputtering rates the sources are activated one by one while storing the sample in the load lock chamber. For a fixed chosen ratio of sputter rates at constant chamber pressure p one obtains a well-defined alloy composition. The total layer thickness d is determined by the total sputtering rate and the sputter time t . The exact sputtering parameters used during this thesis can be found in Table C.1.

metal	P_{rf} (W)	p (μbar)	rate ($\text{\AA}/\text{s}$)	vol. ratio (%)	t (s)	d (nm)
Re	65	5	1.17	70	360	60
Mo	75	5	0.5	30		

Table C.1: Sputtering parameters for the $\text{Re}_{70}\text{Mo}_{30}$ films used as superconducting cpw-resonator material.

C.2 Reactive ion etching

Starting with a completely metallized sapphire chip, the coplanar waveguide structure is defined via reactive ion etching (RIE), where the surplus metal is removed in an Oxford Instruments *Plasmalab80Plus* system. The PMMA resist, defined in a preceding electron beam lithography (EBL) step and acting as etch mask, does not withstand high temperatures in the RIE plasma. In order to avoid overheating of the resist, the total etching process is subdivided into units of 10 seconds etching with 30 seconds thermalization time in between. The parameters for one etching sequence are given in Table C.2.

etching gas	gas flow	pressure	RF power	time
SF ₆	20 sccm	20 mTorr	100 W	10 s
–	0 sccm	0 mTorr	0 W	30 s

Table C.2: One sequence of the reactive ion etching recipe to define ReMo thin film cpw-resonator structures.

This sequence is repeated 16 times to etch the 60 nm ReMo metal layer. A prior etching test for these parameters has yielded an etching rate of 4 nm/10 s.

Appendix D

HF-equipment

In order to measure the transmission through the superconducting cpw-resonators a combination of a signal generator (*R+S SMB100A*) and a signal spectrum analyzer (*R+S FSV*) is used, depicted in Fig. D.1. The spectrum analyzer sets the 10 MHz frequency reference, which is provided to the signal generator via an external port. During the sweep of the radio frequency signal by the *SMB100A*, the scan center of the *FSV* is adjusted with a fixed scan width and resolution. For each measurement point the *FSV* searches for the maximum in the frequency spectrum and the height of the signal peak is queried by the measurement interface.

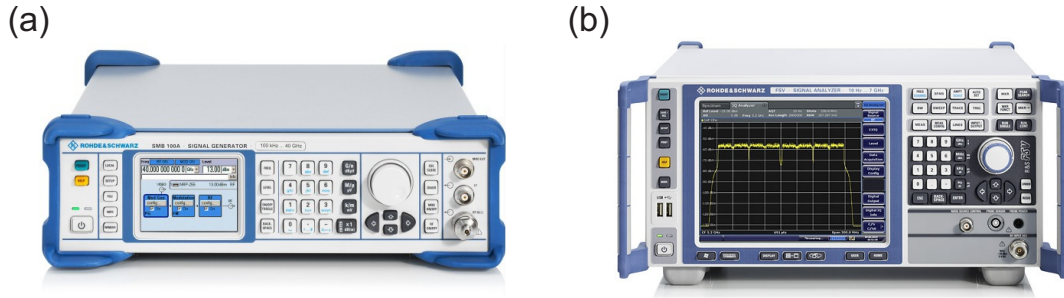


Figure D.1: (a) *Rohde+Schwarz SMB100A*. Power range is $P = -145 - 30$ dBm, and the frequency range is $f = 9$ kHz $-$ 6 GHz. (b) *Rohde+Schwarz FSV* Signal Analyzer. Detectable frequency range is $f = 10$ Hz $-$ 7 GHz. [Pictures from the R+S[®] web site, <http://www.rohde-schwarz.com>]

The sample is mounted in a HF sample holder as shown in Sec. 7.4 providing a good electric shielding. A dipstick has been designed where the setup is immersed directly into the liquid helium ensuring a good thermalization to $T = 4.2$ K, to cool the resonator below the critical temperature of the superconducting metal. Photographs of this dipstick are shown in Fig. D.2. Baffles distributed over its length

reduce the heat input by convection and thermal radiation. The assembly is fixed on an aluminum box with four ports for SMA connectors (see III in Fig. D.2(b)). An additional connector (II) leads the evaporating helium into the recovery line. At the lower end the sample holder (IV in (c)) is mounted and connected to semi-rigid cables (V) for transmission measurements.

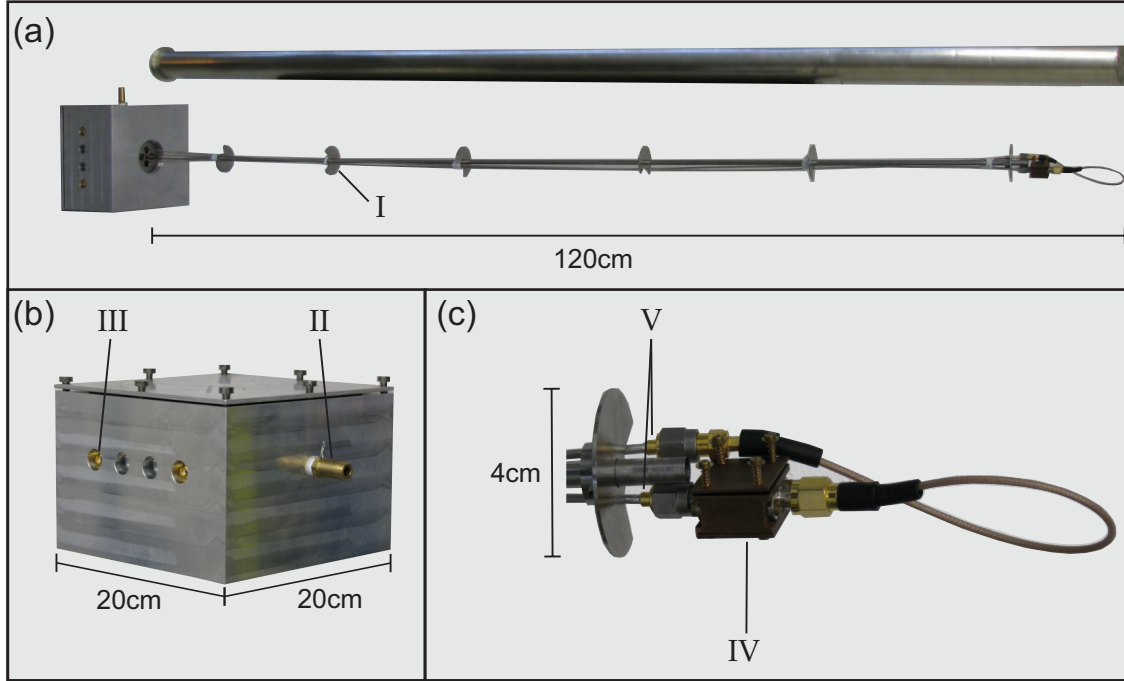


Figure D.2: (a) HF dipstick with removed outer shielding. The sample holder is mounted at the bottom 120 cm distant from the connector box. Six stainless steel discs provide the guiding of the inner part in the shielding tube and reduce room temperature thermal radiation from the top and convection in the stick. (b) Connector box with a plug for the helium recovery (II) plus four potential ports for SMA connectors (III) to access the input and output lines. (c) Details of the lowest part of the assembly where the sample holder (IV) is mounted and connected to semi-rigid Al-Al coaxial cables (*Huber-Suhner, Multiflex 86*) with SMA connectors (*Rosenberger, 32S102-271L5*) soldered on both ends (V).

Bibliography

- [Abdumalikov et al., 2008] Abdumalikov, A., Astafiev, O., Nakamura, Y., Pashkin, Y., and Tsai, J. (2008). Vacuum Rabi splitting due to strong coupling of a flux qubit and a coplanar-waveguide resonator. *Physical Review B*, 78(18):180502.
- [Altland and Simons, 2010] Altland, A. and Simons, B. (2010). *Condensed Matter Field Theory*. Cambridge University Press, Cambridge, 2 edition.
- [Anderson, 1961] Anderson, P. W. (1961). Localized magnetic states in metals. *Phys. Rev.*, 124:41–53.
- [Beenakker, 1991] Beenakker, C. W. J. (1991). Theory of Coulomb-blockade oscillations in the conductance of a quantum dot. *Physical Review B*, 44(4):1646–1656.
- [Bockrath et al., 1999] Bockrath, M., Cobden, D. H., Lu, J., Rinzler, A. G., Smalley, R. E., Balents, L., and McEuen, P. L. (1999). Luttinger-liquid behaviour in carbon nanotubes. *Nature*, 397(6720):598–601.
- [Bockrath et al., 1997] Bockrath, M., Cobden, D. H., McEuen, P. L., Chopra, N. G., Zettl, A., Thess, A., and Smalley, R. E. (1997). Single-electron transport in ropes of carbon nanotubes. *Science*, 275(5308):1922–1925.
- [Bourassa et al., 2009] Bourassa, J., Gambetta, J., Abdumalikov, A., Astafiev, O., Nakamura, Y., and Blais, A. (2009). Ultrastrong coupling regime of cavity QED with phase-biased flux qubits. *Physical Review A*, 80(3):032109.
- [Cao et al., 2005] Cao, J., Wang, Q., and Dai, H. (2005). Electron transport in very clean, as-grown suspended carbon nanotubes. *Nature Materials*, 4(10):745–749.
- [Carr and Craighead, 1997] Carr, D. W. and Craighead, H. G. (1997). Fabrication of nanoelectromechanical systems in single crystal silicon using silicon on insulator substrates and electron beam lithography. *Journal of Vacuum Science & Technology B: Microelectronics and Nanometer Structures*, 15(6):2760.

- [Charlier et al., 2007] Charlier, J.-C., Blase, X., and Roche, S. (2007). Electronic and transport properties of nanotubes. *Reviews of Modern Physics*, 79(2):677–732.
- [Chaste et al., 2011] Chaste, J., Sledzinska, M., Zdrojek, M., Moser, J., and Bach-told, A. (2011). High-frequency nanotube mechanical resonators. *Applied Physics Letters*, 99(21):213502.
- [Cleland, 2003] Cleland, A. N. (2003). *Foundations of Nanomechanics*. Springer, Berlin.
- [Cleland and Roukes, 1996] Cleland, A. N. and Roukes, M. L. (1996). Fabrication of high frequency nanometer scale mechanical resonators from bulk Si crystals. *Applied Physics Letters*, 69(18):2653.
- [Cobden and Nygard, 2002] Cobden, D. and Nygard, J. (2002). Shell Filling in Closed Single-Wall Carbon Nanotube Quantum Dots. *Physical Review Letters*, 89(4):046803.
- [Cronenwett et al., 1998] Cronenwett, S. M., Oosterkamp, T. H., and Kouwenhoven, L. P. (1998). A Tunable Kondo Effect in Quantum Dots. *Science*, 281(5376):540–544.
- [Csaba et al., 2007] Csaba, G., Màtyàs, A., Peretti, F., and Lugli, P. (2007). Circuit modelling of coupling between nanosystems and microwave coplanar waveguides. *International Journal of Circuit Theory and Applications*, 35(3):315–324.
- [Delbecq et al., 2011] Delbecq, M. R., Schmitt, V., Parmentier, F. D., Roch, N., Viennot, J. J., Fève, G., Huard, B., Mora, C., Cottet, A., and Kontos, T. (2011). Coupling a Quantum Dot, Fermionic Leads, and a Microwave Cavity on a Chip. *Physical Review Letters*, 107(25):256804.
- [Deshpande and Bockrath, 2008] Deshpande, V. V. and Bockrath, M. (2008). The one-dimensional wigner crystal in carbon nanotubes. *Nature Physics*, 4(4):314–318.
- [Deshpande et al., 2009] Deshpande, V. V., Chandra, B., Caldwell, R., Novikov, D. S., Hone, J., and Bockrath, M. (2009). Mott insulating state in ultraclean carbon nanotubes. *Science*, 323(5910):106–110.
- [Ducros et al., 1976] Ducros, R., Ehrhardt, J. J., Alnot, M., and Cassuto, A. (1976). Hydrogen and deuterium adsorption on polycrystalline rhenium surfaces; effect of carbon and oxygen coadsorption. *Surface Science*, 55(2):509–522.

- [Eichler et al., 2011] Eichler, A., Chaste, J., Moser, J., and Bachtold, A. (2011). Parametric amplification and self-oscillation in a nanotube mechanical resonator. *Nano Letters*, 11(7):2699–703.
- [Fang et al., 2008] Fang, T.-F., Zuo, W., and Luo, H.-G. (2008). Kondo Effect in Carbon Nanotube Quantum Dots with Spin-Orbit Coupling. *Physical Review Letters*, 101(24):246805.
- [Frey et al., 2012] Frey, T., Leek, P. J., Beck, M., Blais, A., Ihn, T., Ensslin, K., and Wallraff, A. (2012). Dipole Coupling of a Double Quantum Dot to a Microwave Resonator. *Physical Review Letters*, 108(4):046807.
- [Friedel, 1956] Friedel, J. (1956). On some electrical and magnetic properties of metallic solid solutions. *Canadian Journal of Physics*, 34(12A):1190–1211.
- [Galpin et al., 2010] Galpin, M. R., Jayatilaka, F. W., Logan, D. E., and Anders, F. B. (2010). Interplay between Kondo physics and spin-orbit coupling in carbon nanotube quantum dots. *Physical Review B*, 81(7):075437.
- [Gerland et al., 2000] Gerland, U., von Delft, J., Costi, T., and Oreg, Y. (2000). Transmission Phase Shift of a Quantum Dot with Kondo Correlations. *Physical Review Letters*, 84(16):3710–3713.
- [Glazman and Raikh, 1988] Glazman, L. I. and Raikh, M. E. (1988). Resonant Kondo transparency of a barrier with quasilocal impurity states. *JETP Letters*, 47(452):105.
- [Glazman and Shekhter, 1989] Glazman, L. I. and Shekhter, R. I. (1989). Coulomb oscillations of the conductance in a laterally confined heterostructure. *Journal of Physics: Condensed Matter*, 1(33):5811.
- [Goldhaber-Gordon et al., 1998] Goldhaber-Gordon, D., Shtrikman, H., Mahalu, D., David, A.-M., Meirav, U., and Kastner, M. A. (1998). Kondo effect in a single-electron transistor. *Nature*, 391(6663):156–159.
- [Göppl et al., 2008] Göppl, M., Fragner, A., Baur, M., Bianchetti, R., Filipp, S., Fink, J. M., Leek, P. J., Puebla, G., Steffen, L., and Wallraff, A. (2008). Coplanar waveguide resonators for circuit quantum electrodynamics. *Journal of Applied Physics*, 104(11):113904.
- [Grabert et al., 1993] Grabert, H., Devoret, M. H., and Kastner, M. (1993). Single Charge Tunneling: Coulomb Blockade Phenomena in Nanostructures. *Physics Today*, 46(4):62.

- [Grove-Rasmussen et al., 2012] Grove-Rasmussen, K., Grap, S., Paaske, J., Flensberg, K., Andergassen, S., Meden, V., Jørgensen, H. I., Muraki, K., and Fujisawa, T. (2012). Magnetic-Field Dependence of Tunnel Couplings in Carbon Nanotube Quantum Dots. *Physical Review Letters*, 108(17):176802.
- [Grove-Rasmussen et al., 2007] Grove-Rasmussen, K., Jørgensen, H. I., and Lindelof, P. E. (2007). Kondo resonance enhanced supercurrent in single wall carbon nanotube Josephson junctions. *New Journal of Physics*, 9(5):124–124.
- [Hartmann, 2014] Hartmann, B. (2014). Cryogenic high-frequency signal detection. Master’s thesis, Universität Regensburg.
- [Huertas-Hernando et al., 2006] Huertas-Hernando, D., Guinea, F., and Brataas, A. (2006). Spin-orbit coupling in curved graphene, fullerenes, nanotubes, and nanotube caps. *Physical Review B*, 74(15):155426.
- [Hulm and Blaugher, 1961] Hulm, J. and Blaugher, R. (1961). Superconducting Solid Solution Alloys of the Transition Elements. *Physical Review*, 123(5):1569–1580.
- [Hüttel et al., 2009a] Hüttel, A., Witkamp, B., Leijnse, M., Wegewijs, M., and van der Zant, H. (2009). Pumping of Vibrational Excitations in the Coulomb-Blockade Regime in a Suspended Carbon Nanotube. *Physical Review Letters*, 102(22):225501.
- [Hüttel et al., 2009b] Hüttel, A. K., Steele, G. A., Witkamp, B., Poot, M., Kouwenhoven, L. P., and van der Zant, H. S. J. (2009). Carbon nanotubes as ultrahigh quality factor mechanical resonators. *Nano Letters*, 9(7):2547–52.
- [Hüttel et al., 2008] Hüttel, A. K., Poot, M., Witkamp, B., and van der Zant, H. S. J. (2008). Nanoelectromechanics of suspended carbon nanotubes. *New Journal of Physics*, 10(9):095003.
- [Iijima, 1991] Iijima, S. (1991). Helical microtubules of graphitic carbon. *Nature*, 354(6348):56–58.
- [Izumida et al., 2009] Izumida, W., Sato, K., and Saito, R. (2009). Spin-Orbit Interaction in Single Wall Carbon Nanotubes: Symmetry Adapted Tight-Binding Calculation and Effective Model Analysis. *Journal of the Physical Society of Japan*, 78(7):074707.

- [Jarillo-Herrero et al., 2005a] Jarillo-Herrero, P., Kong, J., van der Zant, H., Dekker, C., Kouwenhoven, L., and De Franceschi, S. (2005). Electronic Transport Spectroscopy of Carbon Nanotubes in a Magnetic Field. *Physical Review Letters*, 94(15):156802.
- [Jarillo-Herrero et al., 2005b] Jarillo-Herrero, P., Kong, J., van der Zant, H. S. J., Dekker, C., Kouwenhoven, L. P., and De Franceschi, S. (2005). Orbital Kondo effect in carbon nanotubes. *Nature*, 434(7032):484–8.
- [Jaynes and Cummings, 1963] Jaynes, E. and Cummings, F. (1963). Comparison of quantum and semiclassical radiation theories with application to the beam maser. *Proceedings of the IEEE*, 51(1):89–109.
- [Jespersen et al., 2011] Jespersen, T. S., Grove-Rasmussen, K., Paaske, J., Muraki, K., Fujisawa, T., Nygård, J., and Flensberg, K. (2011). Gate-dependent spin-orbit coupling in multielectron carbon nanotubes. *Nature Physics*, 7(4):348–353.
- [Jin et al., 2007] Jin, Z., Chu, H., Wang, J., Hong, J., Tan, W., and Li, Y. (2007). Ultralow Feeding Gas Flow Guiding Growth of Large-Scale Horizontally Aligned Single-Walled Carbon Nanotube Arrays. *Nano Letters*, 7(7):2073–2079.
- [Kondo, 1964] Kondo, J. (1964). Resistance Minimum in Dilute Magnetic Alloys. *Progress of Theoretical Physics*, 32(1):37–49.
- [Kouwenhoven et al., 1997] Kouwenhoven, Leo P; Marucs, C., McEuen, P. L., Tarucha, S., Westervelt, R., and Wingreen, N. S. (1997). *Mesoscopic electron transport*. Kluwer Academic Publisher, Dordrecht, Netherlands.
- [Kraus, 2013] Kraus, H. (2013). Ansteuerung von Mikrowellenschaltkreisen in hybriden Tieftemperatursystemen. Diplomarbeit, Universität Regensburg.
- [Kretinin et al., 2012] Kretinin, A. V., Shtrikman, H., and Mahalu, D. (2012). Universal line shape of the Kondo zero-bias anomaly in a quantum dot. *Physical Review B*, 85(20):201301.
- [Kumar et al., 2014] Kumar, A., Gaim, M., Steininger, D., Yeyati, A. L., Martín-Rodero, A., Hüttel, A. K., and Strunk, C. (2014). Temperature dependence of Andreev spectra in a superconducting carbon nanotube quantum dot. *Physical Review B*, 89:075428.
- [LaHaye et al., 2004] LaHaye, M. D., Buu, O., Camarota, B., and Schwab, K. C. (2004). Approaching the quantum limit of a nanomechanical resonator. *Science (New York, N.Y.)*, 304(5667):74–7.

- [Laird et al., 2012] Laird, E. A., Pei, F., Tang, W., Steele, G. A., and Kouwenhoven, L. P. (2012). A high quality factor carbon nanotube mechanical resonator at 39 GHz. *Nano Letters*, 12(1):193–7.
- [Langreth, 1966] Langreth, D. (1966). Friedel Sum Rule for Anderson’s Model of Localized Impurity States. *Physical Review*, 150(2):516–518.
- [Lassagne et al., 2009] Lassagne, B., Tarakanov, Y., Kinaret, J., Garcia-Sanchez, D., Garcia-Sanchez, D., and Bachtold, A. (2009). Coupling mechanics to charge transport in carbon nanotube mechanical resonators. *Science (New York, N.Y.)*, 325(5944):1107–10.
- [Li and Evoy, 2005] Li, J. and Evoy, S. (2005). Study of laser-induced self-oscillations in silicon nanomechanical resonators. *Journal of Applied Physics*, 98(8):084316.
- [Liang et al., 2001] Liang, W., Bockrath, M., Bozovic, D., Hafner, J. H., Tinkham, M., and Park, H. (2001). Fabry - Perot interference in a nanotube electron waveguide. *Nature*, 411(6838):665–9.
- [Liang et al., 2002] Liang, W., Bockrath, M., and Park, H. (2002). Shell Filling and Exchange Coupling in Metallic Single-Walled Carbon Nanotubes. *Physical Review Letters*, 88(12):126801.
- [Lifshitz and Cross, 2008] Lifshitz, R. and Cross, M. (2008). *Annual Reviews of Nonlinear Dynamics and Complexity*, volume 1. Wiley-VCH, Weinheim.
- [Marquardt et al., 2007] Marquardt, F., Chen, J., Clerk, A., and Girvin, S. (2007). Quantum Theory of Cavity-Assisted Sideband Cooling of Mechanical Motion. *Physical Review Letters*, 99(9):093902.
- [McEuen et al., 1991] McEuen, P., Foxman, E., Meirav, U., Kastner, M., Meir, Y., Wingreen, N., and Wind, S. (1991). Transport spectroscopy of a Coulomb island in the quantum Hall regime. *Physical Review Letters*, 66(14):1926–1929.
- [Meerwaldt et al., 2012] Meerwaldt, H., Labadze, G., Schneider, B., Taspinar, A., Blanter, Y., van der Zant, H., and Steele, G. A. (2012). Probing the charge of a quantum dot with a nanomechanical resonator. *Physical Review B*, 86(11):115454.
- [Meir et al., 1993] Meir, Y., Wingreen, N., and Lee, P. (1993). Low-temperature transport through a quantum dot: The Anderson model out of equilibrium. *Physical Review Letters*, 70(17):2601–2604.

- [Ng and Lee, 1988] Ng, T. K. and Lee, P. A. (1988). On-Site Coulomb Repulsion and Resonant Tunneling. *Physical Review Letters*, 61(15):1768–1771.
- [Niemczyk et al., 2010] Niemczyk, T., Deppe, F., Huebl, H., Menzel, E. P., Hocke, F., Schwarz, M. J., Garcia-Ripoll, J. J., Zueco, D., Hümmer, T., Solano, E., Marx, A., and Gross, R. (2010). Circuit quantum electrodynamics in the ultrastrong-coupling regime. *Nature Physics*, 6(10):772–776.
- [Nocera et al., 2013] Nocera, A., Perroni, C. A., Ramaglia, V. M., Cantele, G., and Cataudella, V. (2013). Magnetic effects on nonlinear mechanical properties of a suspended carbon nanotube. *Physical Review B*, 87(15):155435.
- [O’Connell et al., 2008] O’Connell, A. D., Ansmann, M., Bialczak, R. C., Hofheinz, M., Katz, N., Lucero, E., McKeeney, C., Neeley, M., Wang, H., Weig, E. M., Cleland, A. N., and Martinis, J. M. (2008). Microwave dielectric loss at single photon energies and millikelvin temperatures. *Applied Physics Letters*, 92(11):112903.
- [O’Connell et al., 2010] O’Connell, A. D., Hofheinz, M., Ansmann, M., Bialczak, R. C., Lenander, M., Lucero, E., Neeley, M., Sank, D., Wang, H., Weides, M., Wenner, J., Martinis, J. M., and Cleland, A. N. (2010). Quantum ground state and single-phonon control of a mechanical resonator. *Nature*, 464(7289):697–703.
- [Pillet et al., 2010] Pillet, J.-D., Quay, C. H. L., Morfin, P., Bena, C., Yeyati, A. L., and Joyez, P. (2010). Andreev bound states in supercurrent-carrying carbon nanotubes revealed. *Nature Physics*, 6(12):965–969.
- [Pletyukhov and Schoeller, 2012] Pletyukhov, M. and Schoeller, H. (2012). Nonequilibrium Kondo model: Crossover from weak to strong coupling. *Physical Review Letters*, 108(26):260601.
- [Poot, 2009] Poot, M. (2009). *Mechanical Systems at the Nanoscale*. PhD thesis, TU Delft.
- [Poot and van der Zant, 2012] Poot, M. and van der Zant, H. S. (2012). Mechanical systems in the quantum regime. *Physics Reports*, 511(5):273–335.
- [Radushkevich and Lukyanovich, 1952] Radushkevich, L. V. and Lukyanovich, V. M. (1952). The structure of carbon formed by thermal decomposition of carbon monoxide on iron contacts. *Russian Journal of Physical Chemistry*, 26:88.
- [Ralph et al., 1995] Ralph, D. C., Black, C. T., and Tinkham, M. (1995). Spectroscopic Measurements of Discrete Electronic States in Single Metal Particles. *Physical Review Letters*, 74(16):3241–3244.

- [Regal et al., 2008] Regal, C. A., Teufel, J. D., and Lehnert, K. W. (2008). Measuring nanomechanical motion with a microwave cavity interferometer. *Nature Physics*, 4(7):555–560.
- [Sage et al., 2011] Sage, J. M., Bolkhovskiy, V., Oliver, W. D., Turek, B., and Welanders, P. B. (2011). Study of loss in superconducting coplanar waveguide resonators. *Journal of Applied Physics*, 109(6):063915.
- [Sahoo et al., 2005] Sahoo, S., Kontos, T., Furer, J., Hoffmann, C., Gräber, M., Cottet, A., and Schönenberger, C. (2005). Electric field control of spin transport. *Nature Physics*, 1(2):99–102.
- [Saito R.; Dresselhaus G, 1998] Saito R.; Dresselhaus G (1998). *Physical properties of carbon nanotubes*. Imperial College, London.
- [Sapmaz et al., 2003] Sapmaz, S., Blanter, Y. M., Gurevich, L., and van der Zant, H. (2003). Carbon nanotubes as nanoelectromechanical systems. *Physical Review B*, 67(23):235414.
- [Sapmaz et al., 2006] Sapmaz, S., Jarillo-Herrero, P., Blanter, Y., Dekker, C., and van der Zant, H. (2006). Tunneling in Suspended Carbon Nanotubes Assisted by Longitudinal Phonons. *Physical Review Letters*, 96(2):026801.
- [Sapmaz et al., 2005] Sapmaz, S., Jarillo-Herrero, P., Blanter, Y. M., and van der Zant, H. S. J. (2005). Coupling between electronic transport and longitudinal phonons in suspended nanotubes. *New Journal of Physics*, 7:243–243.
- [Sazonova et al., 2004] Sazonova, V., Yaish, Y., Ustünel, H., Roundy, D., Arias, T. A., and McEuen, P. L. (2004). A tunable carbon nanotube electromechanical oscillator. *Nature*, 431(7006):284–7.
- [Schmid et al., 2014] Schmid, D. R., Smirnov, S., Marganska, M., Dirnaichner, A., Stiller, P. L., Grifoni, M., Hüttel, A. K., and Strunk, C. (2014). Impact of discrete symmetries on the Kondo effect in carbon nanotubes. *arXiv:1312.6586; submitted for publication to Nature Communications*.
- [Schmid et al., 2012] Schmid, D. R., Stiller, P. L., Strunk, C., and Hüttel, A. K. (2012). Magnetic damping of a carbon nanotube nano-electromechanical resonator. *New Journal of Physics*, 14(8):083024.
- [Schneider et al., 2012] Schneider, B. H., Etaki, S., van der Zant, H. S. J., and Steele, G. A. (2012). Coupling carbon nanotube mechanics to a superconducting circuit. *Scientific Reports*, 2:599.

- [Smirnov and Grifoni, 2013a] Smirnov, S. and Grifoni, M. (2013). Keldysh effective action theory for universal physics in spin-1/2 Kondo dots. *Physical Review B*, 87(12):121302.
- [Smirnov and Grifoni, 2013b] Smirnov, S. and Grifoni, M. (2013). Nonequilibrium Kondo transport through a quantum dot in a magnetic field. *New Journal of Physics*, 15(7):073047.
- [Sprinzak et al., 2002] Sprinzak, D., Ji, Y., Heiblum, M., Mahalu, D., and Shtrikman, H. (2002). Charge distribution in a Kondo-correlated quantum dot. *Physical Review Letters*, 88(17):176805.
- [Steele et al., 2009] Steele, G. A., Hüttel, A. K., Witkamp, B., Poot, M., Meerwaldt, H. B., Kouwenhoven, L. P., and van der Zant, H. S. J. (2009). Strong coupling between single-electron tunneling and nanomechanical motion. *Science (New York, N. Y.)*, 325(5944):1103–7.
- [Tans et al., 1997] Tans, S. J., Devoret, M. H., Dai, H., Thess, A., Smalley, R. E., Geerligs, L. J., and Dekker, C. (1997). Individual single-wall carbon nanotubes as quantum wires. *Nature*, 386(6624):474–477.
- [Teufel et al., 2008] Teufel, J. D., Regal, C. A., and Lehnert, K. W. (2008). Prospects for cooling nanomechanical motion by coupling to a superconducting microwave resonator. *New Journal of Physics*, 10(9):095002.
- [Usmani et al., 2007] Usmani, O., Blanter, Y. M., and Nazarov, Y. (2007). Strong feedback and current noise in nanoelectromechanical systems. *Physical Review B*, 75(19):195312.
- [van der Wiel et al., 2000] van der Wiel, W. G., Franceschi, S. De, Fujisawa, T., Elzerman, J. M., Tarucha, S., Kouwenhoven, L. P. (2000). The Kondo Effect in the Unitary Limit. *Science*, 289(5487):2105–2108.
- [Wallraff et al., 2004] Wallraff, A., Schuster, D. I., Blais, A., Frunzio, L., Huang, R.-S., Majer, J., Kumar, S., Girvin, S. M., and Schoelkopf, R. J. (2004). Strong coupling of a single photon to a superconducting qubit using circuit quantum electrodynamics. *Nature*, 431(7005):162–7.
- [Wang and Okoro, 1990] Wang, Y.-C. and Okoro, J. A. (1990). Impedance calculations for modified coplanar waveguides. *International Journal of Electronics*, 68(5):861–875.

- [Watanabe et al., 1994] Watanabe, K., Yoshida, K., Aoki, T., and Kohjiro, S. (1994). Kinetic Inductance of Superconducting Coplanar Waveguides. *Japanese Journal of Applied Physics*, 33(Part 1, No. 10):5708–5712.
- [Wilson, 1975] Wilson, K. (1975). The renormalization group: Critical phenomena and the Kondo problem. *Reviews of Modern Physics*, 47(4):773–840.
- [Wingreen and Meir, 1994] Wingreen, N. and Meir, Y. (1994). Anderson model out of equilibrium: Noncrossing-approximation approach to transport through a quantum dot. *Physical Review B*, 49(16):11040–11052.
- [Witkamp et al., 2006] Witkamp, B., Poot, M., and van der Zant, H. S. J. (2006). Bending-mode vibration of a suspended nanotube resonator. *Nano Letters*, 6(12):2904–8.
- [Wolff, 2006] Wolff, I. (2006). *Coplanar Microwave Integrated Circuits*. John Wiley & Sons, Inc., 1st edition.
- [Yamada et al., 1984] Yamada, K., Yosida, K., and Hanzawa, K. (1984). Comments on the Dense Kondo State. *Prog. Theo. Phys.*, 71(3):450–457.

Curriculum Vitae

Daniel Richard Schmid, geboren am 3. Dezember 1985 in Nürnberg, ledig

1992–1996 Grundschule Möning

1996–2005 Willibald-Gluck-Gymnasium Neumarkt i.d.Opf.

2005 Abitur

2005–2010 Studium der Physik an der Universität Regensburg

2007 Vordiplom

2009–2010 Diplomarbeit am Lehrstuhl "Physik der Mikro- und Nanostrukturen",
Prof. Dr. Christoph Strunk, Universität Regensburg
"Growth of ultra-clean carbon nanotubes for low temperature
transport measurements"

2010 Diplom mit Auszeichnung

seit 2010 Wissenschaftlicher Mitarbeiter in der Emmy-Noether
Nachwuchsgruppe Dr. A. K. Hüttel, Universität Regensburg
Promotionsstipendium der Studienstiftung des deutschen Volkes

Acknowledgments

Zuerst geht mein Dank an Marina Horvath, der tollen Frau an meiner Seite – für die wundervolle Zeit mit dir, und die wichtige Unterstützung, die ich von dir während meines Studiums und meiner Promotion bekommen habe!

Ich danke meiner Familie für die Unterstützung während meiner ganzen Ausbildungszeit – für den Rückhalt und die guten Ratschläge, die ihr mir gegeben habt.

Ich möchte mich bei meinen langjährigen Kommilitonen und Kollegen Christoph Drexler und Thomas Stangl bedanken – für die gemütlichen Stunden neben dem Promotionsstudium.

Besten Dank auch an meine Kollegen in der AG Hüttel für das gute Arbeitsumfeld und die gute Zusammenarbeit.

Besonders danke ich meinem langjährigen Büro-Kollegen Peter Stiller für die Unterstützung bei der Probenfabrikation und bei den Messungen. Dazu gehörte gelegentlich auch das Helium-Füllen am Sonntag. Ganz wichtig waren dabei auch die Auszeiten u.a. im Innenhof. Dabei schließe ich natürlich auch Thomas Hupfauer und Thomas Kuczmik mit ein.

Vielen Dank an Alois Dirnaichner – v.a. für die produktive gemeinsame Messzeit. Neben vielen schönen Messdaten habe ich in dieser Zeit auch vieles von deiner theoretischen Expertise mitbekommen können. In diesem Rahmen möchte ich gleich noch den Kollegen vom Lst. Prof. Weiss für die Messzeit an ihrem Mischkryostaten danken.

Ich danke Herrmann Kraus für die Unterstützung bei Elektronik- und Programmierfragen, beim Messaufbau, und bei den Hochfrequenzmessungen. Außerdem noch vielen Dank für die Unterstützung an Dr. Andreas Pfeffer, Stefan Blien, Karl Götz, Benedikt Hartmann und Felix Schupp.

Auch möchte ich den Kollegen der AG Strunk und vom Lehrstuhl Weiss generell für die gute Zusammenarbeit danken.

Besten Dank an die Techniker Thomas Haller, Uli Gürster und Michael Weigl für sämtliche Unterstützung bei Planung und technischer Umsetzung.

Für eine stets gute Zusammenarbeit möchte ich mich auch bei dem Team um Dieter Riedl von der Elektronik-Werkstatt und bei dem Team um Norbert Sommer / Johann Deinhart von der Mechanik-Werkstatt bedanken.

Außerdem danke ich Thomas Solleder und Christian Heimerl für die zuverlässige Versorgung mit flüssigem Helium – dem Lebenselixier eines Tieftemperatur-Physikers.

Dabei geht mein Dank auch an Herrn Prof. Dr. Dieter Weiss für die gut ausgebaute Infrastruktur am Lehrstuhl, welche unverzichtbar bei der experimentellen Physik ist.

Für die finanzielle Unterstützung, und die damit verbundene teilweise Entlastung des Emmy-Noether Projektes von Dr. Andreas K. Hüttel, bedanke ich mich bei der Studienstiftung des Deutschen Volkes e.V. für die mehrjährige Förderung.

I want to thank the theory group of Prof. Dr. Milena Grifoni for the collaboration; thanks to Dr. Sergey Smirnov for the many-particle calculations employing the Keldysh formalism, and to Dr. Magdalena Marganska who performed the single-particle calculations of the quantum dot states.

Vielen Dank auch an Sebastian Pfaller für die interessanten Diskussionen und Unterhaltungen auf den vielen Zugfahrten während meiner Pendler-Zeit.

Besonderen Dank möchte ich Herrn Prof. Dr. Christoph Strunk aussprechen, welcher mich für das interessante Gebiet der mesoskopischen Physik motiviert hat, und mich, neben vielen aufschlussreichen Unterhaltungen, auch durch das Mentoring im Rahmen der Graduiertenschule unterstützt hat.

Zu guter Letzt gilt mein Dank meinem Betreuer Dr. Andreas K. Hüttel. Ich danke für das interessante Thema, für die vielen Stunden der rat- und tatkräftigen Unterstützung bei der Fabrikation, bei den Messungen, dem Auswerten und dem Präsentieren der Ergebnisse. Diese gute und enge Zusammenarbeit hat maßgeblich zum Gelingen der Arbeit beigetragen und die hohe Ergiebigkeit der Messungen bewirkt. Vielen Dank außerdem bei der Unterstützung im Rahmen der Studienstiftung. Danke für die stets offene Türe.